Università degli Studi Roma Tre

DIPARTIMENTO DI MATEMATICA E FISICA

Corso di Laurea Magistrale in Fisica

The laser calibration system of the muon *g-2* experiment at Fermilab

Candidato:
Eleonora Rossi
Matricola 438432

Relatore interno:
Prof.ssa Domizia Orestano

Relatore esterno:
Dott. Graziano Venanzoni

Anno Accademico 2015-2016

Contents

Introduction

Precise measurements of fundamental quantities have played a key role in the development of Theoretical Physics models such as Standard Model. Even though this model describes so many physical phenomena and has demonstrated huge successes in providing experimental predictions, it is necessarily incomplete because it does leave a number of things unexplained.
The reason why the muon anomalous magnetic moment is so interesting and plays a key role in Elementary Particle Physics at its fundamental level is the fact that it can be predicted by theory with very high accuracy and at the same time can be measured with the same precision in an unambiguous experimental setup; the fact that the experimental conditions can be controlled very precisely, with small systematic uncertainties, has to do with the very interesting intrinsic properties of muons.
The anomalous magnetic moment of the muon, a_{μ}, represents an important test of the Standard Model because of a long standing discrepancy, of more than three standard deviations, between Standard Model predictions and experimental values resulting from the last g-2 experiment at Brookhaven (2001).
A new muon g-2 experiment at Fermilab is going to start data taking within a year; the goal of the experiment is a four-fold improvement in the experimental precision thereby reducing the error on a_{μ} up to 0.14 ppm which is comparable to the 0.4 ppm uncertainty on the most accurate Standard Model prediction.
Many improvements are needed with respect to previous experiments to reach the requested statistical uncertainty of 0.1 ppm. Among these improvements, the attention will be focused on improved detectors against signal pileup and on a continuous monitoring and re-calibration of the detectors: a high-precision laser calibration system that will monitor the gain fluctuations of the calorimeter photodetectors at 0.04 % accuracy will be used. The level of accuracy required is a challenge for the design of the calibration system because it is at least one order of magnitude higher than that of all other existing, or adopted in the past, calibration systems for calorimetry in Particle Physics.
The Italian g-2 Collaboration is developing and testing such a system.
Tests related to the whole calibration system and to the calorimeter will be reported and explained: a test of a calorimeter prototype was performed in Frascati at the beginning of March 2016; I took part actively in this test taking care in particular of the Local Monitor system and analysis.
Additional tests, due to the high level of accuracy required for the experiment, were necessary: the response of every detector has to be really well known; the distribution chain, including fibers and fiber connections, has to be fully tested in order to check its stability in time; the bias voltage, necessary to supply Silicon photomultipliers, has to be constant over time, in order not to induce detector gain fluctuation.

Chapter 1

The Anomalous Magnetic Moment of the muon

1.1 Magnetic moments: historical perspective

The magnetic dipole moment $\vec{\mu}$ of an object is a measure of how much torque it experiences when placed in a magnetic field:

$$\vec{\tau} = \vec{\mu} \times \vec{B} \qquad\qquad U = -\vec{\mu} \cdot \vec{B} \tag{1.1}$$

where U is the potential energy associated with the magnetic dipole moment.
Subatomic particles of mass m and charge e, have a magnetic moment that is generated by their intrinsic angular momentum, $\vec{S}$; these two quantities are related by the gyromagnetic ratio g[1][1]:

$$\vec{\mu} = g\left(\frac{e}{2m}\right)\vec{S} \tag{1.2}$$

The dimensionless number g is a fundamental property of the particle and its interactions. For the case of a simply rotating structure [2], e.g. a particle which moves with speed v along a circular path of radius r, if the limit $r \to 0$ is taken, the particle effectively constitutes a loop that encloses an area $A = \pi r^2$ and carries a current $I = ev/2\pi r$.
The magnitude of the magnetic moment is

$$\mu = IA = \frac{evr}{2} \tag{1.3}$$

The magnitude of the angular momentum associated with the particle's motion is $L = mvr$, so

$$\vec{\mu} = \left(\frac{e}{2m}\right)\vec{L} \tag{1.4}$$

Comparison shows that $g = 1$ using a purely classical treatment [1].
The breakthrough in the mathematical description of spin came in 1928 from Dirac's attempts to create a relativistic extension of *Schrödinger*'s equation that, unlike the Klein-Gordon equation, preserved linearity with respect to time [3]:

$$i\hbar\frac{\partial\psi}{\partial t} = \mathcal{H}\psi \qquad with \quad \mathcal{H} = c\,(\beta mc + \vec{\alpha}\cdot\vec{p}) \;\rightarrow\; i(\partial_\mu - ieA_\mu(x))\gamma^\mu\psi(x) = m\psi(x) \tag{1.5}$$

[1]Known also as g-factor or Landé factor.

where $\vec{\alpha}$ and β are the 4×4 Dirac matrix operators, $\vec{p}$ is the operator $-i\hbar\nabla$ and γ^{μ} are a set of conventional matrices with specific anticommutation relations defined as $\gamma^0 \equiv \beta, \gamma^i \equiv \beta\alpha^i$.
ψ is a four-component column matrix and when solved for zero velocity Equation 1.5 yields both particle and antiparticle states.
In the presence of an electromagnetic field defined by the usual scalar and vector potentials, the Hamiltonian becomes

$$\mathcal{H} = c\,(\beta mc + \vec{\alpha}\ \cdot \vec{p}) + eV$$

where the kinetic momentum operator $\vec{p}$ has the minimal coupling form

$$\vec{p} = -i\hbar\nabla - \frac{e}{c}\vec{A}$$

In the non-relativistic limit the matrix ψ can be divided into two major and two minor components (the latter can be neglected in the low-energy limit). Thus by exploiting the algebraic properties of $\vec{\alpha}$ and β and in particular the relation between $\vec{\alpha}$ and the Pauli spin operators $\vec{\sigma}$, the Dirac equation reduces to a two-component spinor equation with the non-relativistic Hamiltonian[2] $\mathcal{H}_0$ given by

$$\mathcal{H}_0 = \frac{p^2}{2m} + eV - \frac{e\hbar}{2mc}\vec{\sigma}\ \cdot\ \vec{B} \tag{1.6}$$

The additional term clearly represents the energy of a magnetic dipole in the external field an points to an outstanding achievement of the Dirac theory that is the integration of the intrinsic spin of the electron and its related magnetic moment in a straightforward way. The magnetic moment is obtained by replacing the angular momentum operator $\vec{L}$ by the intrinsic spin angular momentum operator $\vec{S} = \hbar\vec{\sigma}/2$

$$\vec{\mu} = \frac{e\hbar}{2mc}\vec{\sigma} \tag{1.7}$$

A comparison with Equation 1.2 shows that the Dirac electron has a g value equal to 2 [2].
Given the success in Quantum Mechanics in predicting g to be 2 for the half-integer spin electron, it was natural to assume that the half-integer spin proton would also be a Dirac particle with $g \equiv 2$. Nevertheless, in 1933 Estermann and Stern [4] experimentally found a value of 5.6 for the g-factor of the proton. Shortly thereafter, Rabi measured the magnetic moment of the deuteron and from that a g-factor of -3.8 could be inferred for the neutron. Of course, it is now known that the neutron and proton are composite particles containing moving, fractionally-charged quarks: with the current loops induced by the quarks it is no wonder that the magnetic moment for nucleons deviates strongly from the prediction for a point-like particle.
Table 1.1 shows the measured values of the gyromagnetic ratio for different particles: composite particles such as the proton and neutron show large differences from 2, which are indications of their rich internal structure.
Kush and Foley presented the first precise determination of the magnetic moment of the

[2] The expression of the Hamiltonian is just the expected expression for the case of a spin-less charged particle in an electromagnetic field except for the third term.

Particle	Experimental value	Relative precision	Ref.	Theoretical prediction	Ref.
Electron	2.0023193043738(82)	4×10^{-12}	[5]	2.00231930492(29)	[6]
Muon	2.0023318406(16)	8×10^{-10}	[7]	2.0023318338(14)	[8]
Tau	2.008(71)	4×10^{-2}	[9]	2.0023546(6)	[10]
Proton	5.585694674(58)	1×10^{-8}	[5]	5.58	[11]
Neutron	-3.8260854(10)	3×10^{-7}	[5]	-3.72	[11]

Table 1.1: Gyromagnetic ratios g for various subatomic particles

electron in 1948, just before the theoretical result had been settled.
They deduced the value of the electron g-factor from atomic-beam magnetic resonance experiments carried out on several different alkali atoms. These were chosen because of the ease with which they could be detected against the large background due to residual gas molecules in the vacuum system, but their use brought complications due to effect of nuclear magnetic dipole and electric quadrupole moments.
They found an average value for the electron anomalous magnetic moment of [2]:

$$g = 2(1 + a) \quad where \quad a = (0.00119 \pm 0.00005)$$

Although the treatment of the hydrogen atom given by the Dirac theory was beautiful and satisfying, the theory carried with it some strange consequences arising from the existence of the negative energy states. It was therefore considered highly desirable to subject the fine structure predictions to careful experimental tests [12].
A famous experiment by Lamb and Retherford in 1947 showed that the states of the hydrogen atom were not degenerate: the $2S_{1/2}$ level is higher than the $2P_{1/2}$ by about 1000 MHz (0.033 cm^{-1}) or about 9% of the spin relativity doublet separation.
The energy levels of a hydrogen-like atom are given by

$$W = mc^2 \left\{ [1 + (\alpha Z)^2 (n - |K| + (K^2 - \alpha^2 Z^2)^{1/2})^{-2}]^{-1/2} - 1 \right\}$$

where $|K| = j + \frac{1}{2}$.
Therefore levels having the same principal quantum number n and inner quantum number j should be degenerate.
These events had a dramatic impact in establishing Quantum Field Theory as a general framework for the theory of elementary particles and for our understanding of the fundamental interactions. It stimulated the development of the Quantum Electrodynamics (QED) in particular and the concepts of Quantum Field Theory in general [13].
The increase in the hydrogen hyperfine levels could be interpreted as coming from an additional magnetic moment. Motivated by this dilemma, Schwinger carried out the first "loop" calculation and predicted that the electron had an anomalous magnetic moment whose value should be given in terms of the fine structure constant α [3]:

$$a_e = \frac{\alpha}{2\pi} \qquad where\ a_e = \frac{(g_e - 2)}{2}$$

According to Schwinger [14],

"The simplest example of a radiative correction is that for the energy of an electron in an external magnetic field. The detailed application of the theory shows that the radiative correction to the magnetic interaction energy corresponds to an additional magnetic moment associated with the electron spin, of magnitude $\delta\mu/\mu = (1/2\pi)e^2/\hbar c = 0.001162$. The radiative correction to the energy of an electron in a Coulomb field will produce a shift in the energy levels of hydrogen-like atoms, and modify the scattering of electrons in a Coulomb field. Such energy level displacements have recently been observed in the fine structure of hydrogen, deuterium and ionized helium."

The calculation of the leading (one-loop diagram) contribution to the anomalous magnetic moment by Schwinger was one of the very first higher order QED predictions establishing in theory the effect from quantum fluctuations via virtual electron-photon interactions: the small discrepancy is caused by corrections from higher-order interactions described by Quantum Field Theories. In QED this value is universal for all leptons.
Looking at Table 1.1 it has to be noted that the gyromagnetic ratios of stable and nearby-stable particles can be measured experimentally to extremely high precision.
Indeed, the electron g-factor, known to a precision of 4×10^{-12}, is the physical quantity with the smallest quoted uncertainty in the current CODATA[3] table [15] [1].

Virtual particles

The Heisenberg Uncertainty principle , $\Delta E \cdot \Delta t \geq \frac{\hbar}{2}$, suggests that space is not really empty. In fact, according to this principle, the uncertainty in energy of a system increases when the system is analyzed using shorter and shorter time scales.
In many processes, a high-energy force-carrier particle, which almost immediately decays into low-energy particles, is created. These high-energy, short-lived particles are virtual particles.
The conservation of energy seems to be violated by the apparent existence of these energetic particles for a very short time. However, according to the above principle, if the time of a process is exceedingly short, then the uncertainty in energy can be really large. Thus, due to the Heisenberg Uncertainty principle, these high-energy force-carrier particles may exist if they are short lived. In a sense, they escape reality's notice.
Quantum Field Theory predicts, as a result, that in empty space the electric charge can be shielded and considerably reduced over long distances.
The presence of a charge will cause a polarization of the virtual pairs of the empty space; over long distances these virtual particles will shield the "nude charge" so the observed charge will be less than the expected one. Going into the virtual particle cloud instead, this shielding effect will decrease and the observed charge will be greater than the expected one.
If it were not for the quantum world of virtual particles, the g-factor of the leptons would be identically 2 and any deviation would be a strong indication of an internal structure, as in the proton and neutron.
However, the magnetic moment cannot be measured without the influence from virtual exchanges made explicit in Quantum Field Theories. The screening effect of the virtual particles leads to a slight change (anomaly) in the observed magnetic moment [16].

[3] International Council for Science: Committee on Data for Science and Technology.

1.2 Muon properties: why is the muon chosen?

The key point is that a_μ can be both precisely predicted as well as experimentally measured: through experimental data it is possible to subject the theory to very stringent tests and find its possible limitations [13].
Actually, all three charged leptons, $e^\pm$, $\mu^\pm$ and $\tau^\pm$, of the Standard Model can be treated on the same footing, except for the fact that the very different values of their masses will induce different sensitivities with respect to the mass scales involved in the higher order quantum corrections [17].
While a_e is rather insensitive to strong and weak interactions, hence providing a stringent test of QED and leading to the most precise determination to date of the fine-structure constant α, a_μ allows to test the entire Standard Model, as each of its sectors contributes in a significant way to the total prediction [18].
Compared with a_e, a_μ is also much better suited to unveil or constrain "New Physics" effects. For a lepton l, their contribution to a_l is generally proportional to m_l^2/Λ^2, where m_l is the mass of the lepton and Λ is the scale of "New Physics", thus leading to an $(m_\mu/m_e)^2 \sim 4 \times 10^4$ relative enhancement of the sensitivity of the muon versus the electron: the reduced experimental precision[4] is more than compensated and a_μ^{EXP} represents a more sensitive probe of "New Physics" [19].
Looking at the relative enhancement of sensitivity, the anomalous magnetic moment of the τ would offer the best opportunity to detect "New Physics"; unfortunately, the very short lifetime of the τ lepton, which can also decay into hadronic states because of its high mass, makes such a measurement impossible at present [17].
That the experimental conditions can be controlled very precisely, with small systematic uncertainties, has to do with the very interesting intrinsic properties of the muon, which are briefly described in the following.
There are several properties of the muon which have markedly affected the way in which the muon g-2 experiments[5] have developed. One of the fundamental disadvantageous properties is the fact that the muon is an unstable particle; however not all of the properties of the muon increase the difficulty of g-2 experiments and the balance is rather restored by parity non-conservation in both the birth and the decay of these particles [2] as it is explained in the last part of this section. After the discovery of parity (P) violation in weak interactions it immediately became evident that weak decays of charged pions were producing polarized muons.
All muon g-2 experiments are based on the decay chain

$$\begin{array}{l}\pi \to \mu + \nu_\mu \\ \qquad\;\; \hookrightarrow e + \nu_e + \nu_\mu\end{array}$$

producing the polarized muons which decay into electrons.
Let's consider, as an example, the π^+ decay. Being a two-body decay, the lepton energy is fixed (monochromatic) and given by $E_\mu = \sqrt{m_\mu^2 + p_\mu^2} = \frac{m_\pi^2 + m_\mu^2}{2m_\pi^2}$, $p_\mu = \frac{m_\pi^2 - m_\mu^2}{2m_\pi^2}$.
Since the π^+ has spin 0 and the emitted neutrino is left-handed ($(1-\gamma_5)/2$ projector), by angular momentum conservation along with the left-handed helicity state of the neutrinos, the μ^+ must be left-handed as well [13].

[4] a_μ^{EXP} is currently about 1000 times less precisely measured than a_e^{EXP}.
[5] a_μ and g-2, which differ just for a 2 factor, will be used depending on the context.

Because of the spin-zero nature of the pion, the decay muons are emitted isotropically. Hence a pion source produces an unpolarized muon distribution. The helicity discussion implies that for any positive muon, the spin is anti-parallel to the momentum. Thus, to an observer with a small solid angle view of a pion source, muons are highly polarized.
This is exactly the case for muons that are guided from a pion source to an experiment using a beamline [20].
The muon is unstable and decays via the weak three body decay $\mu^+ \to e^+\bar{\nu}_\mu\nu_e$ (or $\mu^- \to e^-\bar{\nu}_e\nu_\mu$).

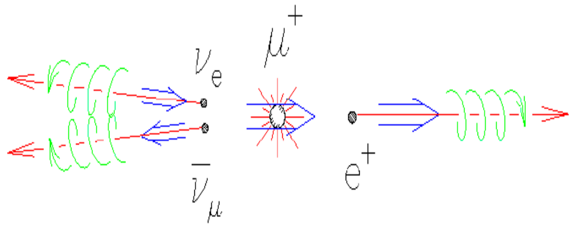

The μ^+ and the e^+ would be right-handed in the massless approximation[6]. This implies the decay scheme of Figure 1.1 for the muon.

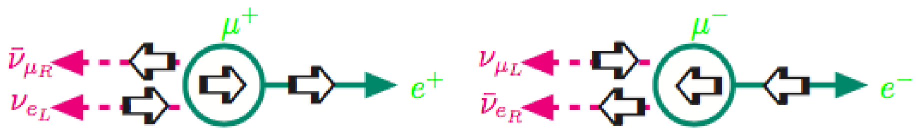

Figure 1.1: In $\mu^+[\mu^-]$ decay the produced $e^+[e^-]$ has positive [negative] helicity, respectively [13].

Again it is the P violation which prefers positrons (electrons) emitted in the direction of the muon spin (opposite to the muon spin). Therefore, the measurement of the direction of the positron (electron) momentum provides the direction of the muon spin (opposite to the muon spin).

1.3 Theoretical calculation

The most important condition for the anomalous magnetic moment to be a useful monitor for testing a theory is its unambiguous predictability within that theory.
The evaluation of the Standard Model (SM) prediction for the anomalous magnetic moment of the muon has occupied many physicists for over fifty years.
Schwinger's 1948 calculation of its leading contribution was one of the very first results of QED, and its agreement with the experimental value of the anomalous magnetic moment of the electron, a_e, provided one of the early confirmations of this theory [19].
The simplest modification, in order to correct the magnetic moment, is when the particle

[6]The corresponding anti-particles left-handed.

interacts with the external electromagnetic field while part of its original energy is carried by a previously emitted virtual photon which is subsequently reabsorbed. More complex corrections involve more than one virtual photon and also virtual lepton pairs.
The muon's magnetic moment is illustrated as a Feynman diagram in Figure 1.2 (a). This diagram shows the muon coupling directly to a photon from the external magnetic field; it corresponds to the Dirac equation's prediction that $g = 2$.
The radiative corrections are represented symbolically by the "blob" in Figure 1.2 (b); any allowed intermediate state may be inserted in its place. The dominant correction arises from a coupling to a single virtual photon, as shown in Figure 1.2 (c).

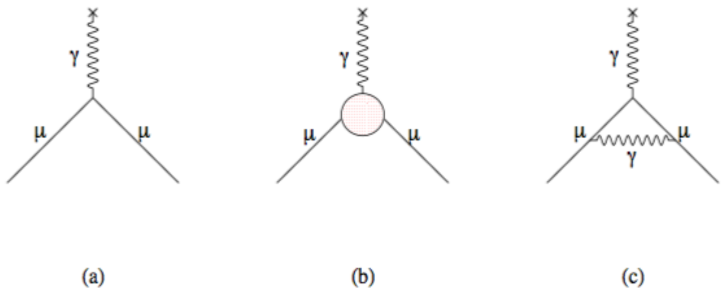

Figure 1.2: Feynman diagrams for (a) the magnetic moment, corresponding to $g = 2$, (b) the general form of diagrams that contribute to the a_μ, and (c) the Schwinger term.

Since the experimental measurements have reached a very high accuracy, it is necessary to include in the theoretical calculation of a_μ contributions from Quantum Electrodynamics (QED), Quantum Chromodynamics (QCD) and Electroweak Theory (EW):

$$a_\mu^{SM} = a_\mu^{QED} + a_\mu^{QCD} + a_\mu^{EW} \tag{1.8}$$

The first term, a_μ^{QED}, denotes all the contributions which arises from loops involving only virtual photons and leptons. Among these, it is useful to distinguish those which involve only the same lepton flavour l for which we wish to compute the anomalous magnetic moment, and those which involve loops with leptons of different flavours, denoted collectively as $l^{'}$,

$$a_\mu^{QED} = A_1\left(\frac{\alpha}{\pi}\right) + \sum_{n\geq 2} A_n(l,l^{'})\left(\frac{\alpha}{\pi}\right)^n \tag{1.9}$$

The second type of contribution, a_μ^{QCD}, involves also quark loops. Their contribution is far from being limited to the short distance scales, and a_μ^{QCD} is an intrinsically non perturbative quantity[7]. Finally, at some level of precision, the weak interactions can no longer be ignored, and contributions of virtual Higgs or massive gauge boson degrees of freedom induce the third component a_μ^{EW}. Of course, starting from the two loop level, a hadronic contribution to a_μ^{EW} will also be present [17].
Any discrepancy remaining between the experimental and theoretical values, proved not

[7]Considering a low energy scale.

to be a statistical fluctuation or an experimental bias, must then be the result of "New Physics": particles and interactions that are not included in the Standard Model. The search for such a difference, if it exists, provides the motivation for the g-2 experiment [1].

1.4 Experimental principles

The principle of a_μ measurement is rather simple; however the short lifetime of the muon, $\tau_\mu = 2.2\ \mu$s, made the measurement difficult from the practical point of view.
In this short period of time, the muons have to be produced from pion decay, stored in a magnetic field and their spin has to be analyzed.

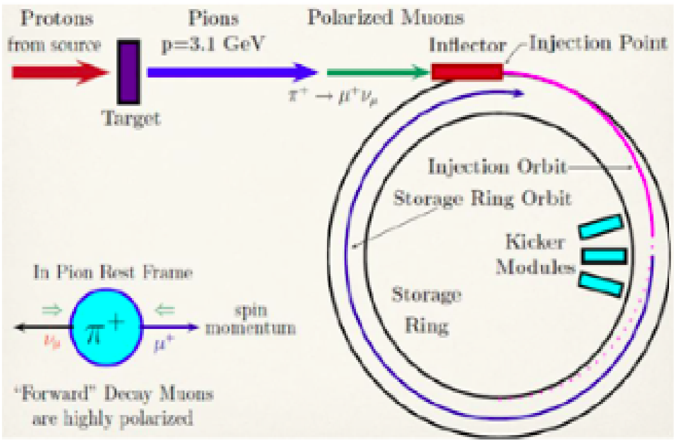

Figure 1.3: The schematics of muon injection and storage in the g-2 ring [13].

As shown in Figure 1.3, muons originate from the interaction between an energetic proton beam and a light-element target. The proton collisions produce pions, which then decay into muons. The muon beam produced can be nearly 100 % spin polarized, i.e. all the muon spins are pointing in the same direction.
Parity violation in the weak interaction allows the spin direction to be measured as a function of time. Let's consider a μ^+ decay: $\mu^+ \to e^+\nu_\mu\bar{\nu}_e$.
In the rest frame of the muon, the differential probability for the positron to emerge with a normalized energy $y = E/E_{max}$ at an angle θ_s with respect to the muon spin is:

$$\frac{dP}{dy dcos\theta_s} = n(y)[1 + A(y)cos\theta_s] \tag{1.10}$$

with:

$$n(y) = y^2(3 - 2y) \qquad and \qquad A(y) = \frac{2y - 1}{3 - 2y}$$

The quantities $n(E)$ and $A(E)$ are plotted in Figure 1.4, normalized to $E_{max} = 52.8$ MeV.

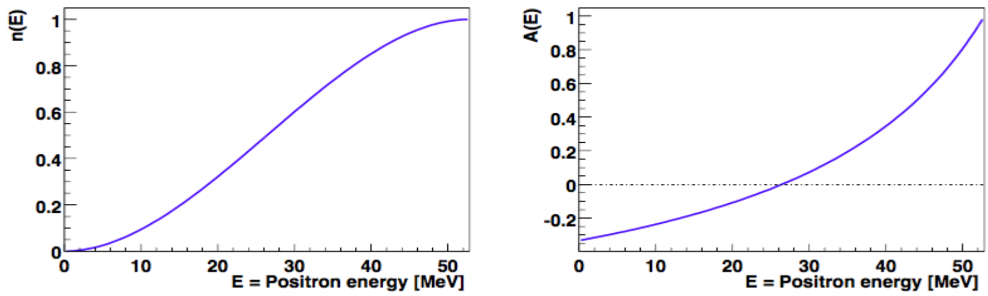

(a) $n(E)$

(b) $A(E)$

Figure 1.4: Number density and asymmetry distributions for decay positrons in the muon rest frame [1].

Positrons with $y > 0.5$ are most likely to be emitted in the direction of the muon spin, and those with lower energy are most likely to be emitted opposite it. Because more positrons are emitted with $y > 0.5$ and because their asymmetry is higher, the overall effect is that the decay positrons tend to go in the direction of the muon spin. Integrating over all energies,

$$\int_0^1 \frac{dP}{dyd\Omega} = \frac{1}{2}[1 + \frac{1}{3}cos\theta_s]$$

If a nonzero energy threshold is established, then the asymmetry is even higher than $\frac{1}{3}$ [1].
Now that positron memory of muon spin direction, after the energy cut, is evident, how to determine a_μ has to be shown.
In a magnetic-field region of high uniformity the particles are somehow trapped and consequently experience a torque [2]. Classically, one would expect the dipole to rotate into a position where the potential energy in Equation 1.1 is minimized. However, conservation of energy implies the dipole must have some means of dissipating energy. At the particle scale, the dipole does not have any means like friction to dissipate energy, so the angle between the dipole and the magnetic field must remain fixed [16]. Therefore, the torque is manifested as a rotation: the particle acts like a gyroscope and its spin axis precesses around the field direction [2]. This rotation is referred to as *Larmor precession*; in the particle rest frame the frequency is:

$$\vec{\omega_s^*} = g\frac{e}{2m}\vec{B^*} \tag{1.11}$$

The frequency is written as a 3-vector, whose each component describes the motion of the spin about one of the three spatial axes so that

$$\frac{\partial \vec{s}}{\partial t} = \vec{\omega_s} \times \vec{s} \tag{1.12}$$

The starred quantities are measured in the muon's rest frame.
The muon moves relativistically along a circular path in the lab frame, and its cyclotron

frequency[8] is given by

$$\vec{\omega_c} = \frac{e\vec{B}}{m\gamma} \tag{1.13}$$

The muon experiences a transverse centripetal acceleration, which leads to a Thomas precession [21] of all observables in the lab frame. This effect may be thought of as a Lorentz contraction of the rest frame axes [22], and it causes the spin to appear to turn at a frequency

$$\vec{\omega_T} = (\gamma - 1)\vec{\omega_c} = (\gamma - 1)\frac{e\vec{B}}{m\gamma} \tag{1.14}$$

Because of mutually canceling factors of γ, the Larmor spin precession occurs at the same rate in both frames. Time moves faster in the muon rest frame, but the magnetic field is stronger there, and the product $\vec{B} \cdot t$ is an invariant. Altogether, the spin in the lab frame rotates at a frequency

$$\vec{\omega_s} = g\frac{e}{2m}\vec{B} + (\gamma - 1)\frac{e\vec{B}}{m\gamma} \tag{1.15}$$

Jackson [23] citing Thomas [21] and Bargmann, Michel, and Telegdi [24], expands this expression to include electric as well as magnetic fields:

$$\vec{\omega_s} = \frac{e}{m}\left[\left(\frac{g}{2} - 1 + \frac{1}{\gamma}\right)\vec{B} - \left(\frac{g}{2} - 1\right)\frac{\gamma}{\gamma + 1}(\vec{\beta} \cdot \vec{B})\vec{\beta} - \left(\frac{g}{2} - \frac{\gamma}{\gamma + 1}\right)(\vec{\beta} \times \vec{E})\right] \tag{1.16}$$

In this general treatment, the cyclotron frequency is written as:

$$\vec{\omega_c} = \frac{1}{\beta^2}\frac{\partial\vec{\beta}}{\partial t} \times \vec{\beta} = \frac{e}{m}\left[\frac{1}{\gamma}\vec{B} - \frac{1}{\gamma\beta^2}(\vec{\beta} \cdot \vec{B})\vec{\beta} - \frac{\gamma}{\gamma^2 - 1}(\vec{\beta} \times \vec{E})\right] \tag{1.17}$$

The anomalous precession frequency[9] $\vec{\omega_a}$ is defined as the *difference* of the spin precession and cyclotron frequencies. It is the frequency at which the muon's spin advances relative to its momentum.

Assuming that the motion of the muons is purely longitudinal so that no component of the momentum is parallel to the magnetic field, the terms containing $\vec{\beta} \cdot \vec{B}$ drop out, leaving

$$\vec{\omega_a} = \vec{\omega_s} - \vec{\omega_c}\frac{e}{m}\left[a_\mu\vec{B} - \left(a_\mu - \frac{1}{\gamma^2 - 1}\right)(\vec{\beta} \times \vec{E})\right] \tag{1.18}$$

This expression may be simplified further by choosing $\gamma = \sqrt{\frac{1}{a_\mu} + 1} \approx 29.3$ so that the dependence on $\vec{E}$ disappears. This γ corresponds to a "magic" muon momentum of 3.09 GeV/c and leads to a relativistic muon lifetime of 64.4 μs.

The relationship between a_μ and $\vec{B}$ is then [1]

$$\vec{\omega_a} = \frac{e}{m}a_\mu\vec{B} \tag{1.19}$$

[8]The frequency at which it completes circular orbits.

[9]The "g-2 frequency".

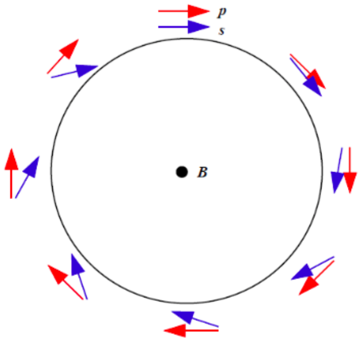

Figure 1.5: Muon's spin advances relative to its momentum.

Because the spin appears to rotate at the frequency ω_a, so does the distribution of decay positrons.
In the laboratory frame, the stored muons are highly relativistic so that the range of observed decay angles is extremely compressed; the effect of the Lorentz boost is illustrated in Figure 1.6. Compared to the angle subtended by a practical detector, all decays are forward. The energy of the positron in the laboratory frame is given by:

$$E_{lab} = \gamma(E^* + \beta p^* cos\theta^*)$$

The positron energy E^* is also high enough, in general, to justify a fully relativistic treatment, so

$$E_{lab} = \gamma E^*(1 + cos\theta^*)$$

The laboratory energy clearly depends strongly on the decay angle θ^*. To have a high energy in the laboratory frame, a positron must have a high energy in the Centre-of-Mass (CM) frame and also be emitted at a forward angle there. Setting a laboratory energy threshold therefore selects a range of angles in the muon rest frame.

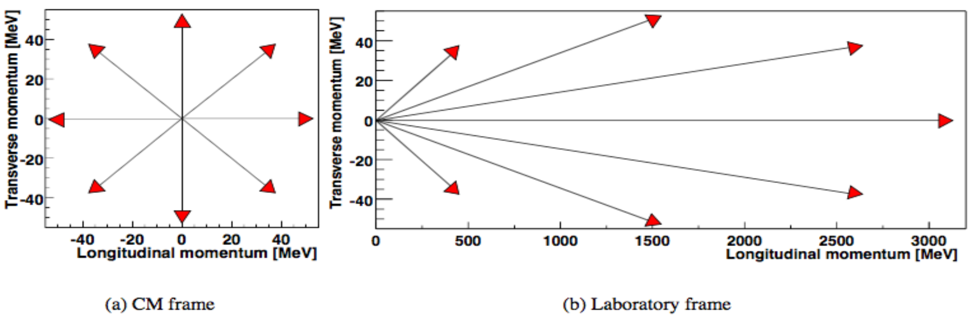

(a) CM frame

(b) Laboratory frame

Figure 1.6: Illustration of the Lorentz boost of the decay positron from the muon rest frame to the laboratory frame.

Consequently, the number of particles detected above such a threshold as a function of time is modulated with the frequency ω_a [1].
An example of positron arrival time histogram appears in Figure 1.7. The oscillations from

the anomalous precession are indeed present as expected, visible on top of an exponential baseline that results from the decay of the muon population. In the absence of any instrumental backgrounds, this spectrum is described by the functional form

$$N(t) = N_0 e^{-t/\tau}[1 + Acos(\omega_a t + \phi)] \tag{1.20}$$

where τ is the muon lifetime, the magnitude of the amplitude A is determined by the energy cut, and the phase ϕ depends on the initial polarization of the muon ensemble [16].
The value of ω_a is extracted by fitting this functional form to the data.

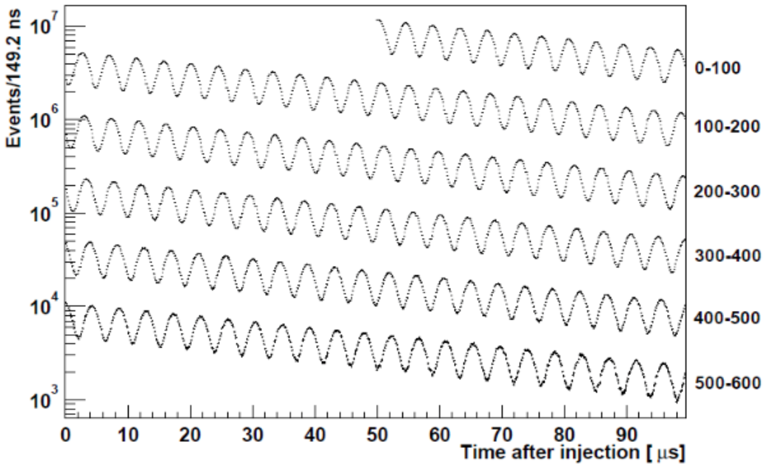

Figure 1.7: Spectrum of arrival times for decay electrons (positrons) with detected energies greater than $2\,GeV$ (BNL experiment).

It must be emphasized that ω_a is proportional to a_μ not to g. The experiment directly measures only the perturbations to the magnetic moment, permitting three orders of magnitude higher precision than if it measured the entire quantity.

Chapter 2

Theoretical calculation of a_μ

2.1 Standard Model contribution: overview of the calculation

At the current experimental precision it is necessary to calculate contributions from many sectors of theory, i.e. Quantum Electrodynamics (QED), Electroweak Theory (EW), and Quantum Chromodynamics (QCD). As such, it is customary in the Standard Model calculation to separate a_μ^{SM} into its constituent parts:

$$a_\mu^{SM} = a_\mu^{QED} + a_\mu^{EW} + a_\mu^{HVP} + a_\mu^{HOHVP} + a_\mu^{HLBL} \tag{2.1}$$

where the QCD contribution has been further divided into three distinct terms.
With a contribution nearly two million times the experimental error, a_μ is vastly dominated by QED. The next most significant contribution comes from the lowest-order hadronic vacuum polarization, which is 116 times larger than the experimental error [16].
Although a_μ is dominated by QED, both this and electroweak contributions are well established at the required level of precision [1], therefore the error on the Standard Model comes almost entirely from the hadronic terms: the comparison between theory and experiment is largely confined to the hadronic sector.

2.1.1 The QED contribution

The QED contribution to the anomalous magnetic moment of the muon is defined as the contribution arising from the subset of SM diagrams containing only leptons (e, μ, τ) and photons. As a dimensionless quantity, it can be cast in the following general form:

$$a_\mu^{QED} = A_1 + A_2(m_\mu/m_e) + A_2(m_\mu/m_\tau) + A_3(m_\mu/m_e, m_\mu/m_\tau) \tag{2.2}$$

where m_e, m_μ and m_τ are the masses of the electron, muon and tau respectively.
The term A_1, arising from diagrams containing only photons and muons, is mass independent[1]. On the other hand, the terms A_2 and A_3 are functions of the indicated mass ratios

[1]This term is the same for QED contribution to the anomalous magnetic moment of all three charged leptons.

and are associated with graphs containing closed fermion loops where the fermion differs from the external one; for the muon as the external lepton we have two possibilities:

- an additional electron-loop (light-in-heavy), $A_2(m_\mu/m_e)$: it is proportional to large logarithms $\propto ln(m_\mu/m_e)^2$, thus it's a huge correction;
- an additional τ-loop (heavy-in-light), $A_2(m_\mu/m_\tau)$: it produces, because of the decoupling of heavy particles in QED, only small effects of order $\propto (m_\mu/m_\tau)^2$ [13].

The renormalizability of QED guarantees that the function A_i $(i = 1, 2, 3)$ can be expanded as power series in (α/π) and computed order-by-order:

$$A_i = A_i^{(2)}\left(\frac{\alpha}{\pi}\right) + A_i^{(4)}\left(\frac{\alpha}{\pi}\right)^2 + A_i^{(6)}\left(\frac{\alpha}{\pi}\right)^3 + A_i^{(8)}\left(\frac{\alpha}{\pi}\right)^4 + A_i^{(10)}\left(\frac{\alpha}{\pi}\right)^5 + ...$$

Only one diagram, shown in Figure 1.2, is involved in the evaluation of the lowest order contribution[2]; it provides the famous result by Schwinger [14] where $A^{(2)} = 1/2$.
Going beyond A_i expression, more than one hundred diagrams are involved in the evaluation of the three-loop (sixth-order) QED contribution. Their analytic computation required approximately three decades, ending in the late 1990s.
More than one thousand diagrams enter the evaluation of the four-loop QED contribution to a_μ. As only few of them are known analytically [25], this eighth-order term has thus far been evaluated only numerically. This formidable task was first accomplished by Kinoshita and his collaborators in the early 1980s [6] [26].
One should realize that this eighth-order QED contribution, being about six times larger than the present experimental uncertainty of a_μ, is crucial for the comparison between the SM prediction of a_μ and its experimental determination.
The evaluation of the five-loop QED contribution is in progress [27].

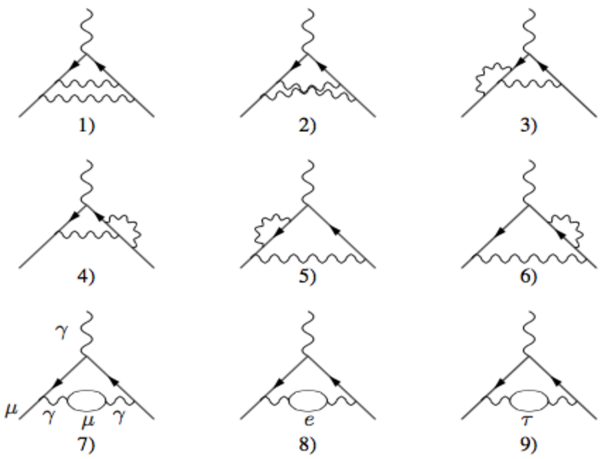

Figure 2.1: Diagrams 1-7 represent the universal second order contribution to a_μ, diagram 8 yields the "light", diagram 9 the "heavy" mass dependent corrections [13].

[2]Second order in the electric charge.

All these contributions lead to [28]:

$$a_\mu^{QED} = (116\,584\,718.95 \pm 0.08) \times 10^{-11} \tag{2.3}$$

The error is given by the uncertainties in α, in the mass ratios, by the numerical error on α^4 terms and the guessed uncertainty of the α^5 contribution[3][13].

2.1.2 The EW contribution

The Feynman diagrams for the leading-order weak interaction contributions to a_μ are illustrated in Figure 2.2. They are topologically similar to the Schwinger diagram in QED, but they contain virtual W , Z, and Higgs bosons rather than photons[4] [1].
Since the Fermi coupling constant $G_F \propto 1/m_W^2$, the electroweak terms are suppressed by $(m_\mu/m_W)^2$. Relative to the entire QED-dominated anomaly a_μ, the perturbation from single-loop W exchange is approximately 3.3 ppm. The single-loop Z exchange reduces the overall EW contribution with a negative fractional value of -1.6 ppm.
The single-loop Higgs contribution has an additional suppression of $(m_\mu/m_W)^2$ relative to the other exchange bosons, and so does not contribute significantly to the single-loop calculation [16].

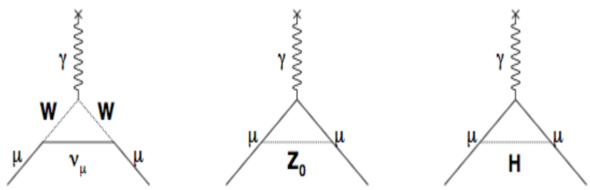

Figure 2.2: Feynman diagrams for the lowest-order weak corrections to a_μ [1].

As a_μ is a physical observable one can calculate it directly in the non-renormalizable unitary gauge [1].
The analytic expression for the one-loop EW contribution to a_μ, due to the diagrams in Figure 2.2, reads:

$$a_\mu^{EW} = \frac{5G_\mu m_\mu^2}{24\sqrt{2}\pi^2}\left[1 + \frac{1}{5}(1 - 4sin^2\theta_W)^2 + \mathcal{O}\left(\frac{m_\mu^2}{m_{Z,W,H}^2}\right)\right] \tag{2.4}$$

where [5] $G_\mu = 1.16638(1) \times 10^{-5}$ GeV^{-2}, $sin^2\theta_W \equiv 1 - m_W^2/m_Z^2 \simeq 0.231$, $m_\mu = 105.658$ MeV/c^2, $m_Z = 91.188$ GeV/c^2, $m_W = 80.385$ GeV/c^2 and $m_H = 125.6$ GeV/c^2.

[3]The uncertainty of the α^3 term is negligible.
[4]The Higgs exchange diagram is included for completeness.

In the approximation where tiny terms $O(m_\mu^2/m_{W,Z}^2)$ are neglected, the gauge boson contributions are given by [29]:

$$a_\mu^{(2)EW}(W) = \frac{\sqrt{2}G_\mu m_\mu^2}{16\pi^2}\frac{10}{3} \simeq (388.70 \pm 0.10)\ \times\ 10^{-11}$$
$$a_\mu^{(2)EW}(Z) = \frac{\sqrt{2}G_\mu m_\mu^2}{16\pi^2}\frac{(-1+4s_W^2)^2-5}{3} \simeq (-193.89 \pm 2)\ \times\ 10^{-11} \tag{2.5}$$

For the Higgs exchange, one finds a negligible contribution:

$$a_\mu^{(2)EW}(H) = \frac{\sqrt{2}G_\mu m_\mu^2}{4\pi^2}\int_0^1 dy \frac{(2-y)y^2}{y^2+(1-y)(m_H/m_\mu)^2}$$
$$= \frac{\sqrt{2}G_\mu m_\mu^2}{4\pi^2}\frac{m_\mu^2}{m_H^2} ln\frac{m_H^2}{m_\mu^2} \quad \sim 5\ \times\ 10^{-14} \tag{2.6}$$

Using the SM parameters, the a_μ^{EW} (1 loop) prediction is:
$a_\mu^{(2)EW} = (194.82 \pm 0.02)\ \times\ 10^{-11}$, where the error is due to the uncertainty[5] in s_W^2 (the sinus squared of the Weinberg angle).
As first noticed in 1992 [30], a_μ^{EW}(2 loop) is actually quite substantial because of the appearance of terms enhanced by a factor of $ln(m_{Z,W}/m_f)$, where m_f is a fermion mass scale much smaller than m_W[19]. This negative contribution has been re-evaluated using the LHC value of the Higgs mass [31]:

$$a_\mu^{(4)EW} = (-19.97 \pm 0.03)\ \times\ 10^{-11} \tag{2.7}$$

Here the remaining parametric uncertainty results from the experimental uncertainties of the input parameters m_H and to a smaller extent of m_W.
Three-loop (and higher-order) contributions were found to be entirely negligible.
Indeed, they are even smaller than one would expect because of a fortunate cancellation between the quark and lepton sectors [1].

2.1.3 The QCD contribution

On a perturbative level we may obtain the hadronic vacuum polarization contribution by replacing internal lepton loops in the QED Vacuum Polarization (VP) contributions by quark loops, adapting charge, color multiplicity and masses accordingly [13].
Since QCD is non perturbative at low energies, the hadronic contribution cannot be calculated analytically as a perturbative series, but it can be expressed in terms of the cross section of the reaction $e^+e^- \to hadrons$ [1], which is known from experiments, using analyticity and unitarity (the optical theorem) [32].
The leading Hadronic Vacuum Polarization (HVP) process is determined via the dispersion relation [13]:

$$a_\mu^{HVP} = \left(\frac{\alpha m_\mu}{3\pi}\right)^2 \left(\int_{m_{\pi^0}^2}^{E_{cut}^2} \frac{R(s)}{s^2}\tilde{K}(s)ds + \int_{E_{cut}^2}^{\infty} \frac{R^{pQCD}(s)}{s^2}\tilde{K}(s)ds\right) \tag{2.8}$$

[5] One-loop contributions suppressed by m_μ^2/m_Z^2 or m_μ^2/m_H^2 are smaller than 10^{-13} and hence neglected here.

where $\tilde{K}(s) \to 1$ at $s >> m_\mu^2$ and $R(s)$ is the measured cross section of e^+e^- annihilation into hadrons in units of $\sigma(e^+e^- \to \mu^+\mu^-)$. The integral Equation 2.8 is written in terms of the rescaled function:

$$\tilde{K}(s) = \frac{3s}{m_\mu^2} K(s)$$

In the integration over s, two regions have to be distinguished: the non-perturbative part (threshold region) to be evaluated from the data and the perturbative high energy tail (resonance region) to be calculated using perturbative QCD (pQCD). In the threshold region $s \sim 4m_\pi^2$ [33]:

$$R(s) \approx \frac{1}{4}\left(1 - \frac{4m_\pi^2}{s}\right)^{3/2} \tag{2.9}$$

In the resonance region $s \sim m_\rho^2$ and the quark-hadron duality gives:

$$R(s) \approx N_c \sum Q_q^2 \tag{2.10}$$

with N_c number of colours.

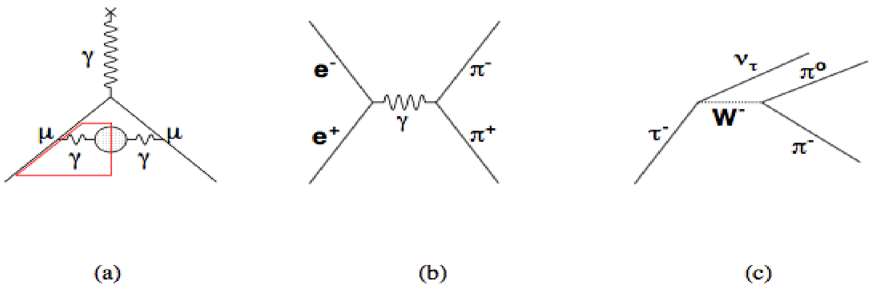

Figure 2.3: Feynman diagrams for (a) hadronic vacuum polarization, (b) dominant hadron production process $e^+e^- \to \pi^+\pi^-$, and (c) equivalent τ decay process $\tau^- \to \nu_\tau \pi^- \pi^0$ [1].

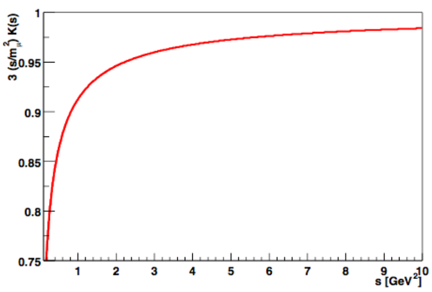

Figure 2.4: Graph of $3\frac{s}{m_\mu^2}K(s)$ versus s, illustrating that it asymptotically approaches 1 at high energies [1].

Intuitively, the dispersion relation 2.8 isolates the portion of the vacuum polarization diagram drawn in a box in Figure 2.3 (a), splitting the hadronic state in half and connecting the virtual photon to incoming e^+ and e^- lines. The resulting real hadron production diagram is shown in Figure 2.3 (b). The leading-order behavior of the QED Kernel $K(s)$ is proportional to $1/s$; this property is illustrated by the graph of $3(s/m_\mu^2)K(s)$ vs. s in Figure 2.4 which trends asymptotically to 1 for large s [1].

The cross section $\sigma(s)$ itself also decreases roughly as $1/s$. Consequently, the integral is dominated by low-energy data; almost 92% of the contribution to a_μ arises from energies below 1.8 GeV, with nearly two thirds coming solely from the $\pi^+\pi^-$ channel [16].
The experimental data for the low energy region are shown in Figure 2.5.

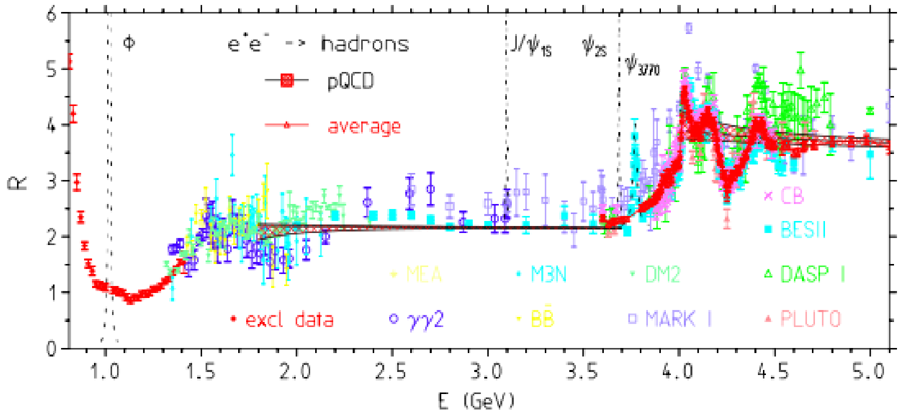

Figure 2.5: Experimental results for $R_\gamma^{had}(s)$ in the range 1 GeV $< E = \sqrt{s} <$ 5 GeV, obtained at the various e^+e^- storage rings. The perturbative quark-antiquark production cross-section is also displayed (pQCD) [13].

The hadronic contribution a_μ^{HVP} is of order 7000×10^{-11}. Of course, this is a small fraction of the total SM prediction for a_μ, but is very large if compared with the current experimental uncertainty $\delta a_\mu^{EXP} = 60 \times 10^{-11}$.
Indeed, as δa_μ^{EXP} is less than one percent of a_μ^{HVP}, precision analyses of this hadronic term as well as full treatment of its higher-order corrections are clearly warranted [19].
Higher-order contributions (HOHVP) contain an HVP insertion along with an additional loop. The additional loop can be a photon that is emitted and reabsorbed, a leptonic pair, or a second HVP insertion.
The calculation is similar to the first-order HVP in that it requires experimental input from $R(s)$ [13]:

$$a_\mu^{HOHVP} = \frac{2}{3}\left(\frac{\alpha}{\pi}\right)^3 \int_{4m_\pi^2}^{\infty} \frac{R(s)}{s} K^{(2)}(s/m_\mu^2) ds \tag{2.11}$$

and knowledge of the kernel $K^{(2)}(s)$ for higher-order loops. The contribution to a_μ from higher-order three-loop hadronic diagrams is calculated to be [34]:

$$a_\mu^{HOHVP} = (-9.8 \pm 0.1) \times 10^{-10} \tag{2.12}$$

Overall, the error on the calculation of HOHVP is small when compared to the first-order term. The HOHVP term includes all higher-order hadronic contributions, with the exception of a special class of interactions known as hadronic light-by-light (HLbL) scattering. The hadronic light-by-light contribution cannot at present be determined from data, but rather must be calculated using hadronic models that correctly reproduce properties of QCD. This contribution is shown below in Figure 2.6 [35]. It is dominated by the long-distance contribution shown in Figure 2.6 (*b*). In fact, in the so called chiral limit, where the mass gap between the pseudoscalars (Goldstone-like) particles and the other hadronic particles (the ρ being the lowest vector state in Nature) is considered to be large and to leading order in the $1/N_c$-expansion, this contribution has been calculated analytically [36] and provides a long-distance constraint to model calculations. There is also a short-distance constraint from the operator product expansion (OPE) of two electromagnetic currents which, in specific kinematic conditions, relates the light-by-light scattering amplitude to an Axial-Vector-Vector triangle amplitude for which one has a good theoretical understanding [37].

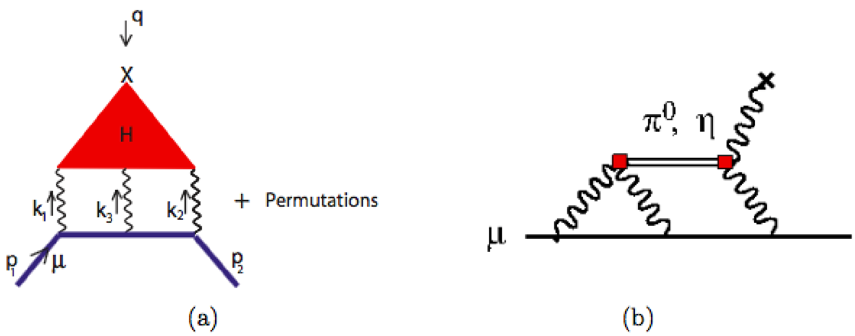

Figure 2.6: (*a*) The hadronic light-by-light contribution; (*b*) the pseudoscalar meson contribution [35].

Unfortunately, the two asymptotic QCD constraints mentioned above are not sufficient for a full model independent evaluation of the HLbL contribution [35]. Most of the last decade calculations found in the literature are compatible with the QCD chiral and large-N_c limits. They all incorporate the π^0- exchange contribution modulated by $\pi^0\gamma^*\gamma^*$ form factors correctly normalized to the Adler-Bell-Jackiw point-like coupling. They differ, however, on whether or not they satisfy the particular OPE constraint mentioned above, and in the shape of the vertex form factors which follow from the different models.
A synthesis of the model contributions, which was agreed by authors from each of the leading groups that have been working in this field, can be found in Ref. [38].
They obtained:

$$a_\mu^{HLbL} = (105 \pm 26) \times 10^{-11} \tag{2.13}$$

2.1.4 Summary of Standard Model contribution: open issues

The latest measurement of the anomalous magnetic moment of negative muons by the experiment E821 at Brookhaven is [39]

$$a_\mu^{EXP} = (116592089 \pm 63) \times 10^{-11} \tag{2.14}$$

The total uncertainty includes a 0.46 ppm statistical uncertainty and a 0.28 ppm systematic uncertainty, combined in quadrature. This result is in good agreement with the

average of the measurements of the anomalous magnetic moment of positive muons [40], [41], [42], [43], as predicted by the CPT theorem [44].
This experimental value has to be compared with the SM value computed as in Equation 2.1, for which different contributions are listed in Table 2.1.
The difference between the experimental and the theoretical value, depending on which evaluation of the lowest-order hadronic contribution is used, is [35]:

$$\Delta a_\mu(E821 - SM) = (287 \pm 80) \ \times \ 10^{-11} \quad [45]$$

$$= (261 \pm 78) \ \times \ 10^{-11} \quad [46]$$

	Value ($\times 10^{-11}$ units)
QED (γ + l)	$116\,584\,718.951 \pm 0.009 \pm 0.019 \pm 0.007 \pm 0.077_\alpha$
HVP (lo) [45]	$6\,923 \pm 42$
HVP (lo) [46]	$6\,949 \pm 43$
HVP (ho) [46]	-98.4 ± 0.7
HLbL	105 ± 26
EW	154 ± 1
Total SM [45]	$116\,591\,802 \pm 42_{HLO} \pm 26_{HHO} \pm 2_{other} (\pm 49_{tot})$
Total SM [46]	$116\,591\,828 \pm 43_{HLO} \pm 26_{HHO} \pm 2_{other} (\pm 50_{tot})$

Table 2.1: Summary of the Standard-Model contributions to the muon anomaly. Two values are quoted because of the two recent evaluations of the lowest-order hadronic vacuum polarization [35].

QED and EW

The QED and EW contributions to a_μ are well understood. Recently the four-loop QED contribution has been updated and the full five-loop contribution has been calculated [47].

Hadronic vacuum polarization

The main conceptual problems remain with the hadronic contributions which are limiting the theoretical precision. The hadronic vacuum polarization requires substantial improvement and will depend very much on new improved e^+e^- annihilation experiments in particular in the range up to 2.5 GeV.
An important long term project is the calculation of non-perturbative terms of the vacuum polarization function in lattice QCD [48].

Hadronic light-by-light scattering

In view of recent and foreseeable progress in computer performance, and using recently developed much more efficient computer simulation algorithms, it is expected that lattice QCD will be able to provide an useful estimate in coming years.

The main problem at present is the limited precision of the e^+e^- data in the range between 1 and 2 GeV.
The hadronic light-by-light scattering contribution will then be limiting further progress in the prediction of g-2 [13].

While the theoretical predictions for the QED and EW contributions appear to be ready to rival these precisions, much effort will be needed in the hadronic sector to test a_μ^{SM} at an accuracy comparable to the experimental one. Such an effort is certainly well motivated by the excellent opportunity the muon g-2 is providing us to unveil or constrain "New Physics" effects [19].

2.2 Possible contributions to a$_\mu$ from New Physics

Although the SM is very well established as a renormalizable Quantum Field Theory (QTF) and describes essentially all experimental data of laboratory and collider experiments, it is well established that the SM is not able to explain a number of fundamental facts.
The SM fails to account for the existence of non-baryonic cold dark matter (at most 10 % is normal baryonic matter), the matter-antimatter asymmetry in the universe, which requires baryon-number B and lepton-number L violation at a level much higher than in the SM, the problem of the cosmological constant and so on.
A complete theory should include the 4th force of gravity in a natural way and explain the difference between the weak and the Planck scale (hierarchy problem).
If we confront an accurately predictable observable with a sufficiently precise measurement of it, we should be able to see that our theory is incomplete. New Physics can manifest itself through states or interactions which have not been seen by other experiments, either by a lack of sensitivity or, because the new state was too heavy to be produced at existing experimental facilities or, because the signal was still buried in the background [13].
The anomalous magnetic moment of the muon provides one of the most precise tests of Quantum Field Theory as a basic framework of elementary particle theory and of QED and the electroweak SM in particular. But not only that, it also constrains Physics beyond the SM severely [13].
The comparison of theoretical and experimental values for a_μ is interesting, regardless of the outcome. If the values differ, then the comparison provides evidence for Physics beyond the Standard Model. If they agree, then the result constrains any proposed speculative extension, assuming that there are no fine-tuned cancellations between different varieties of New Physics [1].
This section describes several generic examples of interesting New Physics probed by a_μ^{EXP}- a_μ^{SM}. Rather than attempting to be inclusive, it focuses on three general scenarios:

- Muon compositeness;
- Supersymmetric loop effects;
- Existence of an Electric Dipole Moment (EDM).

2.2.1 Muon compositeness

The vast spectrum of hadrons is explained by the quark model; in the same way, fundamental "preons" [49] might be able to account for the existence of multiple generations of leptons. The magnetic moments of the proton and the neutron are far different from 2 because they are composed of quarks. One would therefore expect a perturbation to a_μ if the muon was formed of smaller constituents.
An initial model is represented by the tree-level Feynman diagrams in Figure 2.7.
First, each vertex at which a muon interacts with another particle is multiplied by a form factor $\left(1+\frac{q^2}{\Lambda^2}\right)$, where $\Lambda = 1/r$ is the characteristic energy scale, to account for the spatial extent of the charge distribution.
Second, the muon may enter excited states in which the constituents have acquired relative orbital angular momentum.
Finally, there may be contact interactions among the constituents that do not correspond to the usual exchange of gauge bosons [1].

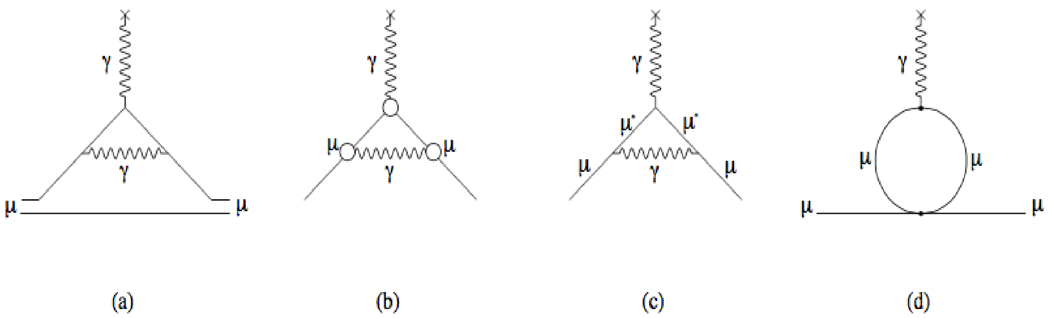

Figure 2.7: Feynman diagrams for (a) the leading-order effect of compositeness, which must be canceled out in a workable model; (b) a form factor at each $\mu\gamma$ interaction vertex; (c) excited lepton states; (d) four-fermion contact interactions [50].

However, in each case the contribution to a_μ is proportional to $\left(\frac{m_\mu}{\Lambda}\right)^2$ [50].

2.2.2 Supersimmetry

The most promising theoretical scenarios for New Physics are supersymmetric extensions of the SM, in particular the Minimal Supersymmetric Standard Model (MSSM).
Supersymmetry (SUSY) implements a symmetry mapping [13]:

$$boson \leftrightarrow fermion$$

between bosons and fermions, by changing the spin by $\pm\frac{1}{2}$ units [51].
Every boson has a fermion partner, and every fermion has a boson partner.
There is no experimental evidence for the partner particles. The symmetry must therefore be broken by the addition of "soft" terms to the Lagrangian; otherwise, the masses of the paired fermions and bosons would be the same, and the partners would have been seen long ago [1].

SUSY associates with each SM state X a supersymmetric "s-state" $\tilde{X}$ where sfermions are bosons and sbosons are fermions.
In addition, in the Minimal Supersymmetric Standard Model (MSSM), there must be at least one extra Higgs doublet which also has its SUSY partners [13]: one Higgs doublet gives mass to the upper half of each generation (the u, c, and t quarks), and the other to the lower half (the d, s, and b quarks).
Of the four Higgs states, two are electrically neutral, one is positively charged, and one is negatively charged [1]. The ratio:

$$tan\beta = \frac{\nu_2}{\nu_1}$$

of the vacuum expectation values of the two Higgs doublets is an important parameter describing the nature of Supersymmetry.

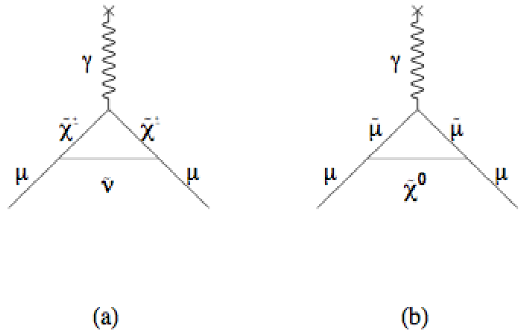

Figure 2.8: Feynman diagrams for the lowest-order supersymmetric contributions to a_μ [1].

The lowest-order supersymmetric contributions to a_μ are shown in Figure 2.8.
The photino, zino, wino, and Higgsinos are not mass eigenstates; they are rearranged into linear combinations called neutralinos and charginos, represented by $\tilde{\chi}^0$ and $\tilde{\chi}^{\pm}$.
They are identical in form to the dominant Standard Model Electroweak corrections.
The symbol $\tilde{\mu}$ represents the smuon while $\tilde{\nu}$ stands for the sneutrino.
To illustrate the scale of these contributions, the masses of the supersymmetric particles can be taken to be degenerate at $\tilde{m}$ yielding [52]:

$$|a_\mu^{SUSY}| \approx \left(\frac{\alpha(m_Z)}{8\pi sin^2\theta_W}\right)\left(\frac{m_\mu}{\tilde{m}}\right)^2\left(1-\frac{4\alpha}{\pi}ln\frac{\tilde{m}}{m_\mu}\right)tan\beta$$

$$\approx 13 \times 10^{-10}\left(\frac{100\,GeV}{\tilde{m}}\right)^2 tan\beta$$

If $tan\beta$ is as large as 40, then a_μ is sensitive to mass scales $\tilde{m}$ of up to 800 GeV [1].
Were SUSY particles to be discovered at LHC, the muon anomaly would play an important role in helping to discriminate between the different possible scenarios and providing measure of $tan\beta$ [3].

2.2.3 Electric dipole moment (EDM)

The EDM is a direct measure of T-violation, which in a QFT is equivalent to a CP-violation. Since extensions of the SM in general exhibit additional sources of CP violation, EDMs are very promising probes of New Physics [13].
In modern notation, the magnetic dipole moment (MDM) interaction becomes:

$$\bar{u}_\mu \left[eF_1(q^2)\gamma\beta + \frac{ie}{2m_\mu} F_2(q^2)\sigma_{\beta\delta}q^\delta \right] u_\mu \tag{2.15}$$

where $F_1(0) = 1$, and $F_2(0) = a_\mu$. The electric dipole moment interaction is:

$$\bar{u}_\mu \left[\frac{ie}{2m_\mu} F_2(q^2) - F_3(q^2)\gamma_5 \right] \sigma_{\beta\delta}q^\delta u_\mu \tag{2.16}$$

where $F_2(0) = a_\mu$ and $F_3(0) = d_\mu$, with[6]

$$d_\mu = \left(\frac{\eta}{2}\right)\left(\frac{e\hbar}{2mc}\right) \simeq \eta \times 4.7 \times 10^{-14}\, e\, cm \tag{2.17}$$

The existence of an EDM implies that both P and T are violated. This can be seen by considering the non-relativistic Hamiltonian for a spin one-half particle in presence of both an electric and magnetic field: $\mathcal{H} = -\vec{\mu} \cdot \vec{B} - \vec{d} \cdot \vec{E}$. The transformation properties of $\vec{E}$, $\vec{B}$, $\vec{\mu}$ and $\vec{d}$ are given in Table 2.2, showing that while $\vec{\mu} \cdot \vec{B}$ is even under all three, $\vec{d} \cdot \vec{E}$ is odd under both P and T. While parity violation has been observed in many weak processes, direct T violation has only been observed in the neutral kaon system. In the context of CPT symmetry, non null EDM value implies CP violation, which is allowed by the Standard Model for decays in the neutral kaon and B-meson sector [53].
The muon spin motion is modified by the presence of an electric dipole moment.

	$\vec{E}$	$\vec{B}$	$\vec{\mu}$ or $\vec{d}$
P	-	+	+
C	-	-	-
T	+	-	-

Table 2.2: Transformation properties of the electric and magnetic field and the dipole moments.

The total frequency becomes $\vec{\omega} = \vec{\omega_a} + \vec{\omega_\eta}$ where

$$\vec{\omega_\eta} = -\frac{q}{m}\left[\frac{\eta}{2}\left(\frac{\vec{E}}{c} + \vec{\beta} \times \vec{B}\right)\right] \tag{2.18}$$

with η defined by Equation 2.17. The spin motion resulting from the motional electric field, $\vec{\beta} \times \vec{B}$ is the dominant effect, so $\vec{\omega}_\eta$ is transverse to $\vec{B}$. A non null EDM would have two effects on the precession, there would be a slight tipping of the precession plane, which

[6]This η, which is the EDM analogy to g for the MDM, should not be confused with the Michel parameter η.

Particle	Present EDM Limit ($e\,cm$)	Standard Model Value ($e\,cm$)
n	$2.9 \times 10^{-26}\,(90\,\%CL)$[54]	10^{-31}
e^-	$1.6 \times 10^{-27}\,(90\,\%CL)$[55]	10^{-38}
μ	$1.9 \times 10^{-19}\,(E821)(95\,\%CL)$[56]	
^{199}Hg	$2.1 \times 10^{-28}\,(95\,\%CL)$[57]	

Table 2.3: Present limits on the electric dipole moments [53].

would cause a vertical oscillation of the centroid of the decay electrons (direct effect) and the observed precession frequency ω would be larger (indirect effect) [53]:

$$\omega = \sqrt{\omega_a^2 + \left(\frac{q\eta\beta B}{2m}\right)^2} \tag{2.19}$$

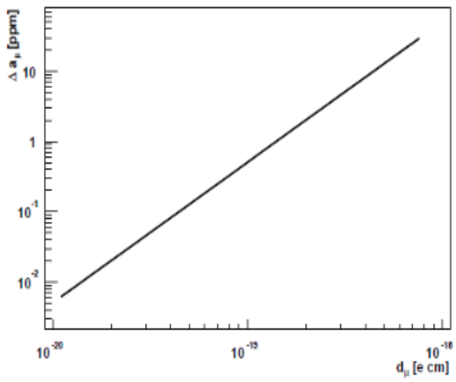

Figure 2.9: Perturbation to the measured value of a_μ as a function of the electric dipole moment d_μ.

To reduce systematic errors in the muon EDM measurement, a “frozen spin” technique has been proposed which uses a radial electric field in a muon storage ring, operating at $\gamma << \gamma_{magic}$ to cancel the g-2 precession. The EDM term would cause the spin to steadily move out of the plane of the storage ring. Electron detectors above and below the storage region would detect a time-dependent up-down asymmetry that increases with time. As in the g-2 experiments, detectors placed in the plane of the beam would be used, in this case to make sure that the radial-E-field cancels the normal spin precession exactly [58].

Other New Physics effects

It must be emphasized that the three topics addressed in this chapter are by no means the only models that have been analyzed in terms of a_μ. Other possibilities include leptoquarks, radiative muon mass generation, anomalous gauge boson properties, and compact extra dimensions. A review of some of these scenarios has been written by Czarnecki and Marciano [52].

Chapter 3

Measuring a_μ: history of the experiments

The reason why the muon anomalous magnetic moment is so interesting and plays a key role in Elementary Particle Physics at its fundamental level is due to the fact that it can be predicted by theory with very high accuracy and at the same time can be measured as precisely in an unambiguous experimental setup [13]. The experimental evolution in parallel with the improvement of the theoretical prediction will be examined.

3.1 Early muon experiments

The first measurement of the g-factor of the muon was performed in 1957 by Garwin and collaborators at the Nevis cyclotron [59]. Muons, formed in-flight from pion decay, were passed one at time through an entrance counter and stopped in a carbon target.

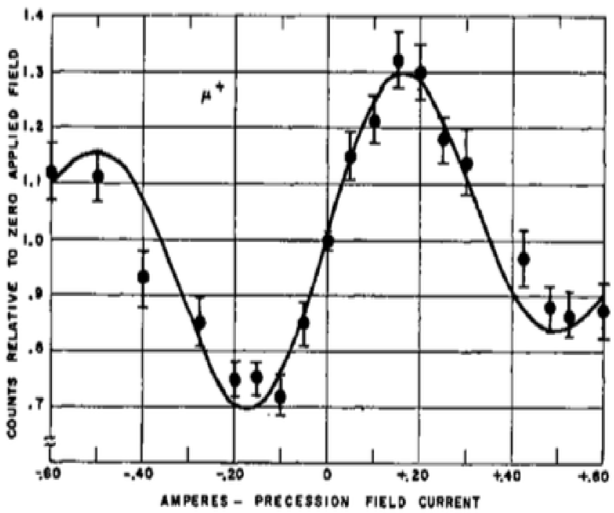

(a) Garwin data

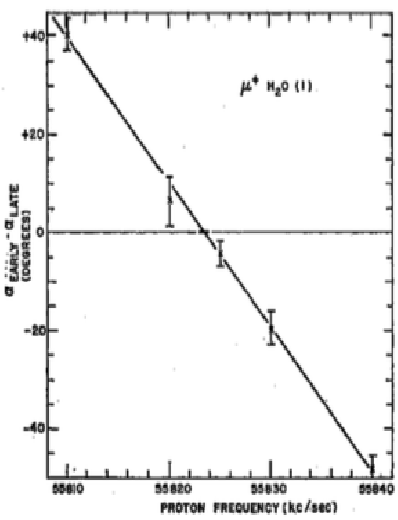

(b) Hutchinson data

Figure 3.1: Historical plots showing Larmor precession data from the (a) Garwin and (b) Hutchinson experiments used to determine the g-factor of the muon [16].

An external magnetic field, applied in the target region, caused the muon spin to precess. The amount of precession in a fixed time interval could be increased or decreased by adjusting the strength of the field. The counts measured in a fixed counter were plotted as a function of the applied field; using $\vec{\omega}_s = g\frac{e}{2mc}\vec{B}$ they were able to determine $g = 2.00 \pm 0.10$ for the muon. The experimental error was initially too large to spot the anomaly of the muon. The data from the Garwin experiment as it was originally published is shown in Figure 3.1 (*a*).
Over the course of the next five years, the determination of the muon g-factor improved as several other groups continued to perform Larmor precession type experiments on stopped muon sources [60-64]. The highest precision reached by this method was achieved by Hutchinson and collaborators [65] in 1963 by stopping muons in a magnetic field and measuring the early-to-late phase difference between a standard reference and peaks in the decay electron distribution. As shown in Figure 3.1 (*b*), the Larmor precession frequency can be measured by plotting the phase difference at a fixed time interval as a function of the reference clock frequency. Fitting the data for the zero crossing allows for a precise determination of the Larmor precession frequency.
Hutchinson and his group measured the Larmor precession frequency and the magnetic field to a 10 ppm precision, but the comparison with theory was in the end limited by the 100 ppm uncertainty in the muon mass [16].

3.2 CERN Experiments

a_μ was measured by a succession of three experiments of increasing precision and complexity at CERN, starting from 1958 and concluding in 1977, based on the principle of measuring the anomalous spin precession directly.

3.2.1 First CERN Experiment

The design of CERN I experiment fully exploited the initial muon polarization and final decay electron asymmetry in the framework of the idea that it should be possible to store muons in a conventional bending magnet which provided an approximately uniform vertical field [66].
Polarized muons were injected into a 6 m long magnet. Once in the 1.5 T magnet, the muons lost energy and consequently followed small orbits which could be contained within the magnetic field region, as shown in Figure 3.2 (*a*).
To prevent them from re-entering the absorber after one turn, a small transverse gradient of the magnetic field was introduced, causing the orbits to drift along the length of the magnet [66]. Vertical focusing was added by carefully shimming the magnetic field to be parabolic in the vertical direction:

$$B(y) = B_0(1 + ay + by^2)$$

where B_0 determined the average radius of the orbit, the strength of the gradient a caused each orbit to advance along the magnet, and a non-zero coefficient b produced a quadratic field, which provided vertical focusing.
The amount of time spent in the field could be varied by tuning the gradient.

The muons were then stopped in a polarimeter outside the magnet in which their front/back decay asymmetry was measured; this asymmetry was plotted as a function of storage time to determine ω_a [1].
The amount the muon spin had precessed relative to the momentum was determined by the amount of time spent in the magnetic field, or in other words the number of orbits. The number of orbits had a natural variance depending on the exact y-position at which the muon entered the apparatus [16].

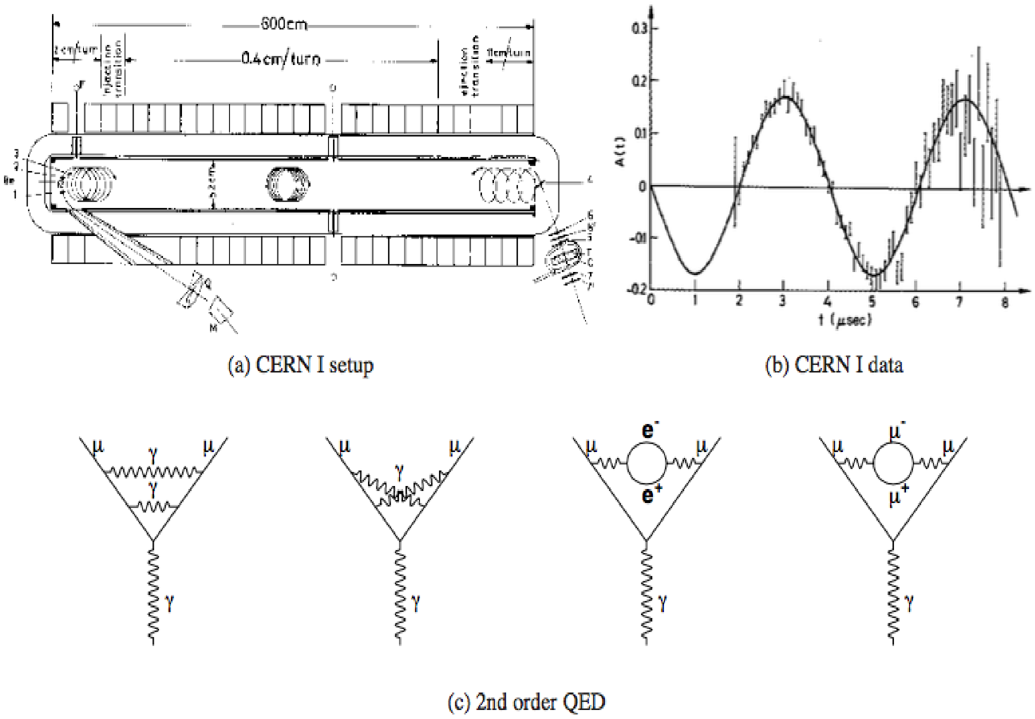

(a) CERN I setup

(b) CERN I data

(c) 2nd order QED

Figure 3.2: (*a*) An overview of the CERN I experimental setup and (*b*) and the published data [67]; (*c*) Some of the Feynmann diagrams required in calculating the second-order QED probed by CERN I.

The average asymmetry versus time is plotted in Figure 3.2 (*b*).
The experiment obtained a result with an uncertainty of 4300 ppm that agreed with the prediction of Quantum Electrodynamics (QED) for a structureless particle:

$$a_\mu^{EXP}(1965) = 0.001\,162(5) \;\Rightarrow \pm\,4300\,ppm$$

Physicists of the time expected a deviation because of the larger muon mass, but here was the proof that, to good precision, the muon can be treated in QED as though it is merely a heavy electron. The precision of the CERN I results motivated a QED calculation complete to second order in α, with the result [68]:

$$a_\mu^{TH}(1965) = 0.001\,165\,52(5) \Rightarrow \pm\,42\,ppm$$

where the error of 5×10^{-8} comes from the uncertainty in virtual loops containing hadronic matter. The uncertainty of the final result from the CERN I experiment was dominated

by statistical error, so the main obstacle for a new experiment was to find a method of increasing the statistical power.
The prospects for improving a_μ can be understood by examining the terms of the expression:

$$N(t) = N_0 e^{-t/\tau}[1 + Acos(\omega_a t + \phi)]$$

which is used to fit the data. The fractional error on ω_a is [69]:

$$\frac{\delta\omega_a}{\omega_a} = \frac{\sqrt{2}}{\omega_a A \tau \sqrt{N}}$$

In addition to the obvious improvement in statistical power gained through increasing N, the precision can be improved by increasing any of the other factors in the denominator:

- the anomalous precession frequency ω_a is proportional to the magnetic field, so one option is to increase the field strength, thus generating more cycles to be fit;
- another possibility is to use higher-energy muons so that the lifetime τ has been relativistically enhanced;
- finally, the asymmetry of the signal A can be improved by using better detectors and choosing an appropriate energy level to maximize the imbalance in the parity violating decay electrons [16].

3.2.2 Second CERN Experiment

The role of the g-2 experiment as the best test of QED at short distances had been established: it was necessary to design a new experiment which would press the accuracy of the measurement to finer limits. In order to do so, it was of paramount importance to increase the muon intensity, and in the second CERN g-2 experiment this was done by producing pions in a target immediately adjacent to the storage ring [66].
The second CERN experiment [70] used a 5 m diameter storage ring with a muon momentum of 1.3 GeV/c; it allowed to measure a_μ for both μ^+ and μ^- at the same machine. A radial magnetic field gradient was used to focus the beam. The primary proton beam was injected directly into an internal target on one side of the ring. Pions were produced at the target: forward-going pions were captured in the 1.7 T field in the storage ring. As the pions decayed, longitudinally polarized muons with a relativistic γ-factor of 12 were captured by the storage ring: just a small fraction of the muons were produced within the accepted phase space of the ring.
The decay electrons from the stored muons were of slightly lower momentum, so they bent radially in-ward. Therefore, the decay electron signal was measured by placing detectors around the inside of the storage ring. Due to the background[1] produced at the target, a large shielding block prevented placing detectors everywhere around the ring.
The experimental setup is shown in Figure 3.3 (a), and the decay electron data is shown in the upper half of the plot in Figure 3.3 (b).
A sample of the data, showing the bunch structure at early times, is shown in the bottom

[1]That was a tremendous flash of prompt radiation when the beam was injected.

half of Figure 3.3 (b).
They were able to measure:

$$a_\mu^{EXP}(1968) = 0.001\,166\,16(31) \Rightarrow \pm\,270\,ppm$$

The increased precision from the CERN II experiment required theorists to start considering the hadronic contributions to vacuum polarization, shown in Figure 3.3 (c). Including the light-by-light calculation, the new theory value

$$a_\mu^{TH}(1969) = 0.001\,165\,87(3) \Rightarrow \pm\,25\,ppm$$

and the experimental results were in good agreement.

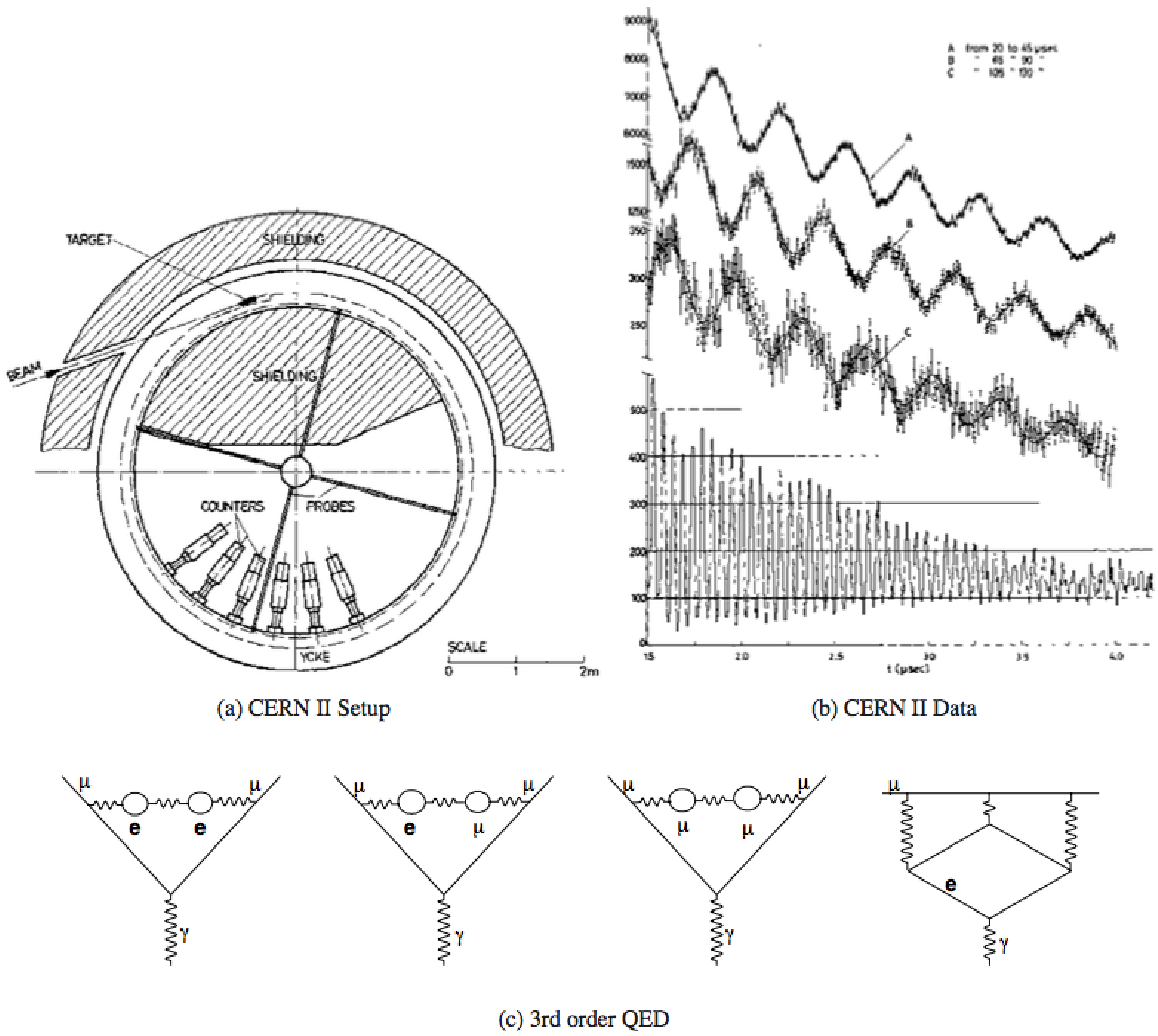

(a) CERN II Setup

(b) CERN II Data

(c) 3rd order QED

Figure 3.3: (a) An overview of the CERN II experimental setup and (b) and the published data [70]; (c) Feynmann diagrams used to calculate the third-order QED correction to a_μ. The light-by-light diagram on the far right was the original source of the discrepancy between theory and experiment [16].

The systematic error was entirely due to the radial variation in the magnetic field required to provide vertical confinement. An alternate method of vertical confinement

was to use a quadrupole electric field. The problem with an electric field arose from the fact that a relativistic muon would "see" the lab frame electric field as a magnetic field in the muon's rest frame: a new term would be introduced in the relation between ω_a, a_μ and B, as it is clear in Equation 1.18.
If the coefficient of that term[2] could be made zero, then a measurement of the electric field was no longer required. It turned out that for the correct relativistic enhancement:

$$\gamma = \sqrt{\frac{1}{a_\mu} + 1}$$

the coefficient is precisely zero. Nature was even "kind enough" to place the "magic momentum" for the muon at $p_\mu = 3.09$ GeV/c, which corresponded to a momentum that was easily attainable at the CERN 28 GeV Protonsynchrotron (PS) [16].
With the concept of the magic momentum the design of CERN III began [71].

3.2.3 Third CERN Experiment

Many of the principles learned with CERN II were put to good use and the whole injection scheme was revisited.
Rather than injecting protons into the ring, the background could be greatly reduced by locating the target outside of the storage ring. Pions could then be transported to the inner part of the ring by using an inflector to cancel the strong fields in the backleg of the magnet; no shielding blocks were required so detectors could be placed all around the interior circumference, thus increasing the statistics. By transporting pions to the ring through a beamline, a very narrow range of pion momenta could be selected and the subsequent polarization of the stored muons was much higher. Finally, the magic momentum meant that the relativistic lifetime of the muons was precisely 64.4 μs, more than a factor of two more dilated than in CERN II.
Essentially, every factor in the denominator of Equation 3.1 was improved with the CERN III design.
The increased statistical precision is apparent in the data shown in Figure 3.4 (b) where the precession signal is discernible for over 500 μs, as opposed to the CERN II data in Figure 3.3 (b) where the wiggles are only visible for 130 μs [16].
After combining data for both the positive and negative muon, the final result from the CERN III experiment was:

$$a_\mu^{EXP}(1979) = 0.001\,165\,924(8.5) \Rightarrow \pm\,7\,ppm$$

where the 7 ppm error is dominated by the statistical uncertainty.
With a theoretical prediction of

$$a_\mu^{TH}(1969) = 0.001\,165\,87(3) \Rightarrow \pm\,25\,ppm$$

it confirmed the importance of hadronic vacuum polarization at the 5σ level.
The precision of 7 ppm was an extraordinary achievement at that time.

[2]Related to the electric field.

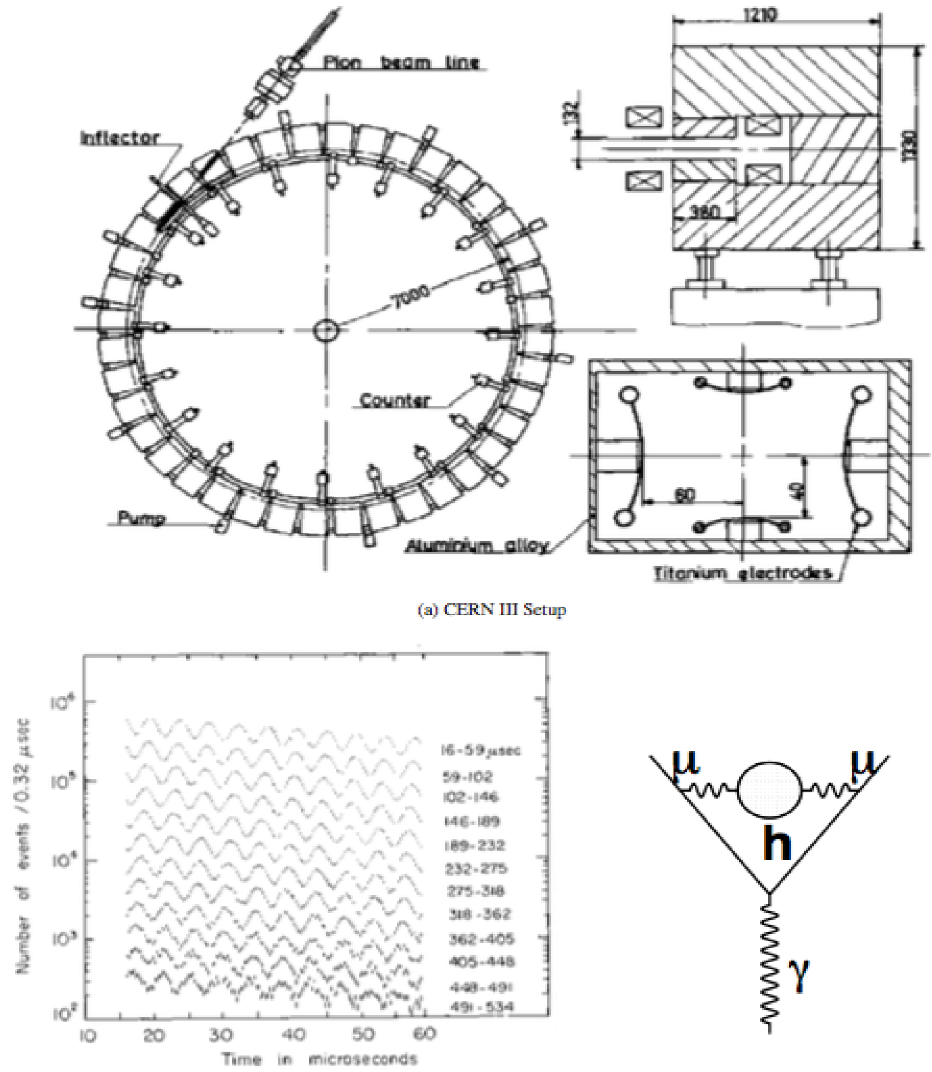

(a) CERN III Setup

(b) CERN III Data

(c) Hadronic diagram

Figure 3.4: (*a*) An overview of the CERN III apparatus and (*b*) the published data [71]; (*c*) Feynmann diagram depicting the contribution to a_μ from hadronic vacuum polarization that was first probed by CERN III [16].

For the first time the m_μ^2/m_e^2-enhanced hadronic contribution came into play.
With the achieved precision the muon g-2 remained a benchmark for beyond the SM theory builders ever since. Only 20 years later the BNL experiment E821, again a muon storage ring experiment run at the magic energy, was able to set new standards in precision.
Of course it was the hunting for deviations from theory and the theorists speculations about "New Physics around the corner" which challenged new experiments again and again [13].

3.3 The Brookhaven Experiment

The 7 ppm error in the CERN III experiment was dominated by statistics, which indicated that the method of operating a storage ring at a field corresponding to the "magic momentum" had not yet been systematically exhausted [16].
The key improvements of the BNL experiment included the very high intensity of the primary proton beam from the proton storage ring Alternating Gradient Synchrotron (AGS) that was capable of producing 60×10^{12} protons every 2.7 s, which was about a factor of 20 higher than the luminosity of the PS at CERN [72]. A second large increase in statistics was required to achieve a sub-ppm measurement: this improvement came from the injection of muons instead of pions into the storage ring; in the previous design, in fact, muons from circulating pions having a lower momentum could not be kept for long inside the same orbit and only few muon decays were detectable. An additional expedient was a super-ferric storage ring magnet with increased storage efficiency that allowed higher intensity with lower background: this change required, in addition to an inflector, a pulsed kicker magnet [1].
Furthermore the decay electron (positron) signals from the calorimeters were recorded by waveform digitizers and stored for later analysis instead of relying on a hardware trigger [16].
This list is by no means exhaustive, but it does represent some of the key issues in keeping the systematics under control.
The ring had a diameter of $\sim$ 14 m, the aperture of the beam pipe was 90 mm, the field was 1.45 T and the momentum of the muon $p_\mu = 3.094$ GeV. The muon spin was precessing with angular frequency ω_s, which is slightly bigger than ω_c by the difference in angular frequency $\omega_a = \omega_s - \omega_c$ [13].

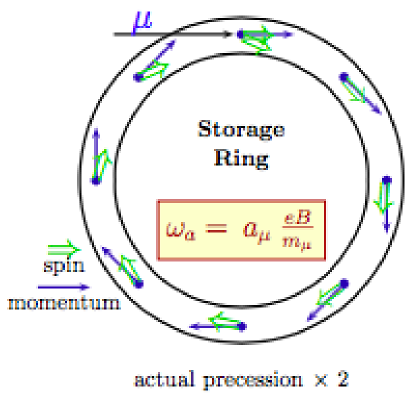

Figure 3.5: Spin precession in the g-2 ring ($\sim 12°$/circle) [13].

After nearly 15 years of development, the first data were collected by the BNL experiment in 1997. The experiment continued to take data with positive muons in 1999 and 2000, where an eventual precision of 0.7 ppm was obtained for a_μ. The decay positron data from 2000 is shown in Figure 3.6. The improvement in the statistical power relative to CERN can be observed by comparing Figure 3.6 to Figure 3.4.
Positively charged muons were preferred for the first measurements due to the enhanced cross section for producing π^+ at the target. This 20 % increase relative to π^- can be attributed to conservation of charge from the parent proton beam.
It was not until 2001, the last year of data collection, that the charge species of the experiment was changed to μ^-: by measuring μ^+ and μ^- with equal precision, a constraint on CPT violation can be determined for the muon sector [16].

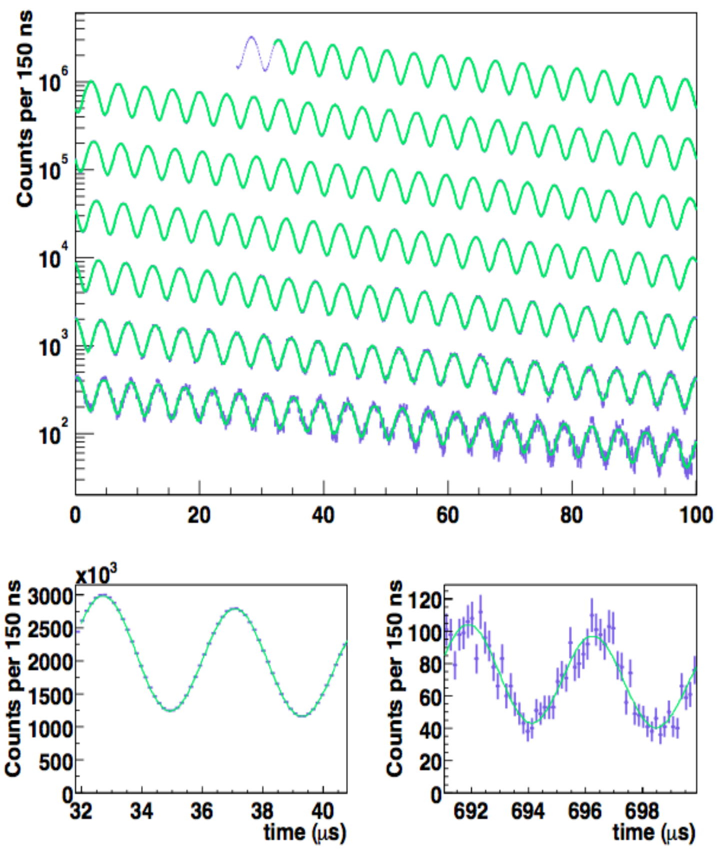

Figure 3.6: Decay positron data from 2000 with a five parameter fit of the form in Equation 1.20 overlayed [16],[7].

The results of the CERN and BNL experiments are summarized in Table 3.1.
To underscore the huge improvement over time in experimental precision, the most recent measurements are presented graphically in Figure 3.7.

Experiment	Year	Polarity	$a_\mu \times 10^{10}$	Precision [ppm]	Reference
CERN I	1961	μ^+	11 450 000(220 000)	4300	[73], [22]
CERN II	1962-1968	μ^+	11 661 600(3100)	270	[70], [22]
CERN III	1974-1976	μ^+	11 659 100(110)	10	[71], [22]
CERN III	1975-1976	μ^-	11 659 360(120)	10	[71], [22]
BNL	1997	μ^+	11 659 251(150)	13	[74]
BNL	1998	μ^+	11 659 191(59)	5	[40]
BNL	1999	μ^+	11 659 202(15)	1.3	[41]
BNL	2000	μ^+	11 659 204(9)	0.7	[7]
BNL	2001	μ^-	11 659 214(8)	0.7	[75]
Average			11 659 208.0(6.3)	0.54	[75]

Table 3.1: Summary of a_μ results from various experiments and data sets, showing the evolution of experimental precision over time.

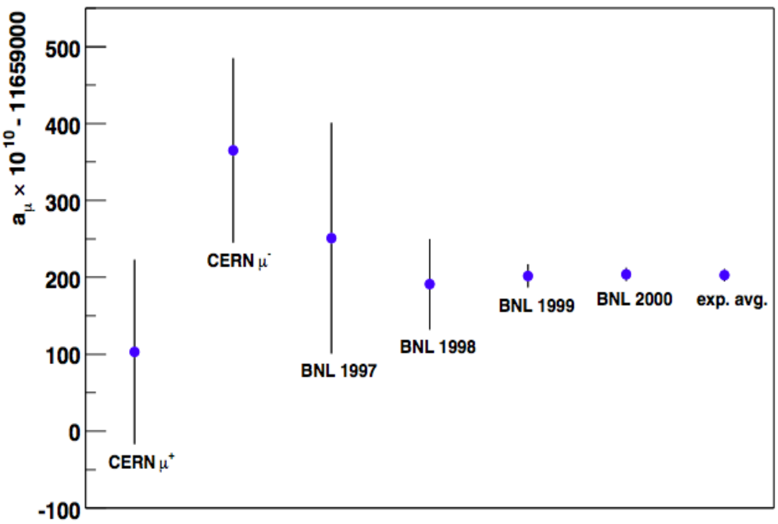

Figure 3.7: Comparison of a_μ results from various experiments and data sets [1].

Since the first results were published, a persistent "discrepancy" between theory and experiment of about 3 standard deviations was observed. It was the largest "established" deviation from the Standard Model seen in a "clean" electroweak observable and thus could be a hint for New Physics to be around the corner [13].

Chapter 4

The *g-2* experiment at Fermilab

4.1 Experiment overview

The error achieved by the BNL E821 experiment was $\delta a_{\mu}^{EXP} = 6.3 \times 10^{-10}$ (0.54 ppm) [39]. The greater than 3σ difference found by E821 with respect to the theoretical expectation, was limited and does not meet the 5σ threshold for claiming a discovery, so a more precise measurement is needed to rule out statistical fluctuations and confirm the discrepancy.
The goal of the g-2 experiment at Fermilab is a four-fold improvement in the experimental precision thereby reducing the error on a_{μ} up to 0.14 ppm which is comparable to the 0.4 ppm uncertainty on the most accurate Standard Model prediction [76].

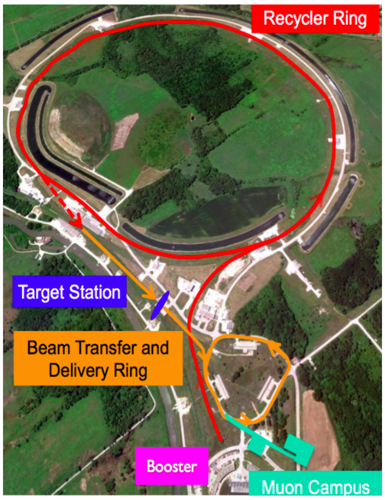

Figure 4.1: Overview of Fermilab complex.

While BNL E821 improved on the CERN III experiment in a revolutionary manner, primarily by the invention of direct muon injection into the storage ring, the FNAL E989 experiment will introduce a broad suite of refinements focused on optimizing the beam purity and rate, the muon storage efficiency, and modernizing the instrumentation used to measure both ω_a and ω_p [77].
E989 will use the same muon storage ring of E821, which has been relocated to Fermi-

lab in a new building characterized by mechanical stability and controlled temperature. These options were not available at BNL [78].
The E989 experiment will measure a_{μ^+} during the first run, due to the enhanced cross section for producing π^+ at the target and due to the fact that negative muons tend to be captured in matter more often than positive muons; a_{μ^-} though may be measured in a second run. Theoretically, a_{μ^+} should be equal to a_{μ^-}, but measuring both provides a way to perform a CPT theorem test. Since the values measured for a_{μ^+} and a_{μ^-} in the E821 experiment were statistically consistent, the E821 Collaboration averaged the two values to produce their final experimental value for a_μ [79].

Many improvements are needed with respect to the previous experiment to reach the statistical uncertainty of 0.1 ppm as requested. Some of these improvements are [80]:

- higher proton rate with less protons per bunch: since the detected positron number is directly proportional to the protons on target, the Fermilab experiment will have to deliver 4×10^{20} protons; indeed, it will be possible to reach these numbers by using the Fermilab beam complex which is expected to annually deliver (2.3×10^{20}) 8 GeV protons on an Inconel[1] core target; at this rate, the desired number of protons, and thus positrons[2], will be achieved in less than two years of running [78];

- 900 m pion decay line: a limiting factor at BNL was the 120 m beamline between the pion production target and the storage ring; because the decay length of a 3.11 GeV/c pion is $\approx$ 173 m, the beam injected into the storage ring contained both muons and a significant number of undecayed pions, the latter creating an enormous burst of neutrons when intercepting materials: their subsequent capture in scintillator-based detectors impacted detector performance adversely [77]; this background will be reduced by a factor of 20 in E989;

- 510 times larger muon yield per proton and 510 times as many muons stored per hour than that at BNL; the muon storage ring will be filled at a repetition rate of 12 Hz, which is the average rate of muon spills that consists of sequences of successive 700 μs spills with 11 ms spill-separations, compared to 4.4 Hz at BNL [78];

- improved detectors against signal pileup and new electronics: the detectors and electronics will all be newly constructed to meet the demands of measuring the spin precession of the muon to a statistical error of 0.1 ppm, while controlling systematics on ω_a to the 0.07 ppm level; this is a substantial improvement over the E821 experiment. Better gain stability and corrections for overlapping events in the calorimeters are crucial improvements addressed in the new design.
  A new tracking system will allow for better monitoring of the stored muon population, thus improving the convolution of the stored muon population with the magnetic field volume, and establishing corrections to ω_a that arise from electric field and pitch corrections, which are related to vertical particle oscillations (pitch effect): the vertical undulation of the muons means $\vec{p}_\mu$ is not exactly perpendicular

[1] Inconel is an alloy, composed of a metal and other elements, specially designed to withstand high beam stresses.

[2] The total data set must contain more than 1.8×10^{11} detected positrons with energy greater than 1.8 GeV.

to $\vec{B}$, thus a small "pitch" correction is necessary at the current and proposed levels of experimental precision [81];

- better shimming to reduce B-field variations: the storage ring magnetic field, and thus ω_p, will be measured with an uncertainty that is approximately 2.5 times smaller by placing critical Nuclear Magnetic Resonance (NMR) probes at strategic locations around the ring and shimming the magnetic field to achieve a high uniformity, in addition to other incremental adjustments [82];

- a continuous monitoring and re-calibration of the detectors, whose response may vary on both the short timescale of a single fill, and the long time scale of an entire run, will be required: a high-precision laser calibration system that will monitor the gain fluctuations of the calorimeter photodetectors at 0.04 % accuracy will be used [80].

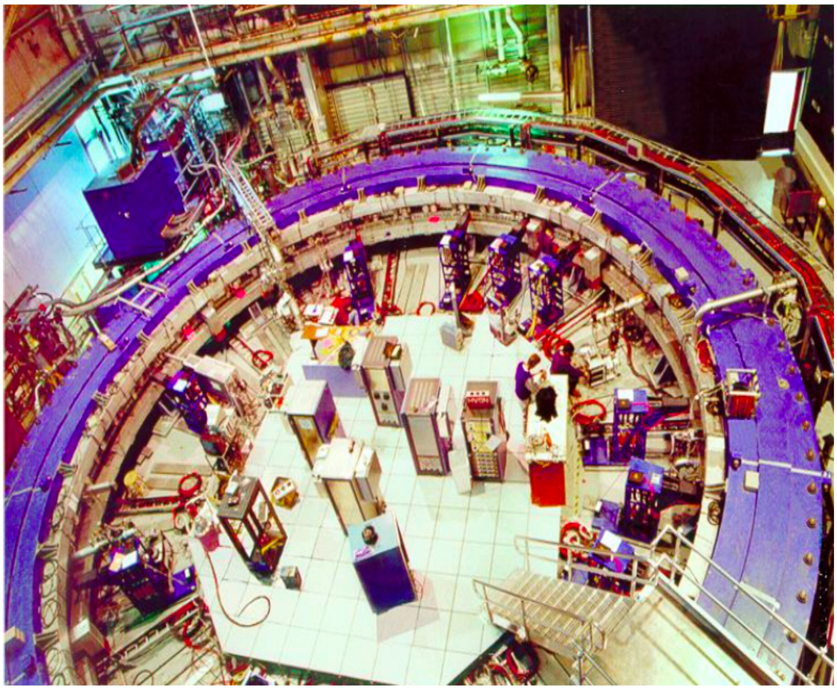

Figure 4.2: BNL/FNAL storage ring.

Experimental technique

E989 will bring a bunched beam from the 8 GeV Fermilab Booster, which is a synchrotron accelerator with a circumference of 474 m, to a pion production target located where the antiproton production target was in the Tevatron collider program [76]. Pions will pass through a bending magnet to select particles with a momentum of 3.1 GeV ($\sim 10\,\%$), and subsequently will traverse a decay line of ~ 1 Km which results in a pure muon beam entering the storage ring [78].

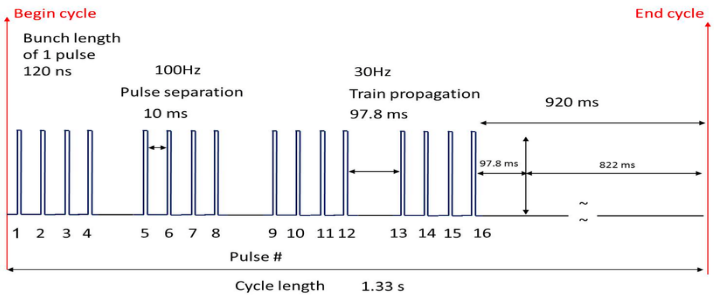

Figure 4.3: Bunch structure.

The pions and daughter muons will be injected into the Delivery Ring, the re-purposed $\bar{p}$ debuncher ring, where after several turns the remaining pions decay. The polarized muons will be collected, transferred through the inflector magnet, and injected into the same 14 m-diameter muon storage ring used for the E821 experiment at Brookhaven [79].

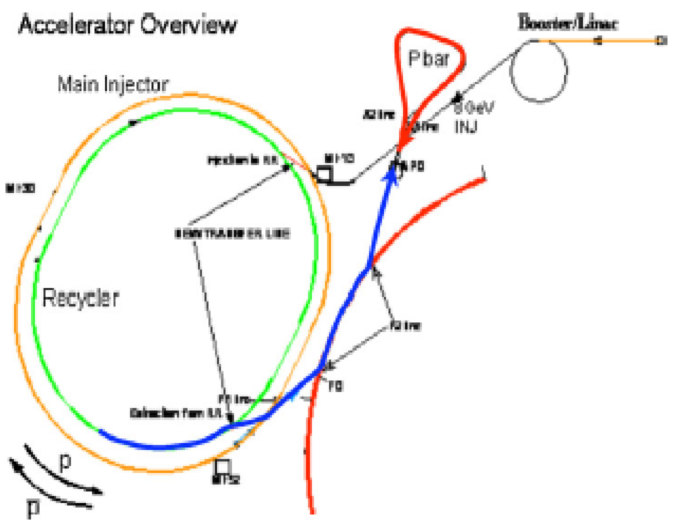

Figure 4.4: Accelerator overview (FNAL).

The muon kicker will have an optimized pulse-forming network, which is an electric circuit composed of capacitors that provide a square pulse with a flat top upon discharge, that will provide a pulse close to the beam width, as opposed to the E821 kicker which had a pulse width longer than the cyclotron period [78]. A 10 mrad kick is required to put magic momentum muon onto a stable orbit after injection.
The beam will enter through a hole in the "back-leg" of the magnet and then will cross into the inflector magnet, which provides an almost field free region, delivering the beam to the edge of the storage region; the new superconducting inflector is characterized by a limited flux leakage onto the storage region and a larger horizontal beam aperture to allow a higher storage efficiency [78].
The geometry is rather constrained, as can be seen in Figure 4.5 (a). The injection geometry is sketched in Figure 4.5 (b).

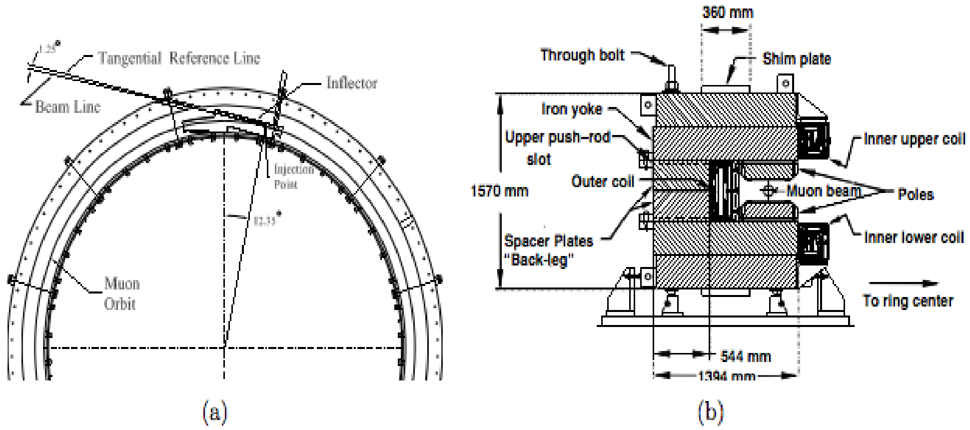

Figure 4.5: (*a*) Plan view of the beam entering the storage ring; (*b*) Elevation view of the storage-ring magnet cross section [76].

Finally, the electron/positron energy and the number of high energy electrons/positrons detected as a function of time will be measured by calorimeters and trackers, throughout the storage ring [79].
The calorimeters will use Silicon Photomultipliers (SiPMs) to read signals from lead-fluoride crystals ($Pb\,F_2$).
Since momentum spread, betatron oscillations, and muon distribution introduced ppm level corrections in the anomalous precession at BNL, E989 will exploit in-vacuum straw drift tubes as tracking detectors to better understand beam dynamics, limit pile up effects and provide an independent validation of the systematic uncertainties analysis (for example, an independent momentum measurement).
The electronics and data acquisition systems will be upgraded to handle the increased rate of data taking and to record all information related to the run for monitoring and for the application of corrections in the analysis stage [78].

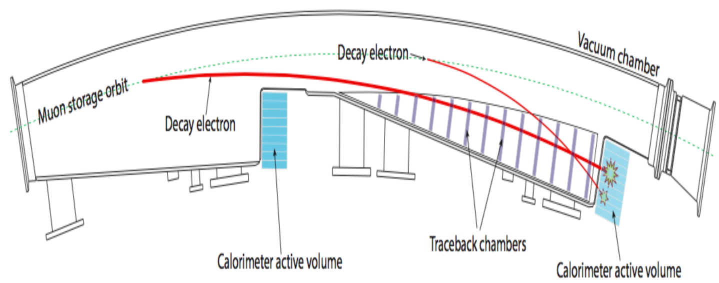

Figure 4.6: Detectors overview.

E989 uncertainties

The systematic errors on the anomalous precession frequency ω_a, and on the magnetic field normalized to the proton Larmor frequency ω_p, are each targeted to reach the $\pm\,0.07$ ppm level. E989 will have three main categories of uncertainties [76]:

Category	E821 [ppb]	E989 Improvement Plans	Goal [ppb]
Gain changes	120	Better laser calibration	
		low energy threshold	20
Pileup	80	Low-energy samples recorded	
		calorimeter segmentation	40
Lost muons	90	Better collimation in ring	20
CBO	70	Higher n value (frequency)	
		Better match of beamline to ring	< 30
E and pitch	50	Improved tracker	
		Precise storage ring simulations	30
Total	180	Quadrature sum	70

Table 4.1: The largest systematic uncertainties for the final E821 ω_a analysis and proposed upgrade actions and projected future uncertainties for E989 analysis; CBO stands for Coherent Betatron Oscillation [76].

- statistical: the uncertainty $\delta\omega_a$ from the fits will be purely statistical (assuming a good fit). The final uncertainty depends on the size of the data set used in the fit, which in turn depends on the data accumulation rate and the running time;
- ω_a systematics: additional systematic uncertainties that will affect $\delta\omega_a$ might be anything that can cause the extracted value of ω_a from the fit to differ from the true value, beyond statistical fluctuations. Categories of concern include the detection system (e.g., gain stability and pileup immunity), the incoming beamline (lost muons, spin tracking), and the stored beam (coherent betatron oscillations, differential decay, E and pitch correction uncertainties);
- ω_p systematics: the magnetic field is determined from proton NMR. The uncertainties are related to how well known are the individual steps from absolute calibration to the many stages of relative calibration and time-dependent monitoring.
  The "statistical" component to these measurements is negligible.

Analysis Methods Summary

The standard analysis procedure is to identify individual decay positrons and plot the rate of their arrival versus time using only events having a measured energy above a threshold.
The number of detected positrons above a single energy threshold E_{th} is

$$N(t; E_{th}) = N_0 e^{-t/\gamma\tau_\mu}[1 + Acos(\omega_a t + \phi)] \tag{4.1}$$

Here the normalization, N_0, the average asymmetry, A, and the initial phase, ϕ, are all dependent on the energy threshold.
This function is used to fit the results from the T (Time) Method analysis and extract ω_a. The T Method, whose application to simulated data is shown in the top panel of Figure 4.7, is sufficient to reach the experimental goal [76].

Pileup causes an early-to-late phase shift; because ϕ is highly correlated to ω_a, this effect leads to a a significant contribution in the systematic uncertainty of ω_a [83].
However the possibility to extract more statistical precision from the data set has been investigated: by weighting events in proportion to their energy, or the asymmetry associated with their energy, the statistical precision is improved.
Thus an alternative method, the so-called Q Method, has been developed.
In the Q Method, individual events are not identified, but rather the detector current[3] is integrated as a function of time, and ω_a can subsequently be extracted from this time-distribution [83]. This method, using energy-weighted events, has the attractive feature of being immune to the systematic effect of pileup. It was not used in E821 due to memory and readout limitations, but will be implemented in E989.
An example of the spectrum that would result from a T or Q Method analysis using the same simulated data set is shown in Figure 4.7.
The main features of three T-based and of the Q-based methods are outlined below [76]:

- T Method: events in the calorimeter are individually identified, sorted and fit to obtain time and energy. The events vs. time-in-fill histogram is built from all events with reconstructed energy above a threshold. All events in the histogram are given equal weight. The figure-of-merit (FOM) is maximized for a positron energy threshold of 1.86 GeV. The quantity ω_a is obtained from a fit to a pileup-subtracted histogram. This is the standard method used in E821 and the benchmark for determining the statistical and systematic requirements for the E989 experiment;

- E-Weighted Method: identical to the threshold T Method except that the histogram is built by incrementing a time bin with a weight equal to the energy of an event, therefore producing the energy vs. time-in-fill histogram;

- A-Weighted Method: identical to the threshold T Method except that the histogram is built by incrementing a time bin with the average value of the asymmetry corresponding to that positron energy. This technique yields the maximum possible statistical power for a given threshold using the event identification technique;

- Q Method: an alternative approach whereby the detector current - a proxy for the deposited energy - is digitized and plotted as a function of time. It is an energy-weighted analysis with a single very low threshold, since events do not need to be individually identified. This procedure leads to a histogram of energy vs. time-in-fill. No attempt to correct for pileup is necessary here and a very low threshold is desired. The statistical power of this approach almost reaches that of the threshold T method.

All of the mentioned analysis techniques will be applied to the data set by different research groups throughout the collaboration. A combination of the results of the different methods will enable a small reduction in the final uncertainty of ω_a; more importantly, the two main methods (T and Q) will also serve as an important cross checks on the final result because they have very different sensitivities to various systematic uncertainties.
The analysis will be conducted in a blind fashion.

[3] Which is proportional to the energy deposited in the calorimeter vs. time from the decay positrons.

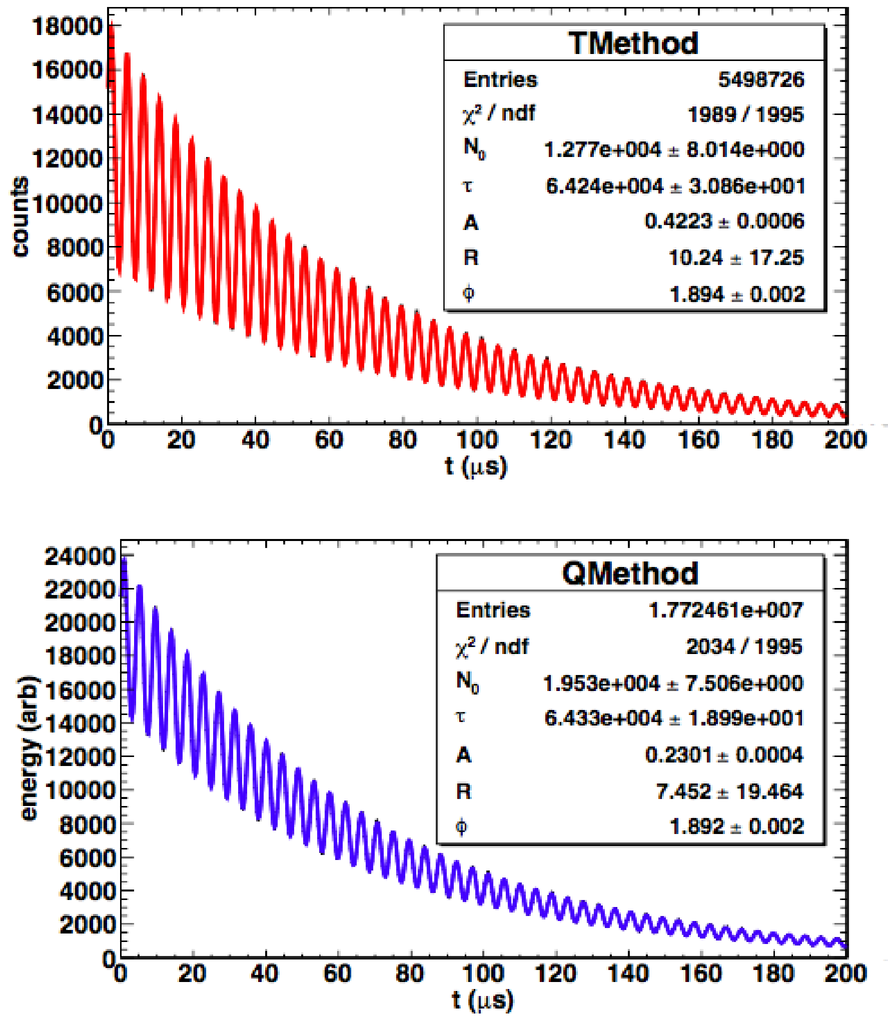

Figure 4.7: Top: Monte Carlo data analyzed using the T method with a threshold cut at $y = 0.6$. Bottom: Same data analyzed using the Q method. Detector acceptance is included. The asymmetry A is much higher for the T method; however, the Q method has many more events (N). The ω_a Monte-Carlo truth is $R = 0$ and the uncertainty in R is a measure of the precision, in ppm. Both methods give a similar statistical uncertainty and acceptable fit central values [76].

Detector System

The detector system for E989 is entirely new, as is the supporting electronics, and the fast and slow data acquisition systems. The detector system will include [81]:

- an entrance scintillating paddle and several sets of scintillating fiber hodoscopes to determine the incoming muon beam intensity profile vs. time and space;
- two sets of rebuilt scintillating fiber hodoscopes placed in the path of the stored muons to measure (somewhat destructively) the stored beam x-y profile in two locations; these detectors will be used to optimize the storage and measure the

coherent betatron motion; they will be rotated out of the way for normal data taking;

- three sets of in-vacuum straw trackers that reside in the scallop of the vacuum chamber adjacent to the muon storage volume; they will provide data of decay positron tracks that can be "traced back" to the point of tangency from the muon that decayed. This track will provide a transverse stored-muon profile vs. time-in-fill. They will be also useful to calibrate the calorimeters and will be sensitive to an electric dipole moment of the muon (See Section 4.3);
- 24 stations of electromagnetic calorimeters that will be positioned to maximally intercept the higher-energy decay positrons and determine their time of arrival and energy.

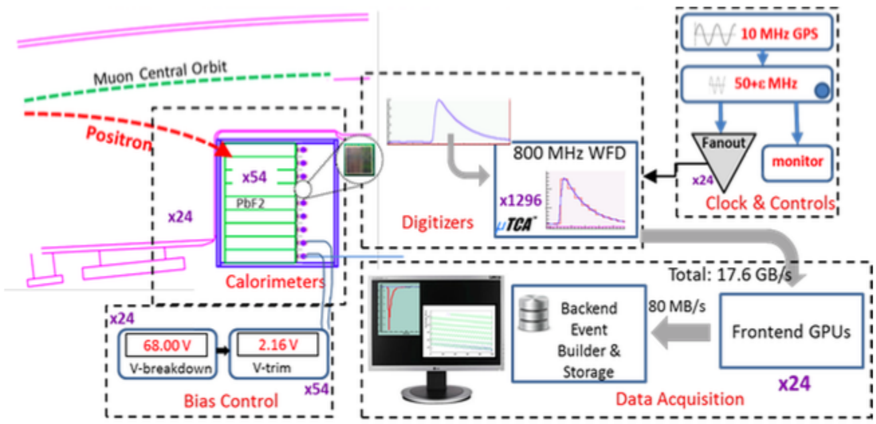

Figure 4.8: Schematic of the relationship of a number of the ω_a subsystems. The dashed boxes represent distinct responsibilities of different groups within the collaboration [76].

Several subsystems are required to make calorimeters work and to record data: they are shown schematically in Figure 4.8.
First a segmented array of PbF_2 crystals absorbs the energy of the positrons and converts it to Cherenkov light.
Then the light is detected by SiPMs. These devices produce a pulse that is digitized separately for each block by custom digitizers running at 800 MSPS[4] with 12 bit depth. The digitized signals are passed to a farm of graphics processing units (GPUs) where they are reduced to a form suitable for storage. In the case of the event reconstruction style analysis (T Method) regions of interest or "islands" are selected for recording. In the case of the current readout analysis (Q Method) the waveforms are summed across several digitizer samples as well as within individual stations to reduce the size of the recorded data.
The proposed SiPM readout devices are particularly sensitive to bias and temperature stability. Dedicated subsystems to provide a stable bias supply to each device and to

[4]MSPS stands for Megasamples per second.

monitor temperature inside the calorimeter enclosures are being tested (See "Bias Voltage System for SiPMs" for details).
Tracker stations will gather data that contains a large number of resolved two-track events that might appear as unresolved pileup in the calorimeters. These data will be crucial to develop the calorimeter cluster and pileup-subtraction routines. Single track events will be used to determine the absolute energy calibration. The trackers are needed to determine the stored muon beam distribution, which must be known to make the electric field and pitch corrections.
The laser calibration subsystem provides the means to monitor the detector gain stability. The slow control data from the entire experiment will be gathered by a dedicated subsystem, which will monitor the performance and health of all the subsystems [76].
The design of these subsystems will be described in the following Sections.

4.2 The Calorimeter System

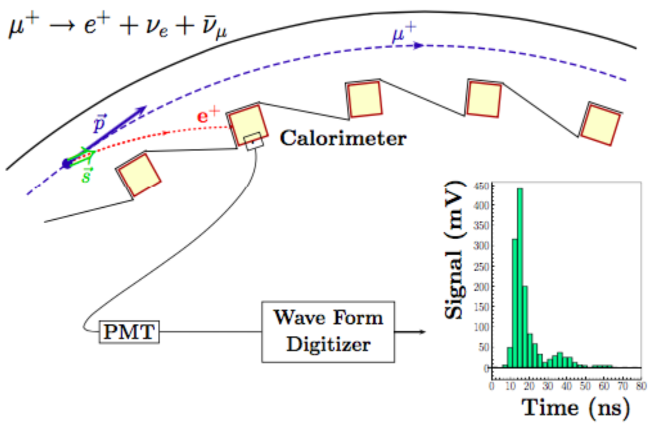

Figure 4.9: Detection process.

The primary purpose of the electromagnetic calorimeter is to measure the energy and time of arrival of the daughter positrons from stored muon decay.
After a muon decays into a positron and 2 neutrinos, the positron doesn't end up with sufficient energy to fly along the magic orbit in the ring. It curls inward where it hits a segmented lead fluoride calorimeter readout by SiPMs.
The requirements on the energy and time measurements are:

- relative energy resolution of the reconstructed positron energy summed across calorimeter segments must be better than 5 % at 2 GeV [84]: the purpose of the energy measurement is just to select events;
- timing resolution of the hit time extracted from the fit of the SiPM current pulse must be better than 100 ps for positrons with kinetic energy greater than 100 MeV in any combination of temporal and spatial pileups [76];

- the calorimeter must be able to resolve two showers by temporal or spatial separation. It must provide 100 % efficiency in the discrimination of two showers with time separations greater than 5 ns. Showers that occur closer in time than 5 ns must be further resolved spatially in more than 66 % of occurrences [76];
- the gain (G) stability requires a maximally allowed gain change of $\frac{\delta G}{G} < 0.1\,\%$ within a 200 μs time period in a fill. The long term gain stability (intervals of multiple seconds) is more relaxed and must be $\frac{\delta G}{G} < 1\,\%$. To verify the overall gain stability, each of the 24 stations must be equipped with a calibration system that must monitor the gain continually during the muon spills with a precision of $\frac{\delta G}{G} \sim 0.04\,\%$ [76];
- efforts must be made to preserve fidelity of the Cherenkov light pulse shape through the analog and digital signal chain.

Figure 4.10: Calorimeter Prototype (SLAC).

Because pileup has been in E821 the leading systematic error source and scales with rate, a segmented and very fast calorimeter has been designed. Pileup occurs when two decay positrons strike the calorimeter at nearly the same time, and are interpreted as one decay with a larger energy than either individually. If the energy of the decay positrons exceeds E_{th} such that the event is accepted, the phase will be wrong because the two positrons that led to this fake single "high" energy event had traveled a shorter distance from their parent muons than the single high-energy positron, that they mimic, would have. That is, the time from muon decay to hit a detector is shorter on average for the low-energy positrons than the higher-energy positron. Mitigating the level of intrinsic pileup is accomplished by segmenting the calorimeter (unlike E821) and by choosing a technology that allows two-pulses to be resolved with a separation of just a few ns [81]. Several factors that influenced the technology choice are [76]:

- the absorber must be dense to minimize the Moliere radius and radiation length: a short radiation length is critical to minimize the number of positrons entering the side of the calorimeter while maintaining longitudinal shower containment;

- the intrinsic signal speed must be very fast with no residuals on either leading or trailing edge since the leading edge reports on hit time, and the quality of the trailing edge is essential for reliable pileup correction;
- the energy resolution should be good but it doesn't need to be "excellent" as it is only needed for the event selection. A resolution of $\sim 5\,\%$ at 2 GeV is considered sufficient and improves upon the E821 calorimeter system by a factor of 2.

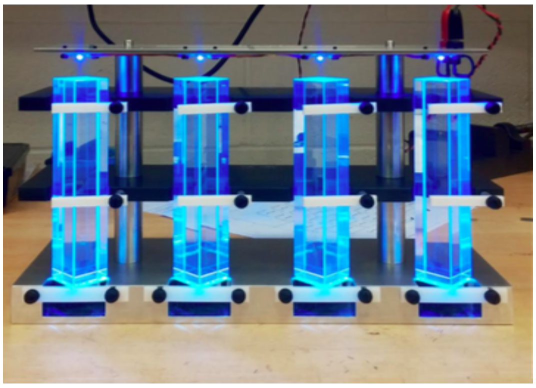

Figure 4.11: $\mathrm{Pb\,F_2}$ Cherenkov crystals [76].

The calorimeter system includes the following subsystems: absorber, photodetection, bias control, calibration, and mechanical [76]:

- Absorber: each of the 24 calorimeter stations consists of a 6×9 array of lead fluoride ($\mathrm{Pb\,F_2}$) Cherenkov crystals; the crystal is $2.5 \times 2.5 \times 14$ cm^3.
- Photodetector: each crystal is read out by a monolithic 16-channel Hamamatsu MPPC (S12642-0404PA-50)[5]; these devices have been chosen because of the compact placement, see Figure 4.12, and because of the proximity to the storage ring field, which does not allow conventional PMTs to be attached to the downstream face of the crystals.
  The current pulse output by SiPM is amplified and converted into a voltage signal in a custom made amplifier board that the SiPM is soldered to. The output stage of the amplifier board features a digitally controlled variable gain amplifier which is AC coupled to a differential pair of coaxial cables to avoid ground loops, and maximize signal to noise ratio. The recommended design does not include pole zero correction, or any other tool to shape the output pulse in order to preserve the intrinsic Cherenkov light pulse shape.
- HV bias control: reverse bias voltage applied to a SiPM is provided by a commercial HV bias power supply that maintains better than $1\,mV$ stability over the critical $700\,\mu s$ time window. The voltage output ranges from $60\,V$ to $80\,V$, and can be set digitally. Each output channel will serve about 12 SiPMs, allowing four or five individually tunable bias values per calorimeter.

[5]Multi-Pixel Photon Counter, also called Silicon Photomultipliers or SiPMs.

- Laser calibration: the calorimeter gain is calibrated and continuously monitored by a state-of-the-art high-performance laser-based distributed system. The unique system is critical to keep systematic contributions from any energy-scale instability well below the statistical precision of the measured ω_a frequency. Additionally the system will be used to initially tune and set gains for all crystals;

- Mechanical: a calorimeter housing is a moveable light-tight enclosure that provides sufficient cooling power to temperature stabilize the crystals, SiPMs, and amplifiers. The platform, which rides on a set of rails, allows easy insertion into or out of the ring in the radial direction. The absolute position of the calorimeter is of lesser importance than reproducibility of the position.

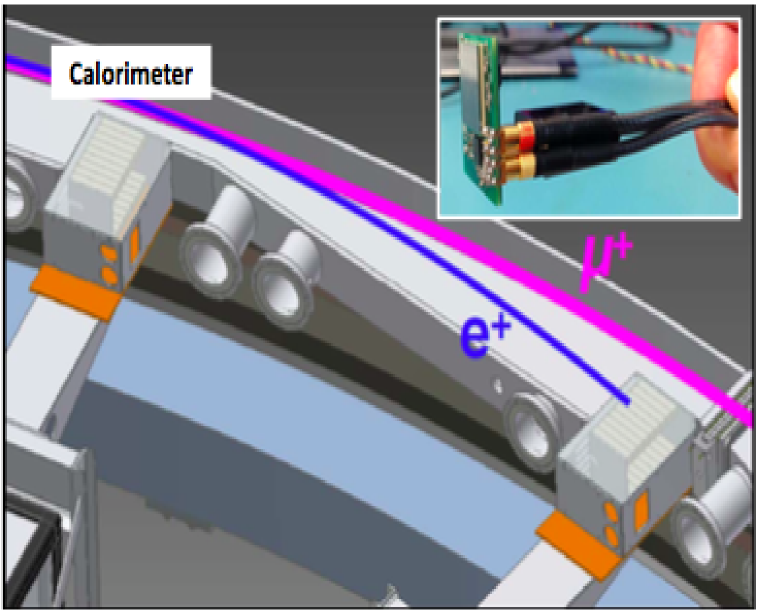

Figure 4.12: Positioning of two of the segmented calorimeter stations just downstream of the scalloped section of the vacuum chambers. The central muon orbit is sketched in, as is a nominal decay positron. The insert shows the size of the SiPM readout and its custom amplifier and pulse-shaping board [81].

Absorber Subsystem

The default material choice is lead-fluoride crystal ($\mathrm{Pb\,F_2}$) which has very high density ($7.77\,g/cm^3$). The combination of good energy resolution and a very fast Cherenkov signal response outperformed the other absorber options that had been considered.
It has very low magnetic susceptibility, a radiation length of $X_0 = 0.93$ cm, and a Moliere Radius of 1.8 cm.
Table 4.2 presents a summary of the properties of the crystals.

Crystal cross section	$2.5 \times 2.5\,cm^2$
Crystal length	$14\,cm$ $(> 15\,X_0)$
Array configuration	6 rows, 9 columns
Density of material	$7.77g/cm^3$
Magnetic susceptibility	$-58.1 \times 10^{-6}\,cm^3/mol$
Radiation length	$0.93\,cm$
Moliere radius R_M	$2.2\,cm$
Moliere R_M (Cherenkov only)	$1.8\,cm$
K $E_{threshold}$ for Cherenkov light	$102\,keV$

Table 4.2: Properties of lead-fluoride crystals [76].

GEANT- 4 simulations were used to optimize the individual crystal size and the array matrix configuration. A visualization of a typical 2 GeV positron shower is shown in Figure 4.13 [76].

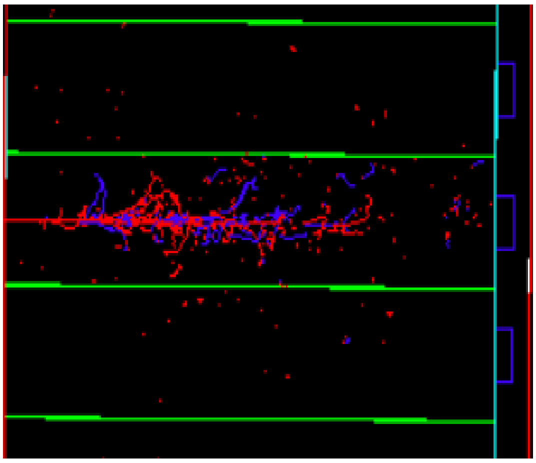

Figure 4.13: A single shower showing secondary positrons (blue) and electrons (red) in a 2.5 cm × 2.5 cm × $15X_0$ deep PbF_2 crystal, subject to a 2 GeV positron incident from the left. Photons have been removed for clarity [76].

The fast nature of the purely Cherenkov radiation aids in reducing pileup [81]. A challenge is to enable the light, which propagates dominantly via total internal reflection, to efficiently escape from PbF_2, with its high refractive index of 1.8, to the SiPM sensitive surface; indeed, the intrinsic pulse width from photon arrivals is affected noticeably by the choice of wrapping [85].

Cherenkov radiation

Cherenkov radiation arises when a charged particle in a material medium moves faster than the light in that same medium. This speed is given by:

$$\beta c = v = \frac{c}{n}$$

where n is the index of refraction and c is the speed of light in a vacuum.
A particle emitting Cherenkov radiation must therefore have a velocity $v_{part} > \frac{c}{n}$.
In such case, an electromagnetic shock wave is created, just as a faster-than-sound aircraft creates a sonic shock wave.
The coherent wavefront formed is conical in shape and is emitted at an angle

$$cos\theta = \frac{1}{\beta n}$$

with respect to the trajectory of the particle. In general, a continuos spectrum of frequencies is radiated with the photon being linearly polarized [86].
In a threshold Cherenkov counter, the total light emitted above threshold is collected. It gives a yes/no decision based on whether the particle speed is above or below threshold, $\beta_t > 1/n$. Instead, the imaging Cherenkov counters make use of the dependence of the fast particle speed from the photon emission angle [87].

Wrapping

Different wrappings are being tested in order to study the light collection efficiency of the crystals and the couplings to the photo-sensitive readout.

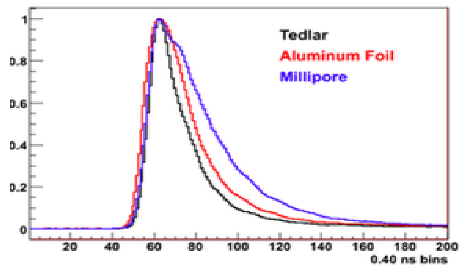

Figure 4.14: Normalized response of PbF2 crystal wrapped in absorptive black tedlar, reflective aluminum foil, and white Millipore paper. A 29-mm Photonis PMT was used to make these comparisons [76].

Tests are focused on two extremes, namely an all-black Tedlar absorptive wrapping, and a diffuse reflective white Millipore paper wrapping which acts as a Lambertian (diffusive) mirror. The black wrapping largely transmits only the direct Cherenkov light cone, while the white wrapping allows light to bounce multiple times within the crystals, eventually leading to a higher overall photon yield. Both wrappings have advantages.
For the shortest pulse occupancy time, the black wrapping excels.
For the greatest light yield, the white wrapping is better.
Shorter-duration pulses improve pileup rejection; higher light yield improves energy resolution [76].
A sketch of the representative features of light propagation in the crystal is shown in Figure 4.15. Near the entrance, the Cherenkov cone produces photons at 57° with respect to the crystal axis which is aligned with the beam direction. As the shower develops, the average angle loses its original coherence, becoming nearly isotropic closer to the end of

the crystal.
Light bounces off of the faceted crystal surface owing to internal reflection for angles less than the critical angle $\theta_c = 90° - 57° = 33°$. For larger angles, it passes into a thin layer of air and then hits the wrapping. The black wrapping is assumed to be totally absorptive, while the white wrapping is diffusive, re-emitting the light at a new angle, that might again be captured in the crystal. The indexes of refraction of the crystal (1.8), optical gel (1.62), protective epoxy resin (1.55), and SiPM active surface (~ 3) are shown.
Only photons passing through this sequence can convert to photoelectrons [85].

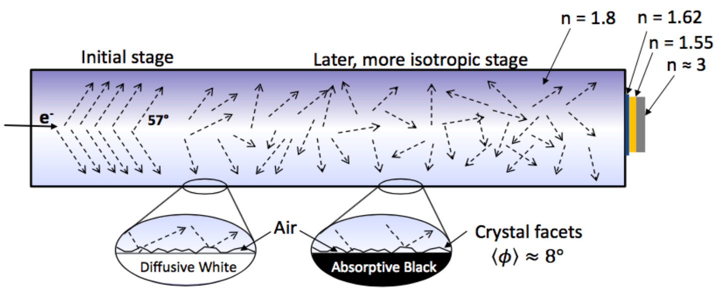

Figure 4.15: Light propagation in the crystal [85].

Photodetection Subsystem-SiPM

Silicon photomultipliers (SiPMs) read out the crystals.

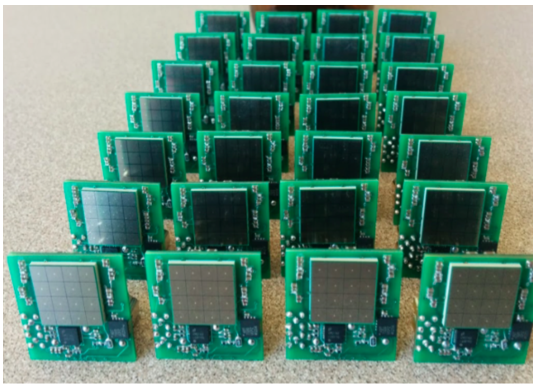

Figure 4.16: Set of SiPMs + Electronics.

While challenging and relatively new devices, they are increasingly preferred over traditional PMTs in many Nuclear and Particle Physics applications.
They work as pixelated Geiger-mode counters. The default SiPM that it's going to be considered has $57,600$ -50 μm-pitch pixels on a 1.2 $\times$ 1.2 cm^2 device.
When a photon strikes a pixel, it can cause an avalanche that is summed together with the other struck pixels in a linear fashion to produce the overall response. Quenching resistors are intrinsic to the device to arrest the avalanche and allow the device to recover. The recovery time constant of a fired pixel is typically of the order of tens of ns. Those pixels that are not struck, meanwhile, remain ready for a next pulse.

The pixel recovery time is very much dependent on the SiPM fabrication properties. For good near-linear operation, the number of pixels must exceed greatly the highest photon count that is expected to strike the device, allowing a high photo-detection efficiency [84]. The selection of SiPMs over PMTs is pragmatic. SiPMs can be placed inside the storage ring fringe field, thus avoiding the awkward, long lightguides that would be needed for remote PMTs.
They will not perturb the storage ring field, and they can be mounted directly on the rear face of the PbF_2 crystals. Large-area SiPM arrays are cheaper than same-size PMTs, their cost is falling, and their performance characteristics continue to improve.
One of the challenges of using SiPMs is their particular sensitivity to temperatures.
The calorimeter design is prepared to handle the temperature dependance currently observed. While short-term shifts are unexpected, the overall SiPM environment must be maintained at a fairly constant temperature in order to simplify the global calibration of gain during the running period.
The response of a SiPM is also quite sensitive to the bias voltage stability above Geiger-mode breakdown threshold [76].

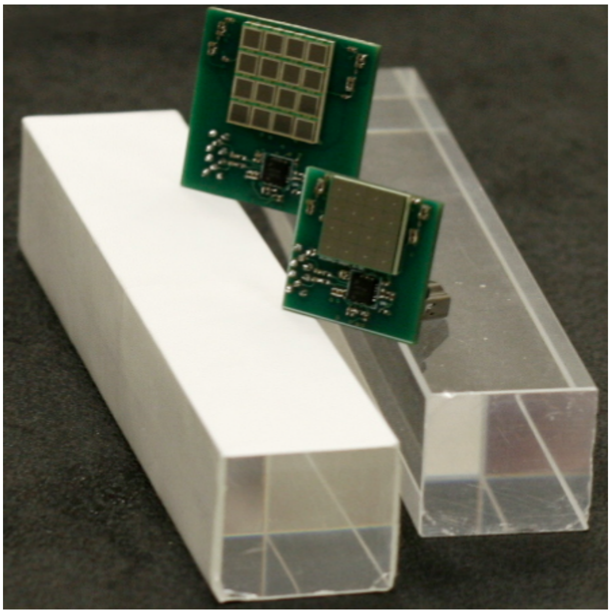

Figure 4.17: Sample $25 \times 25 \times 140$ mm^3 PbF_2 crystals (bare and wrapped in Millipore paper) are pictured together with a 16-channel monolithic Hamamatsu SiPM mounted to our transimpedance amplifier board (front). Behind it, one of alternative SiPM designs manually assembled from 16 individual SiPMs is shown. A Millipore wrapped crystal read out by a monolithic 16-channel SiPM is the core of FNAL recommended design [76].

Bias Voltage System for SiPMs

The requirements that drove the baseline design are presented below.
The SiPM Bias System must supply a bias voltage for each SiPM that should be stabilized at the mV level, particularly over the critical $700\,\mu s$ time window.
At the projected operating voltage, the gain shift per millivolt is $0.12\,\%$, which equates to a

0.05 ppm shift in ω_a if it were left uncorrected. The requirement to maintain mV stability or better is selected such that any necessary correction from bias voltage deviation is not large compared to the overall systematic error budget. To meet this requirement, the control loop for each channel must have a voltage resolution of at least 1 mV.
Each SiPM has a preferred working point bias, so the system must allow each channel to be set to an individual bias voltage. The expected operating voltage range of the SiPMs is a few volts around a central bias voltage of approximately 70 V. There will be 24 individual SiPM Bias Systems, one for each calorimeter station, plus one additional spare [76].

4.3 Tracking Detectors

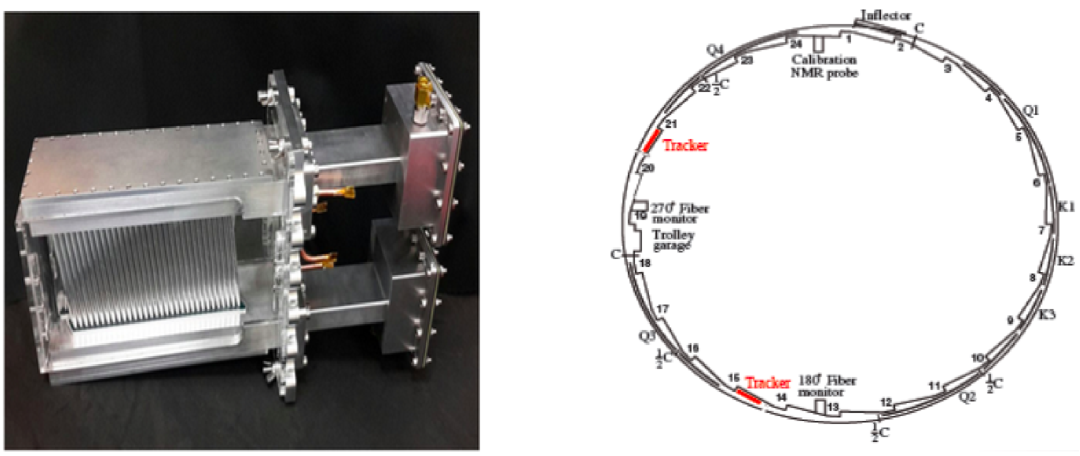

Figure 4.18: A tracking module and its position.

The primary goal of the tracking detectors is to measure the muon beam profile at multiple locations around the ring as a function of time throughout the muon fill [76]. This auxiliary system is required for the following reasons:

- momentum spread and betatron motion of the beam lead to ppm level corrections to the muon precession frequency associated with the fraction of muons that differ from the magic momentum and the fraction of time muons that are not perpendicular to the storage ring field;
- betatron motion of the beam causes acceptance changes in the calorimeters that must be included in the fitting functions used to extract the precession frequency;
- the muon spatial distribution must be convoluted with the measured magnetic field map in the storage region to determine the effective field seen by the muon beam.

The secondary goal of the tracking detectors involves understanding systematic uncertainties associated with the muon precession frequency measurement derived from calorimeter data. In particular, the tracking system will isolate time windows that have multiple

positrons hitting the calorimeter within a short time period and will provide an independent measurement of the momentum of the incident particle. This will allow an independent validation of techniques used to determine systematic uncertainties associated with calorimeter pileup, calorimeter gain, and muon loss based solely on calorimeter data.
The tertiary goal of the tracking detectors is to determine if there is any tilt in the muon precession plane away from the vertical orientation. This would be indicative of a radial or longitudinal component of the storage ring magnetic filed or a permanent electric dipole moment (EDM) of the muon. Any of these effects directly biases the precession frequency measurement. A tilt in the precession plane leads to an up-down asymmetry in the positron angle that can only be measured with the tracking detectors [76].

4.3.1 Tracker design

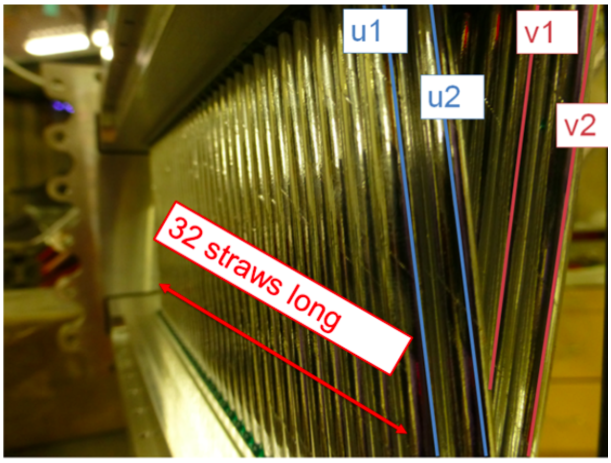

Figure 4.19: The straw tracker: overview.

The tracker design is an array of straw tubes with alternating planes oriented 7.5° from the vertical direction. The DC nature of the beam requires a tracker with multiple planes spread out over a lever arm as long as possible. The required number of planes, along with the need to minimize multiple scattering, lead to the choice of a gas based detector. The requirement to place the detectors in the vacuum leads to the choice of straws since the circular geometry can hold the differential pressure with minimal wall thickness.
Straw or tube chambers are basically proportional chambers constructed with a single anode wire centered in an aluminized plastic tube forming the grounded cathode; when a charged particle passes through the tube, it ionizes the gas generating a signal for a particle "hit" [78].
The advantages of a straw chamber when compared to multiwire chambers are [88]:

- the straw chamber is inexpensive, robust and relatively simple to construct;
- the damage and possible down time caused by wire breakage is minimal since the broken wire is isolated in the tube cell and will only need to be disconnected;

- the effect of signal cross talk are minimized as the straw cathode provides a complete ground shield between nearby wires;
- the problems of electrostatic alignment distortions are minimal when the anode is kept reasonably centered in the straw.

The main disadvantage is the amount of material the straw introduces into the chamber. This causes more multiple scattering and reduces the momentum resolution.
In order to minimize multiple scattering of muons and positrons, g-2 muon storage volume, which lies within the 1.45 T magnetic field, is evacuated.

Gas mixture choice

The choice of the drift gas that has to fill the detector, between the wire and the walls of the straw, is guided by gain, efficiency, convenience and economic reasons. The typical mixture is composed by a noble gas and a quencher. Avalanche multiplication occurs in noble gases at much lower fields than in complex molecules: this is a consequence of the many non-ionizing energy dissipation modes available in polyatomic molecules. Therefore, convenience of operation suggests the use of a noble gas as the main component; addition of other components will of course slightly increase the threshold voltage.
The choice within the family of noble gases is then dictated by a high specific ionization; disregarding for economic reasons the expensive Xenon or Krypton, the choice naturally falls on Argon.
During the avalanche process, excited and ionized atoms are formed.
The excited noble gases can return to the ground state only through a radiative process, and the minimum energy of the emitted photon (11.6 eV for Argon) is well above the ionization potential of any metal constituting the cathode (7.7 eV for Copper). Photo-electrons can therefore be extracted from the cathode, and initiate a new avalanche very soon after the primary.
Argon ions, on the other hand, migrate to the cathode and are there neutralized extracting an electron; the balance of energy is either radiated as a photon, or by secondary emission, i.e. extraction of another electron from the metal surface. Both processes result in a delayed spurious avalanche: even for moderate gains, the probability of the processes discussed is high enough to induce a permanent regime of discharge.
The large amount of non-radiative excited states (rotational and vibrational) allows the absorption of photons in a wide energy range: for methane, for example, absorption is very efficient in the range 7.9 to 14.5 eV, which covers the range of energy of photons emitted by argon. This is a common property of most organic compounds in the hydrocarbon and alcohol families, and of several inorganic compounds like freons, CO2, BF, and others. The molecules dissipate the excess energy either by elastic collisions, or by dissociation into simpler radicals [89].

Chapter 5

The *g-2* Laser Calibration System

It is estimated that the detector response must be calibrated with relative accuracy at sub-per mil level to achieve E989 experiment's goal: keeping systematics contributions due to gain fluctuations at the sub-per mil level on the beam fill scale ($0 - 700\,\mu s$).
Over the longer data collection period the goal is to keep systematics contributions due to gain fluctuations at the sub-percent level [90].
The level of accuracy required is a challenge for the design of the calibration system because it is at least one order of magnitude higher than that of all other existing, or adopted in the past, calibration systems for calorimetry in Particle Physics [80].
For instance, the ATLAS calibration system calibrates at a 10^{-3} accuracy level.

5.1 The calibration procedure

A the end of data taking, the collaboration aims at obtaining a single plot integrating all the required statistics and appearing as the one in Figure 3.6. The main purpose of the calibration system is to obtain calibration constants to be applied during analysis.
Two time scales, related to gain fluctuations, are to be monitored:

- long term fluctuations (hours/days): this kind of fluctuation does not depend on the beam but rather on local factors such as drift day/night, temperature, bias voltage variations; the calibration can be performed offline: it has to be checked when the system goes beyond a threshold value upon which measurement perturbations are evident;

- short term fluctuations ($0 - 700\,\mu$s: time of a fill): this kind of fluctuation is not related to environmental factors but rather to beam features such as muon rate, incoming electrons, i.e. charge, which can cause over/under voltages; the calibration has to be performed online, using laser pulses during the fill[1].

[1]It is essential to have enough points (~ 140) for fill.

Calibration system: statistical goal

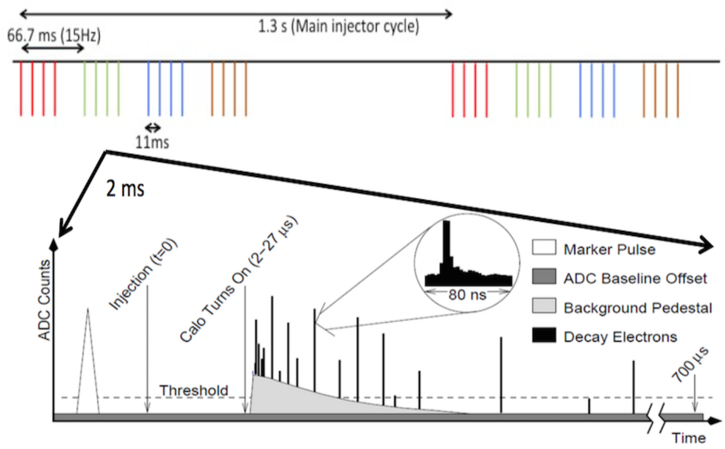

Figure 5.1: Time profile of a fill.

The accelerator machine produces 2 signals, one "Begin of Fill" (BOF) signal and one "End of Fill" (EOF) signal; they define a 700 μs period, in other words the period when decay positrons hit calorimeters; this time span is followed by a 10 ms period without beam and with no signal to be acquired. The laser is going to send calibration pulses in a $\sim$ 11 ms period (10 ms + 700 μs).
The statistical goal is to reach 0.04 % statistical uncertainty per time interval within a spill (point), which means 2000 events/point.
The laser repetition rate has to be chosen in order not to perturb the signal by overlapping with positrons; furthermore the laser pulse duration should be as short as possible not to violate the assumption that every fill in the calibration run is identical.
Let's assume 7 points per fill (1 every 100 μs, 10 kHz laser repetition rate).
By moving the offset by 5 μs after a fill, 20 fills are necessary to have a single event calibration cycle (i.e. one point every 5 μs).
Calibration runs lasting $60'$ with $\sim$ 10 kHz laser frequency lead to a sampling of G(t), which is the gain of the system whose stability has to be monitored, in 140 points between 0 and 700 μs.

5.2 Calibration system guidelines

Almost 1300 channels must be calibrated during data taking; the proposed solution is based on the method of sending simultaneous light calibration pulses onto the readout photo-detector through the active sections (crystals) of the calorimeters.
Light pulses must be stable in intensity and timing to correct for systematic effects due to drifts in the response of the crystal readout devices. A suitable photo-detector system must be included in the calibration architecture to monitor any fluctuation in time of the light source intensity and beam pointing as well as any fluctuation of the transmitted light along the optical path of the light distribution system, which could occur because of mechanical vibrations or optics aging.

Some guidelines are defined to select the light source(s) and to design the geometry of the light distribution and monitoring; the following criteria are adopted to select the light source type [76]:

- light wavelength must be in the spectral range accepted by the detector and determined by the convolution of the spectral density of the Cherenkov signal produced by positrons in PbF_2 crystals with the spectral transmission of the crystals (See Figure 5.2), and with the spectral Quantum Efficiency (Q.E.) of the photo-detector; Q.E. is peaked around 420 nm for SiPMs, as shown in Figure 5.3; the chosen laser wavelength is 405 nm;

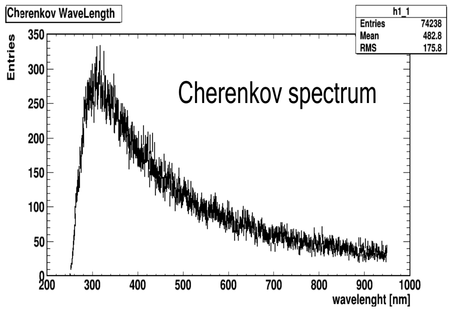

Figure 5.2: Wavelength distribution for Cherenkov photons produced by 2 GeV e^- on a PbF_2 crystal (GEANT 4 simulation).

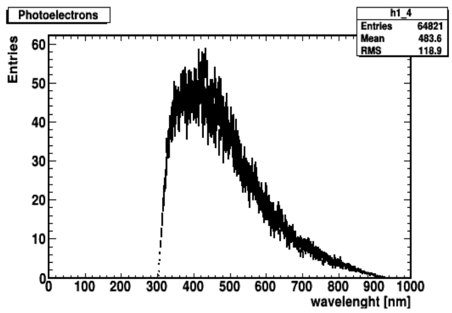

Figure 5.3: Wavelength distribution for the Cherenkov photons that, once transmitted through a PbF_2 crystal, manage to produce photoelectrons (GEANT 4 simulation).

- the luminous energy of the calibration pulses must be in the range of the positron energy deposited in the crystals, typically 1-2 GeV; if we take, for the number of laser photons per pulse the value N_γ of Cherenkov photons integrated by a PMT, the laser equivalent energy pulse on each tower of a calorimeter station is:

$$E^{crystal}_{pulse} = N_\gamma \times E_\gamma = N_\gamma \times h\frac{c}{\lambda} = 2\cdot 10^4 \times 6.6\cdot 10^{-34}[J\cdot s]\times \frac{3\cdot 10^8[m\cdot s^{-1}]}{400\cdot 10^{-9}[m]} = 0.01\,pJ$$

The numbers quoted above are merely indicative of the order of magnitude; they are derived by assuming that the readout of each crystal will produce about 2 photo-electrons per MeV with 50 % P.D.E.[2] for SiPMs and with 40 % coverage of the crystal readout face. If the simultaneous excitation of all calorimeter readout channels[3] (1296) is considered, the equivalent energy value becomes about 0.013 nJ ($E^{crystal}_{pulse} \times 1296$). Finally, taking into account the whole distribution system,

$$E^{TOT}_{pulse} = \frac{24 \times 54 \times E^{crystal}_{pulse}}{T} = \frac{24 \times 54 \times 0.01pJ}{T} = \frac{13pJ}{T} \tag{5.1}$$

The "light transmission factor" T includes light loss along the optical path: filters, diffusive elements, fiber coupling, light routing to calorimeter and depends on the adopted solution;

- the pulse shape and time width must be suitable to infer on the readout capability in pile-up event discrimination; pulse rise/trailing time must be of the order of some hundred of ps, the total pulse width should not exceed 1 ns;
- the pulse repetition rate must be of the order of 10 kHz; this value will be tuned to obtain the best compromise between the need of having enough calibration statistics in the time interval (some tens of μs after the muon injection in the ring) when the maximum rate is achieved in the readout devices, the need to avoid saturation of the DAQ bandwidth and laser-signal overlapping.

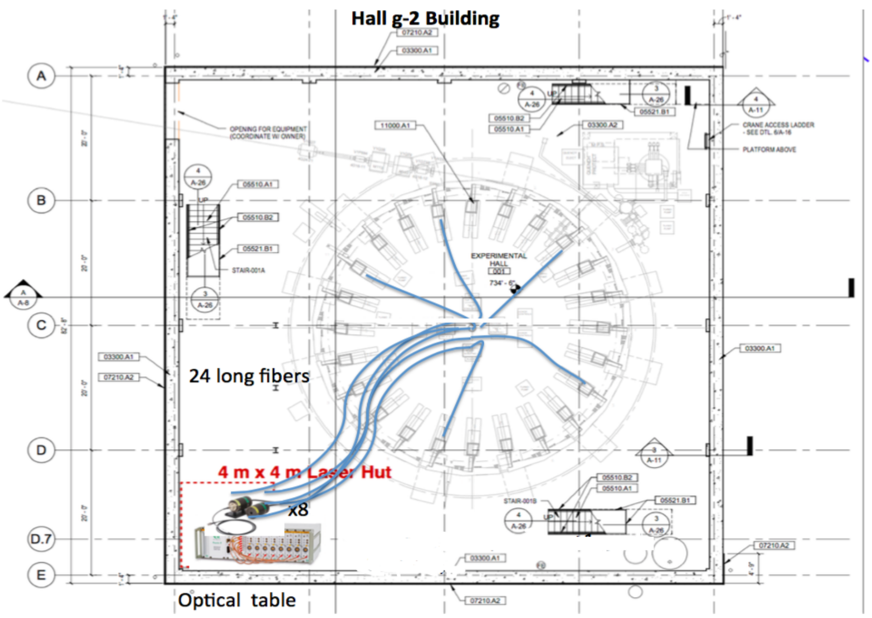

Figure 5.4: *g*-2 experimental hall.

Guidelines for designing the light distribution chain are listed below [76]:

[2]P.D.E. stands for Particle Detection Efficiency.

[3]The number of channels (1296) is determined by multiplying the number of calorimeter stations (24) by the number of crystals in every station (9 × 6).

- high sensitivity monitors of the transmitted light at the end-point of each individual section of the distribution chain must be used to ensure online control of the system stability and to have information to apply feed-back corrections to the source operation parameters, if needed;

- the optical path must be minimized in order to limit the light loss due to self-absorption in the optical fibers; the number of cascade distribution points must be also minimized to reduce the unavoidable light loss in the couplers between different sections;

- the laser source and its control electronics should be located outside the muon ring in order to avoid electromagnetic perturbations of the local field induced by the current flow used to excite the laser;

- optical fiber selection: silica fibers (20 dB/km attenuation at 400 nm) are the best solution for long path light transmission and in terms of robustness against solarization or other aging affects due to large values of transmitted light intensity.
  For the shorter fiber bundles, where the transmitted intensity is at least one order of magnitude lower, also PMMA clear fibers (200 dB/km attenuation at 400 nm) can be considered to save money.

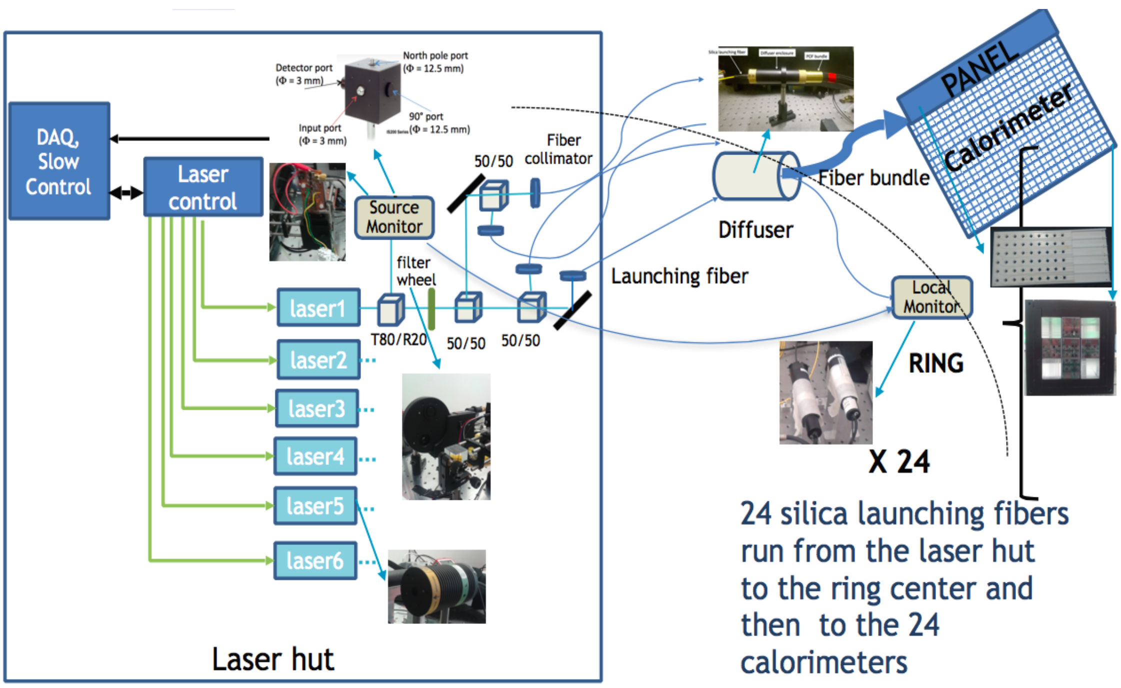

Figure 5.5: Preliminary scheme; in the final version the Local Monitor is going to be in the laser hut together with the Source Monitor.

A scheme fulfilling all the requirements set by the guidelines listed above is shown in Figure 5.5; light generated by a laser source is fed into a primary distribution device located outside the muon ring; quartz fibers (25 m long, one per calorimeter station plus

spares for monitoring purposes) route the light to secondary distribution devices located near the calorimeter stations, each distributor serving one station. A small fraction of the light exiting the source and the light distributors is routed to monitors whose analog signal is returned to the DAQ system for online checking of the system stability. Interface with DAQ is also required for slow control signal recording, and communication with the timing signal controls is used to trigger the electronics of the laser driver.
The crucial elements of this system are the light source and the distribution system, that shares the light to the calorimeters with sufficient intensity and sufficient homogeneity among them [80].

Laser source

The light source should be in the same spectral range accepted by the photodetectors and has to be powerful enough to ensure a sufficient amount of light for each calorimeter station considering losses due to the distribution chain. Among many different types of pulsed lasers commercially available, pulsed diode lasers in the blue seem to best address all the criteria listed above [90]. In the final configuration the laser source is composed by 6 lasers LDH-P- C-405M from PicoQuant driven by a single PDL 828 Sepia II 8 channel multi-laser driver: the redundancy granted by this kind of solution would have the advantage that, in case of laser failure, no calibration stop will occur during data acquisition; moreover, lower power lasers are, in general, more stable.
The laser source fully agrees to all the guidelines defined by the experiment:

Wavelenght	405 ± 10 nm
Pulse FWHM	700 ps
Average Power (at 40 MHz)	28 mW
Power stability	1 % RMS, 3 % peak to peak (12 h)
Measured light output	1000 pJ/pulse at 10 kHz

Table 5.1: Properties of the laser source.

Distribution chain

The task of the distribution chain is to divide and carry the light from the laser source to the different calorimeter stations placed around the ring, preserving as much as possible uniformity and intensity of the laser light source.
The first step consists in collecting the light of the laser using optical fibers. The attenuation loss of the fibers should be minimized because the laser could be $\sim$ 25 m far away from a single calorimeter station. For this reason the fibers used are quartz fibers with an attenuation of 20 dB/km at 400 nm. Each laser is splitted in four and coupled to quartz fibers. To connect all the equipment with the engineered diffuser, which is the item placed near the calorimeter, a 25 m long launching fiber (quartz fiber) is used. The diffuser is then coupled, through a 3 m fiber bundle, to the front panel placed in front of the crystals. One of the major efforts of the distribution chain is related to the design and the construction of the front panel, necessary to couple the fibers coming from the diffuser to the calorimeter. This front panel has 9 holes. Each hole houses a 5×5 $45°$ prism glued

to the panel. Each fiber comes from one side and reaches each prism following guiding grooves starting on one side. This design is constrained by the mechanical design of the calorimeter box which will be used during the final experiment where the only possible access to the calorimeter is an aperture on the left side of the box 2 cm large: a device which can deflect the light coming from 54 fibers to 54 crystals in 2 cm of space has to be created.

Laser Calibration Stability

The most important feature of the calibration system is time stability. In fact is requested a stability of the order of 10^{-4} over 2 hours.
To ensure that this level of stability is maintained during data taking a monitoring procedure has to be included in this calibration system. The monitoring system is composed of two parts. The Source Monitor checks all the possible fluctuations of the laser sources. The number of Source Monitors is the same number of the laser sources. The Local Monitor checks the stability just before the injection of the calorimeters. Temperature stability is extremely important: the gain of PMTs is significantly sensitive to temperature variations of less than 0.1 °C. These temperatures will be monitored but it is obviously important to maintain temperature stability and uniformity in the experimental hall as much as possible.

5.3 Monitoring System

5.3.1 The Source Monitor

The light sent to the channels is monitored close to the light source, pulsed laser in this case, with the so called Source Monitor where absolute value of the laser power sent to the distribution system is being measured.
The following expedients will be used to optimize the monitor stability [76]:

- employ zero gain PIN diodes which are much more stable than SiPMs to variations in bias and temperature; they will be exposed to much higher light levels to minimize photostatistical fluctuations;
- use a redundant system, with three photodetectors for each monitor;
- minimize the "pointing fluctuations" by incorporating diffusion and mixing elements;
- incorporate a radioactive source for absolute calibration.

Primary distribution points are necessary to split the light coming from the laser.
The light distribution points have to be tested in order to understand how stable they are and how the outgoing light is; different configurations being studied are: an integrating sphere (default solution) shown in Figure 5.6 and a combination of an engineered diffuser and a reflective mixing chamber, shown in Figure 5.7. In the planned design, the laser pulses should be sent into one or more integrating spheres and then coupled into bundles

of optical fibers. Each fiber will finally convey the light pulses into the crystals and SiPMs to be calibrated.

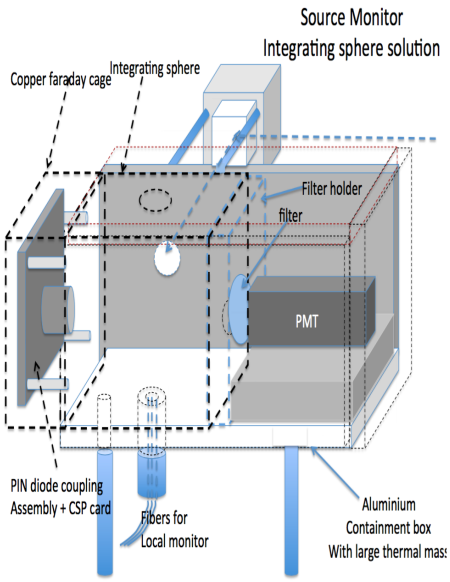

Figure 5.6: Source monitor (developed by the Udine group).

Integrating spheres with diffusely reflective white walls, also known as Ulbricht spheres, have been used for more than a century for the characterization of light sources, detectors, and for other photometric studies.
An integrating sphere is used to spatially integrate a radiant flux that can either be introduced into it by some input port or directly produced inside the sphere by a source. In either case, the light reflects diffusively several times inside the sphere so that, on some output port, the radiant flux can be considered uniform and isotropic [90].
The shape of the output signal is determined by convolving the input signal with the time response of the integrating sphere. The time response is of the exponential form $e^{-t/\tau}$ and the time constant τ is given by:

$$\tau = -\frac{2}{3}\frac{D}{c}\frac{1}{ln\,\rho_{eff}}$$

where ρ_{eff} is the average wall reflectance, c is the velocity of light and D is the diameter of the integrating sphere [91].
Tests demonstrated a very high degree of uniformity, up to 99.3 % for a 1 mm diameter fiber connected to one sphere port at the price of a rather large intensity loss (10^{-4}).
The alternative solution (diffuser+mixing chamber) has the following features: it is not as much uniform as the sphere is, even if the uniformity is acceptable, but the transmission factor is 15/20 times higher than the one of the sphere.
A comparison of the performance of the two solutions was done during the Test Beam performed in Frascati. Details will follow in the next chapter.

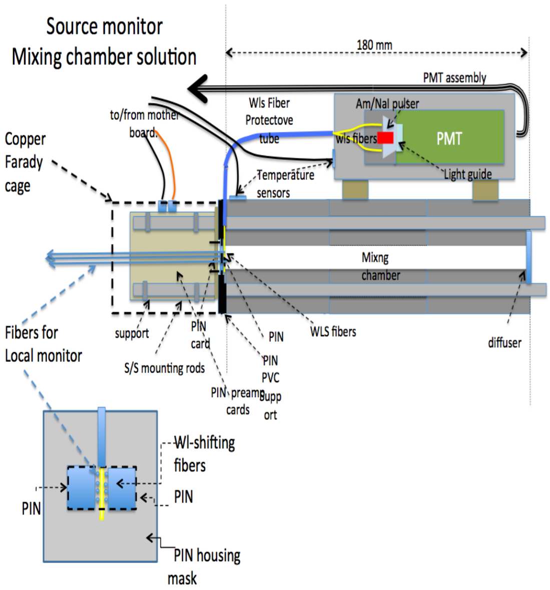

Figure 5.7: Source monitor (developed by the Udine group).

The source output is monitored by a system composed by two PIN diodes, a PMT and uses a small plate of ^{241}Am [80].

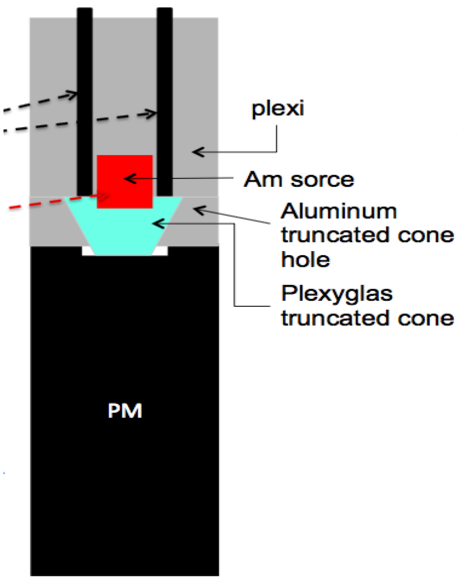

Figure 5.8: Source monitor (developed by the Udine group).

The PMT simultaneously views:

- the laser light pulses transmitted from the sphere to the photocathode by wavelength-shifting fibers;

- light pulses which are emitted by a weak Am source[4], deposited on an NaI crystal, enclosed in an aluminium cylinder with a quartz window situated close to the PMT photocathode.

The signal from the Am source serves as an absolute reference in lieu of the relatively poor stability (e.g. strong dependence on HV) of PMTs.
Tests taking place in Udine showed that:

- the PIN diode response is stable w.r.t. temperature to better than 0.2 % per °C. Higher statistics measurements are needed to establish an eventual temperature-dependence of the PIN diode response;
- The PM gain is very dependent ($\sim 3\,\%$ per °C) on temperature. Accurate temperature measurements are needed to establish this temperature dependence;
- The Am signal can be used to correct for temperature-dependence and the fluctuations but $\sim$ 30000 events ($\sim$ 2 hour) are needed for accuracy at the level of 0.4 %.

5.3.2 The Local Monitor

In order to closely monitor the light that illuminates each of the channels and diagnosing the source of eventual instabilities or faults in the distribution system, a so called Local Monitor system has been devised. The Local Monitor has to be different from the Source Monitor because of different position and light characteristics [80]. The proposed system consists of custom made detector assembly (LMA) based on photomultiplier tubes (Photonics PMTs) placed in the laser hut. In order to guarantee the performance of the LMA it has to be illuminated by a stable source with known power.
A small amount of light ($\sim$ 10 pJ) is taken from the main distribution beam immediately before entering the outgoing fiber[5]; the second signal comes directly[6] from the bundle which goes to the calorimeter.

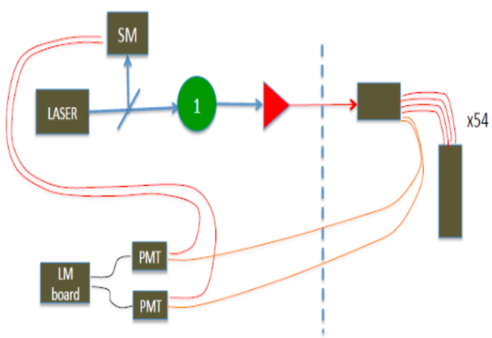

Figure 5.9: LM PMTs are directly supplied by the Source Monitor.

[4]The chosen radiative Americium source emits α particles at a rate of $\sim$ 5 Hz.
[5]It is a fiber coming from the SM which furnishes the source reference signal.
[6]Through a PMMA fiber.

The time delay acquired during the light pulse roundtrip in the distribution and LM system should separate the calibration and the monitored signal by a time interval sufficient ($\sim$ 250 ns) to resolve two light pulses. The advantage of such setup is that the PMT gain can be considered constant during this timescale and that the two pulses can be directly compared. Also absolute calibration can be provided by referencing these signals to the Source Monitor of each laser.
An extensive study of the components of the distribution and LM system has been performed and the most promising solution has been chosen for each of the critical points. Primary distribution is based on a series of beamsplitters which guarantee long term stability better than 1 %. With the proposed scheme it is possible to find fluctuations in the distribution by observing the calibration peaks in the LMA. Care must be taken to stabilize the fiber which goes to the PMTs against temperature or mechanical/optical variations.

5.3.3 Monitoring Electronics

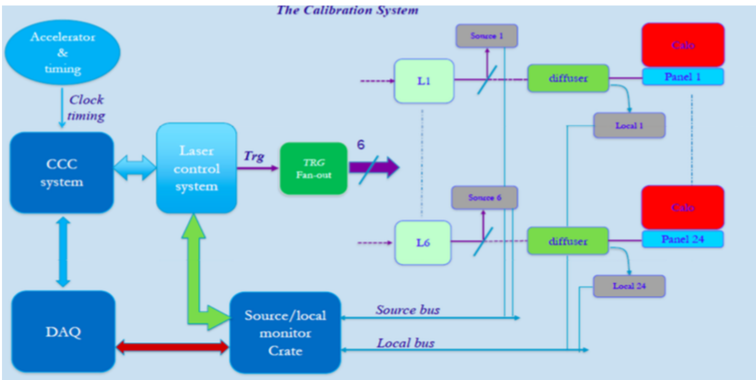

Figure 5.10: Laser control system

The Monitoring Board (MB) is the electronics which will be used to monitor calibration signals coming from the lasers. It consists of an electronic device designed for the acquisition of calibration pulses provided by the laser source; as output signals it provides a digital pattern produced by the Analog to Digital Converter (ADC) that has to be send to the Data Acquisition System (DAQ) and an analog signal for the Wave Form Digitizer (WFD). The Monitoring Board acquires signals upstream (Source Monitor) and downstream (Local Monitor) from the distribution system in order to monitor and guarantee the stability of the calibration signal and do something, if necessary, to stabilize sensors and readout electronics. It provides a pattern for each pulse composed by:

- a start;
- an event number (BOF/EOF);
- an event absolute time (BOF/EOF);
- temperature, High Voltage, SiPM bias voltage and PMT HV, 5 nominal values of the test pulse for each channel;

- $10 \times$ ADCval: 10 signal samples, time related to BOF, iCH (to identify the channel), iSignal (to codify the kind of signal);
- Stop.

Chapter 6

Test of the g-2 calibration system with an electron beam

This section describes the tests of a calorimeter prototype performed in Frascati at the Beam Test Facility (BTF) from 29^{th} February to 6^{th} March 2016 to which I took part actively taking care in particular of the Local Monitor system.

The Beam Test Facility and DaΦne accelerator

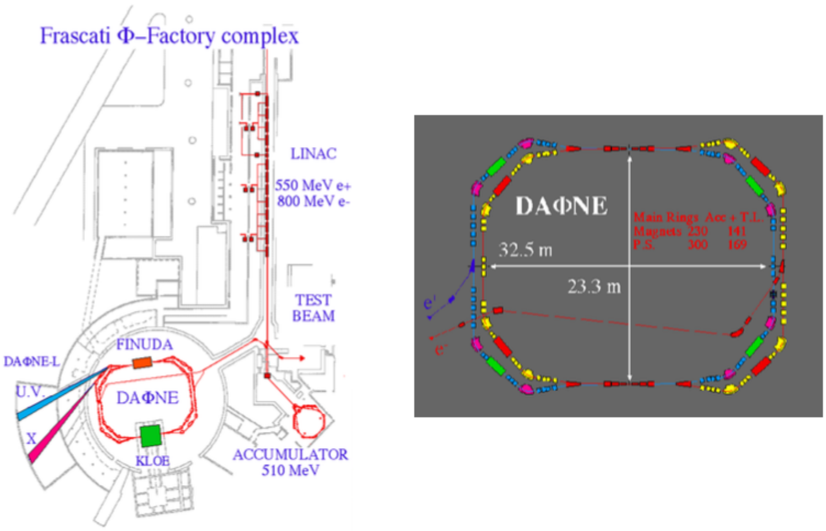

Figure 6.1: Left: The DAΦNE complex. Right: Schematic layout of the two DAΦNE Main Rings.

The Beam Test Facility (BTF) is a beam line optimized for the production of a pre-determined number of electrons or positrons, in a wide range of energies (up to 800 MeV) and multiplicity. The facility is particularly suitable for particle detector testing purposes, such as energy calibration and efficiency measurements, in single electron mode [92].
The BTF is part of the DAΦNE accelerator complex, consisting of:

- a double ring electron-positron collider: this is a “conventional” storage ring, where a single bunch of electrons and a single one of positrons circulate in opposite directions, crossing in a low-beta interaction point and being separated at the opposite point in the ring by means of electrostatic fields [93];

- a high current linear accelerator (LINAC): it delivers electrons with energy up to 800 MeV, with a typical current of 500 mA/pulse, or positrons with energy up to 550 MeV, with a typical current of 100 mA/pulse and a resolution of 1 %; the pulse duration can be adjusted in the range $1 \div 20$ ns with a maximum repetition rate of 50 Hz [92];
- an intermediate damping ring (Accumulator);
- a system of 180 m transfer lines connecting the four machines: the initial part of the transfer line delivers the LINAC beam to a copper converter with selectable radiation lengths. The outgoing beam acquires a broaden energy spectrum down to few tens of MeV; the population per energy bin is determined mostly by the bremsstrahlung process. The remaining transfer line is composed of different dipoles, quadrupoles, correctors and couples of vertical and horizontal scrapers. These elements act formerly as energy, transverse parameters and multiplicity selectors.

The end of the transfer line is in a 100 m^2 experimental hall, where detector calibrations and tests can be carried out. The facility, initially optimized to produce single electron in the $25 - 750$ MeV energy range, can now provide beam with different particles in a wider range of intensity, i.e. up to 10^{10} electrons/pulse [92].
During the test for the g-2 experiment, most of the runs were taken with an average intensity of about one electron per pulse. Higher intensities, up to three electron per pulse, were also used. The electron beam arrived in the test area with a transverse dimension of about 250 μm and a mean position stable in time.

Test Beam goals

The facility was used to test a small calorimeter prototype, of 5 real crystals in different configurations.
The purpose of the Test Beam (TB) was multifold:

- calibration of the laser intensity using a 450 MeV e^- beam to obtain the equivalent luminous energy of the laser;
- test of the calibration system with the full-line (from the control board to the calorimeter) including the laser-driving and electronics board in an environment closer to the one of the experiment;
- test of the SiPMs and their bias voltage configuration;
- test the energy degradation of the physics signal due to the presence of the front panel.

The e^- beam was first fired at the center of the central crystal in the 3×3 array; then, moving the BTF table, it was possible to illuminate other PbF_2 crystals in order to study the shower leakage together with the superposition of laser signal with physical signal.

6.1 Experimental Apparatus

6.1.1 Detector and SiPMs

The calorimeter was positioned on a movable table in order to match the position of the electron beam. It consisted of a small scale prototype of the calorimeters that will be used for the actual muon g-2 experiment: it was composed by an array of 3 × 3 crystals arranged as shown in Figure 6.2: 5 PbF_2 crystals were arranged in a cross-like configuration while 4 mock crystals in Plexigas were placed at the corners. The sensitive elements were $2.5 \times 2.5 \times 14$ cm^3 high-quality PbF_2 crystals. This small calorimeter was housed in a light tight box which permitted also the right placement of a 3 × 3 front panel prototype.

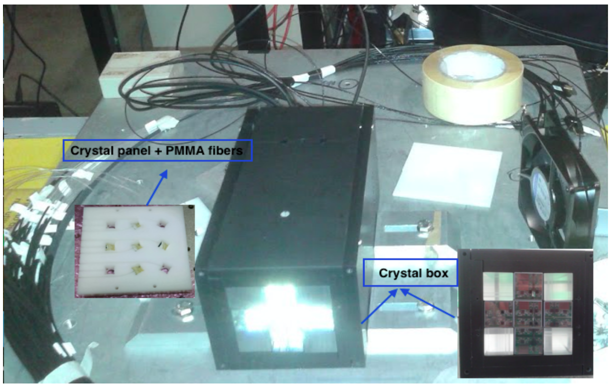

Figure 6.2: Calorimeter setup at the Test Beam.

Detector housing held photodetectors against the calorimeter back face: a 16-channel Hamamatsu SiPM was glued to the rear face of each crystal. The five SiPMs detected both the Cherenkov light generated by the beam electrons and the calibration photon pulses coming from the laser system through the fiber.
Laser calibration pulses were guided to the front face of each calorimeter element by means of optical fibers (Silica + PMMA), each ending on a reflective right-angle prism in order to inject the light in a direction parallel to the crystal axis.
The prisms and the terminal part of the fibers were held by a Delrin panel[1] that was positioned in front of the calorimeter.
Each SiPM was connected through a custom PIN-to-MCX signal cable to the digitizer and through an HDMI[2] cable to a custom breakout board, that is a common electrical component that take a bundled cable and breaks out each conductor to a terminal that can easily accept a hook-up wire for distribution to another device; it provided the bias voltage. The breakout board was also linked to a beagle-bone microprocessor[3] which was used to set control procedures and parameters of the SiPM front-end electronics, e.g. set gain values for each single SiPM and readout its temperature. It communicated with the

[1]Reduced version of the panel that will be used for the full-size calorimeters manufactured at LNF mechanics workshop.
[2]HDMI stand for High-Definition Multimedia Interface.
[3]It is a low-power open-source hardware single-board computer.

SiPMs through the HDMI cables of the breakout board.
SiPMs were cooled by a continuos air flux, provided by fan units. Temperature control of the room was stable within 2°C.
For this test beam we used two different sets of crystals and SiPMs glued in two different ways:

- first set: 5 black wrapped crystal of PbF_2 with 5 SiPMs coupled to them only with optical grease and black tape. This configuration was sufficient to obtain useful information but unfortunately the coupling was not perfect and one SiPM board was damaged so, in the first days, we took data just from 4 out of 5 SiPMs;

- second set: one crystal wrapped in white Millipore paper while the others were left with black Tedlar. The most important difference was in the SiPMs coupling: they were glued to the rear face of the crystals ensuring a better coupling, no need of tape, which resulted in a better cooling, and differences between crystals due to small displacements of the SiPMs with the optical grease were avoided. The overall result of this change was a cleaner signal with better working conditions of the whole calorimeter.

6.1.2 Laser system

The experiment tested the full distribution chain that will be used to send light to all 1296 channels of the muon g-2 experiment. The setup is illustrated in Figure 6.3.
The light source was a pulsed laser (PicoQuant LDH-P-C-405M), having a maximum pulse energy up to 1 nJ, a pulse width of about 700 ps at a wavelength of (405 ± 10) nm, with a repetition rate that can be varied from low frequency to 40 MHz; a custom made electronic board selected the rate providing the trigger to the laser.
One of the important measurements performed at the test beam was the effective luminous energy that the distribution system can deliver to the calorimeter in order to choose the intensity at which the laser light source should work.

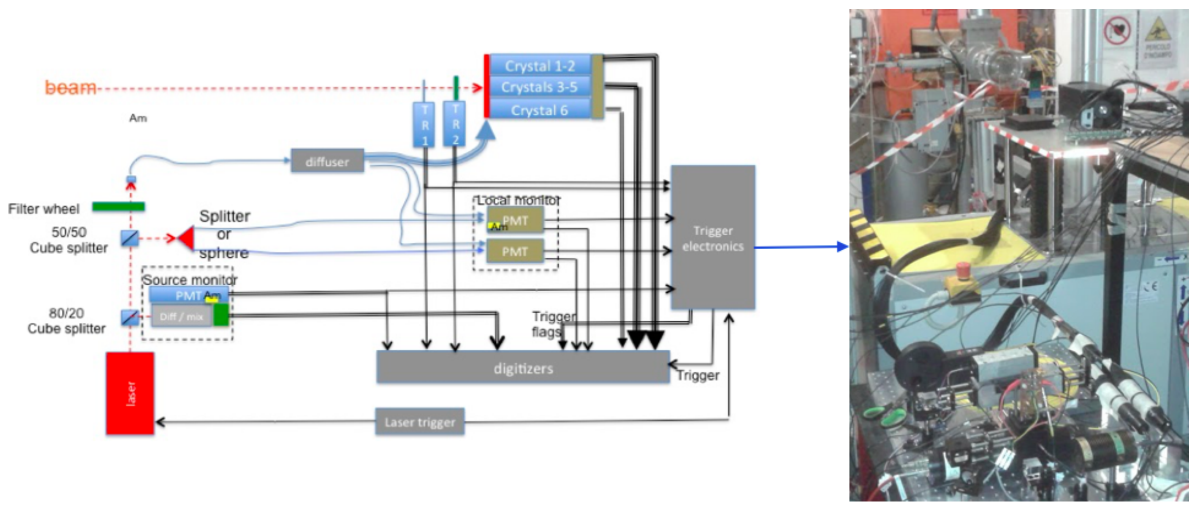

Figure 6.3: Schematic view of the baseline setup proposed for this Test Beam: full calibration system + detector system.

Laser distribution system

Part of the laser light was sent to the monitoring system by two beam splitter cubes (80/20 cube splitter + 50/50 cube splitter) and a Filter Wheel (FW), whose transmission factor could be selected manually or via computer[4]. Changes in the optical configuration led to variations of the laser pulse energy reaching the calorimeter.
The laser beam was then coupled and focussed into a 400 μm diameter and 25 m-long fused silica fiber, with about 30 dB/km loss at 400 nm. Although a fiber of this length was not required, it was used in order to simulate the running conditions of the E989 experiment. The fiber output was recollimated and transmitted through an engineered diffuser produced by RPC Photonics, consisting of structured microlens arrays that transform a Gaussian input beam into a flat top one. A fiber bundle made of 1 mm diameter fibers in PMMA was positioned at about 4 cm from the diffuser.
Five of the fibers, each 3 m long, were finally connected to the light distribution panel, as shown in Figure 6.2, two other fibers were connected to two separate photomultipliers (Photonics PMTs) which were part of the Local Monitor, in order to monitor the signal sent to the detector at the end of the distribution chain.

Monitoring system

The monitoring system consisted of a Source Monitor (SM) and a Local Monitor (LM). Part of the laser light was delivered by a beam splitter to the SM, whose tasks have already been described in the previous chapter.

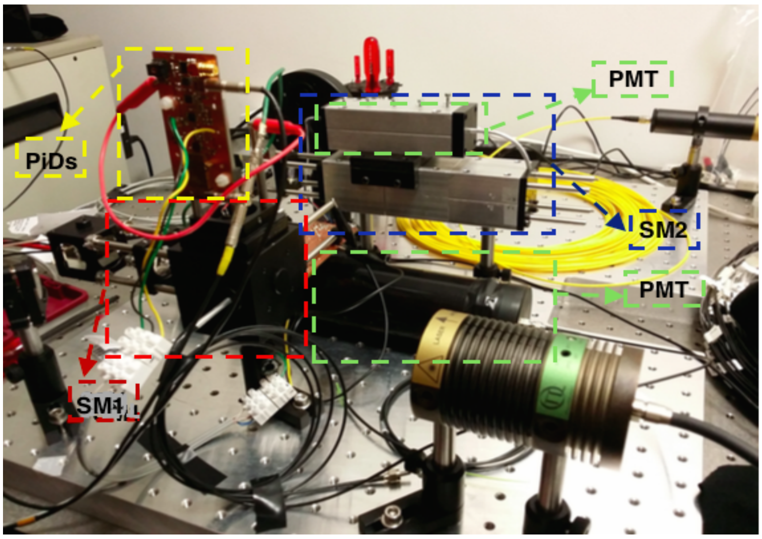

Figure 6.4: Picture showing the two Source Monitors. The two devices were installed in cascade to give the right amount of light each.

Two different designs of the SM, which differed with respect to the method employed to eliminate beam-pointing fluctuations, were tested:

[4]The transmission light rate varied from 100 % to 0.01 % (12 different intensity steps).

- first configuration: the light was mixed by an integrating sphere; this configuration was really interesting because it gave the possibility to send a reference signal to the Local Monitor corrected exactly in the same way and with the same device as the SiPM signal, and also ensured high levels of uniformity because of the integrating sphere. The only drawback was the high level of light loss of the integrating sphere which constrained to send an high percentage of the primary light source to the Source Monitor;

- second configuration: the light from the splitter was mixed by a combination of an engineered diffuser and a reflective mixing chamber; this configuration reflected the need to have less light as input than the sphere configuration, paying with a loss in the uniformity of the light that reached each detector.

In both cases, the mixed light was viewed by a redundant system composed by:

- two large area PIN diodes (PiDs): they are inherently stable, gain 1, high speed devices which operate at low bias; their low gain requires high light input which leads to high statistical accuracy[5];

- a wavelenght shifter (wls) which illuminated a PMT together with the absolute ^{241}Am reference signal.

The reference signal was necessary to correct for eventual instabilities in the PMT gain and, since both the PMT and the PiDs saw the same laser signal, it checked the stability of the PiDs in a time interval sufficient to accumulate the required statistics: it was possible to use the PiD to correct for drifts of the detectors and the PMT Americium signal to correct for laser light fluctuations. This procedure permits to have control of both of the possible sources of systematics which can be caused by drifts of a single kind of detectors (for example common fluctuations of the PiD due to same temperature behavior and so on) and also to the laser light source itself.

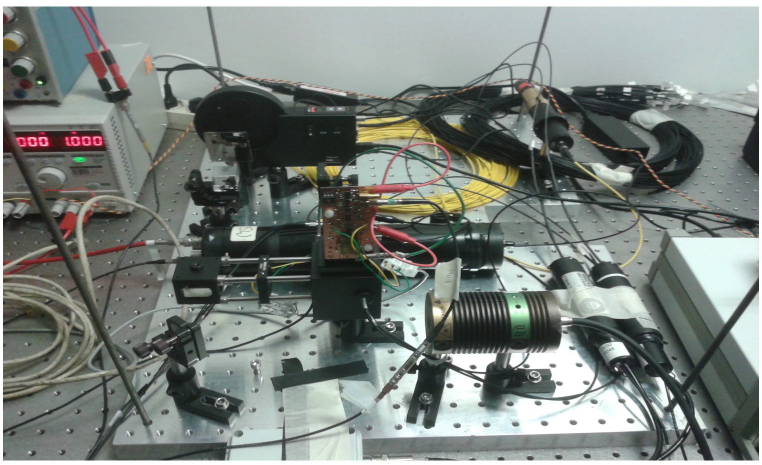

Figure 6.5: Overview of the calibration system.

[5]The intensity of the lasers required for this experiment was insufficient to generate a usable signal without amplification so that the stability check provided by the reference pulser was important.

The SM furnished also the reference signal from the laser source to the LM via 2 optical fibers.
The Local Monitor is also a redundant system composed by two Photonics PMTs.
In this configuration, both LM PMTs received a fraction of the light pulse sent to the SM (1 fiber for each PMT which furnished the reference signal) and to the calorimeter (1 fiber for each PMT: they were 2 out of the 56 PMMA fibers which will be used to send laser light to all of the 54 crystals) through the light distribution fiber bundle.
The two LM pulses were separated in time by more than one hundred nanoseconds. The ratio of the second to the first pulse intensity was a direct measurement of the stability of the distribution chain. The short time distance between the signals minimized the possibility of PMT gain drifts between the two signals.

6.2 Acquisition system (DAQ & Trigger)

For this test it was necessary to acquire 18 different signals considering both detectors and trigger. The DAQ system consisted of two digitizers, a 16 channel CAEN DT5742 5 GS/s and a 8 channel DT5730B 500MS/s, together with a custom DAQ software used also in previous test beam.

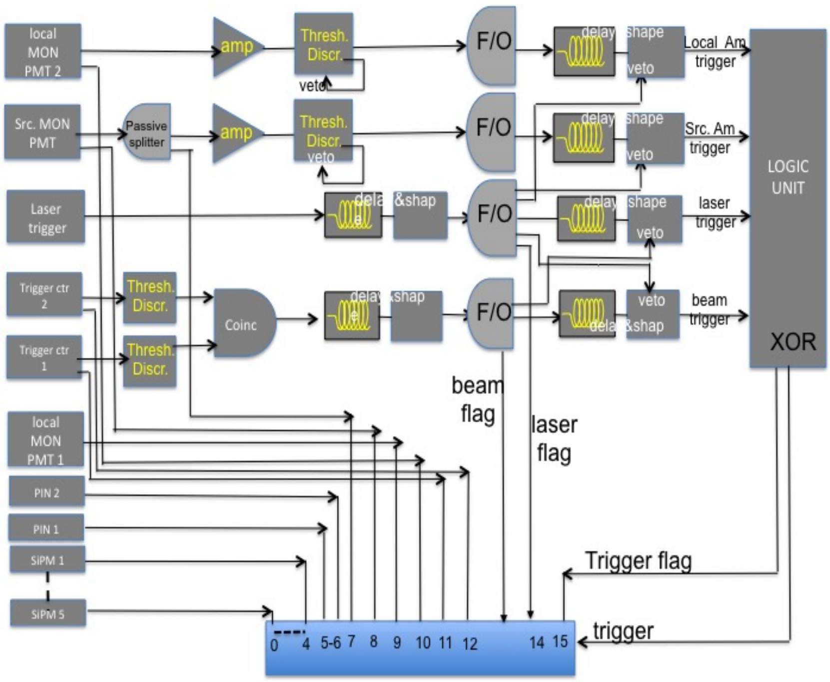

Figure 6.6: TB electronics scheme.

As shown in Figure 6.6, the acquired signals were:

- 5 SiPMs signals;
- 2 Local Monitor PMT signals;
- 2 PIN Diode signals;

- 1 Source Monitor PMT signal and 1 Source Monitor Americium signal;
- 5 flags necessary to identify: trigger, laser, beam, Americium (X2);
- 2 signals from the “finger” scintillators, which are helpful to identify beam induced events.

Three different types of trigger were provided to the DAQ:

- beam trigger (physical signal);
- laser trigger (calibration signal);
- Americium signal from the Source Monitor (reference signal);

Simple NIM signals were used as trigger coming from the electronics. Each signal, coming from the distribution chain, was sent to different timing units to set the proper time delay in order to ensure the correct timing between the different devices.

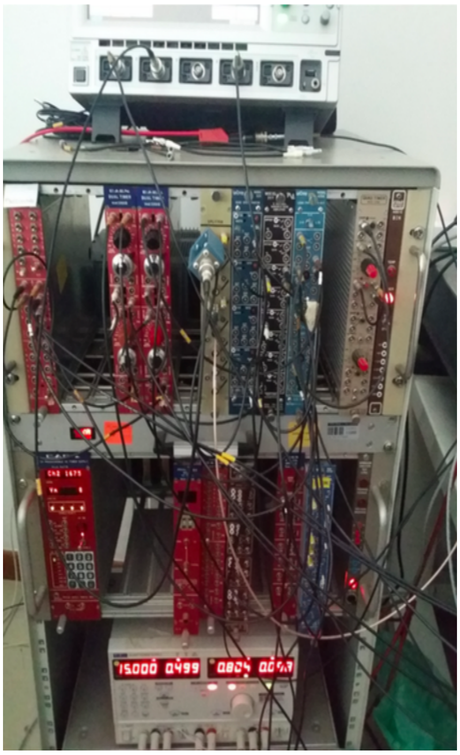

Figure 6.7: Picture of the hardware system used to setup the trigger for the Test Beam in Frascati.

Different types of trigger were obtained from the provided signals:

- beam trigger: to improve the single particle determination and p.e. reconstruction. This type of trigger was realized using 2 “finger” scintillators placed in front of the calorimeter together with a signal coming from DAΦNE; the scintillators acted as event selectors, identifying just beam induced events and helping in data analysis;

- laser trigger: it came from the laser driver; after being delayed through timing units, it operated as a VETO for the Local Monitor, the Source Monitor and the beam trigger itself;
- SM Americium trigger: it was realized after splitting, amplifying of a 5 factor, discriminating (Discriminator Threshold: 30 mV) and delaying the SM PMT signal;

The "final" experimental trigger was realized through a fold logic unit which provided an exclusive OR (XOR) of the 4 triggers mentioned above.
Some temperature sensors were also acquired, including room, SiPM and electronic board temperatures.
Finally, flag signal were very important for analysis purposes because they allowed to distinguish signals coming from each device.

Figure 6.8: Examples of different signals.

6.3 Local Monitor tests

When the beam was not enabled, some calibration tests, concerning Local Monitor PMTs, took place. The main target of these tests was to understand the PMT supply voltages which had to be used during the TB; the calibration was performed varying Filter Wheel positions, a process that implied different light transmission factors.
First of all, we used default supply voltages (LM1: HV=900 V; LM2: HV=950 V, black dots in Figure 6.9); data were acquired at the low rate of 8 Hz.
Signal(-baseline) pulse heights were used as a quick check.
Measurements were taken before and after the FW, see Figure 6.9:

- before FW: signals were coming from the beginning of the distribution chain, i.e. coming from the Source Monitor (Laser signal);
- after FW: signals were coming from the end of the distribution chain, namely the same signals that were sent to the calorimeter (Calibration signal).

Using default voltages, PMTs saturated when the transmission factor exceeded 35 % of the light addressed to the FW.
Using another configuration, (LM1: HV=950 V; LM2: HV=1000 V, red dots in Figure 6.9), PMTs saturated when the transmission factor exceeded 21 % of the light addressed to the FW.

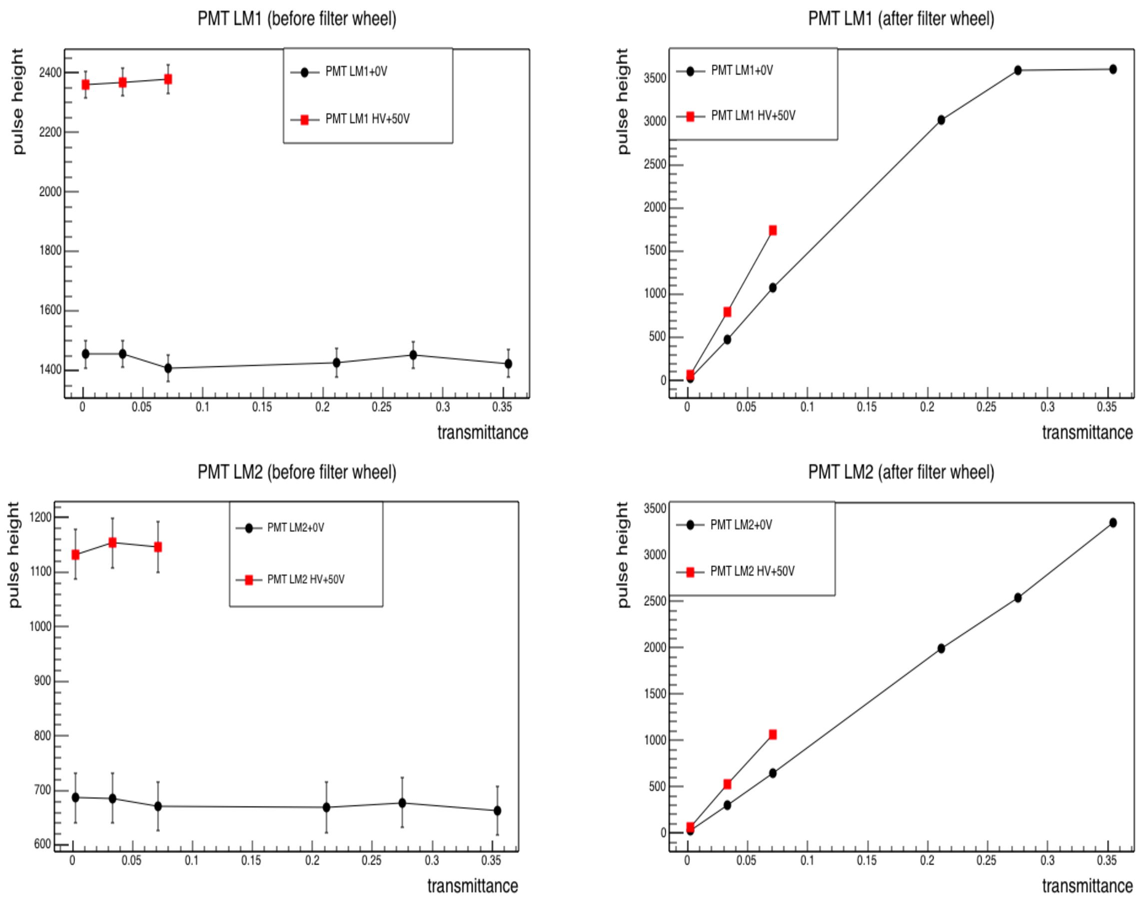

Figure 6.9: LM PMT signals observed at LM1 and LM2 for two different HV settings; statistical uncertainties are included.

The PMT saturation had to be taken in account in order to guarantee the high accuracy level required for the experiment. After increasing again PMT supply voltages, we obtained saturated signals for every transmission factor.
These plots reflect what we expect: before the FW pulse heights were almost constant (the signal didn't change while the FW position changed); after the FW pulse heights increased almost linearly increasing the light transmission factor (apart from becoming flat when the signal was saturated).

Since PMT working point seems to be at higher supply voltages (1100-1200 V), as it will be explained in the next chapter, the insertion of a light filter is being planned to avoid saturation problems.
Further studies have been pursued, in order to understand PMT responses varying laser frequencies: a laser control board designed by the Napoli group was employed for this purpose.
Data were acquired at 20.4 Hz, 134.4 Hz and 243.2 Hz (LM1: HV=900 V, black dots; LM2: HV=900 V, red dots), see Figure 6.10.

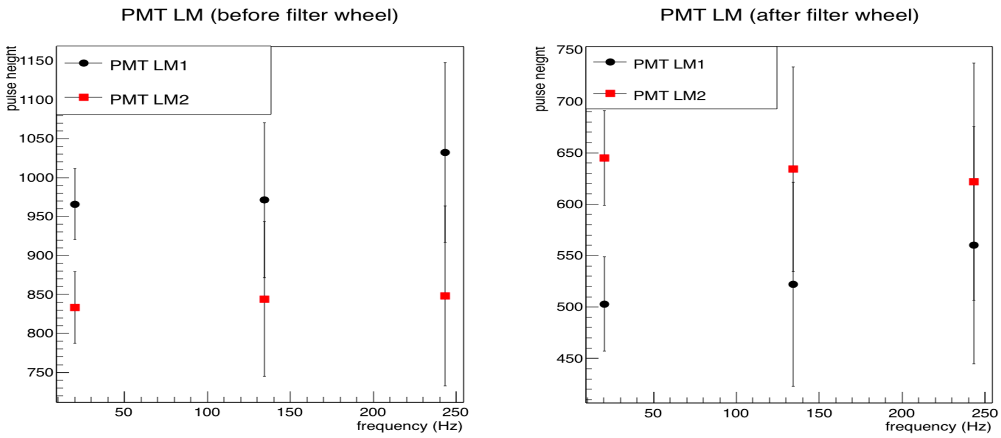

Figure 6.10: LM PMT signals observed at LM1 and LM2 for three different pulse frequencies; statistical uncertainties are included

Looking at data before and after the FW, the PMT responses are stable with respect to frequency variations (with a fixed transmission factor) but different PMT gains were evident; the change in attitude of LM1 compared to LM2 (higher pulses in the left plot of Figure 6.10, lower pulses in the right plot) is an effect that is evident in other plots (Figure 6.14, 6.15 and 6.17): it could be an indication of a different light transmission factor between the fibers which illuminate LM1 and LM2. A stricter selection of the PMTs used is needed to grant a similar behaviour between the LMs.

6.4 Analysis

The signals from the different sources are shown in Figures 6.11 and 6.12. Each signal is the result of the selection of a particular digitizer channel.
In order to acquire every signal, the trigger was delayed with respect to the other signals, as shown in Figure 6.8: digitizers in a common stop mode of operation, stop at a trigger signal arrival, freezing all the analog memory buffers and subsequently digitizing them into a digital memory buffer. In order to process signals, simple algorithms have been used. In this section we are going to focus the attention on the Local Monitor Analysis. TB results will be briefly reported in the following section.

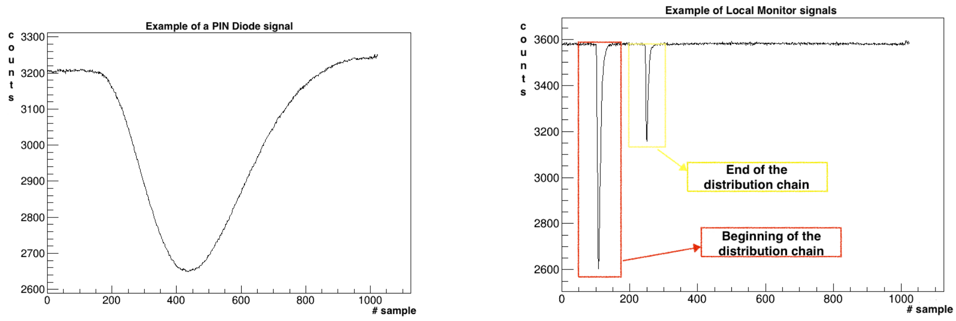

(a) (b)

Figure 6.11: (a): PIN Diode signal; (b): Local Monitor signals (16 channel CAEN DT5742 digitizer).

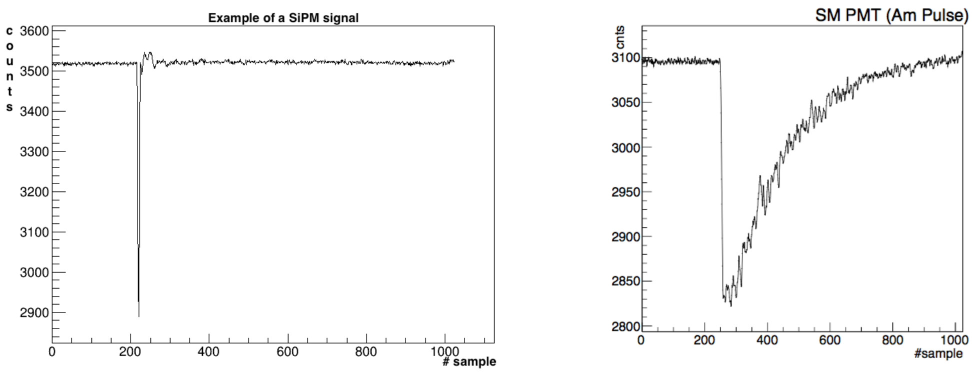

(a) (b)

Figure 6.12: (a): SiPM signal; (b): Americium signal (16 channel CAEN DT5742 digitizer).

6.4.1 LM PMT selection procedure

The analysis went through several steps, in order to select Local Monitor “good” events:

- first step: laser events were selected after looking at laser flag signals; integrals of the laser flag signal provided a threshold above which events were considered good (LASER ON); the 16 channel CAEN DT5742 digitizer was used;
- second step: the baseline of the LM signals, for each event, was estimated as the mean of the first 80 bins (bins with just electronic noise); 1 bin is $\sim$ 200 ps;
- third step: the first and second LM signal, which came from the beginning (first) and the end of the distribution chain (second), separated by about 100 ns, were selected through a threshold on the amplitude (related to the time span between the two signals).

Fluctuations on the light distribution were measured by the LM. They corresponded to the fluctuations in the ratio of the signal from the end of the optical transmission line and the signal from the SM (a fiber coming from the integrating sphere). Since both signals

were detected by the same PMT this ratio was insensitive to fluctuations in the PMT gain.
The LM PMT analysis was developed starting from the distribution of PMT pulse integrals, an example of which is shown in Figure 6.13: this distribution was used to extract, through a gaussian fit, the mean value of the pulse integral and its statistical error.
Two different sets of runs were analyzed:

- calibration runs from 1081 to 1090 ($\sim$ 30 minutes); the FW transmission factor varied from 100 % to 3 % of the light: I studied these runs in order to estimate the number of photoelectrons produced by the laser pulse and to verify the linearity of the response varying the FW positions;

- beam (impinging in the central crystal) runs from 1100 to 1107 ($\sim$ 4 hours); the FW transmission factor was 100 %, it was not changed during this set of runs: I studied these runs in order to monitor the LM stability in time.

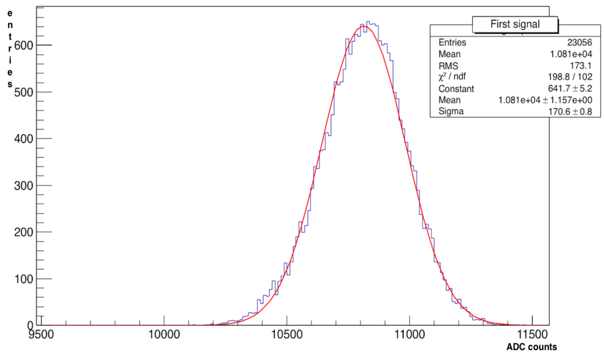

Figure 6.13: Example of LM pulse integral, gaussian fit.

Calibration runs (1081-1090)

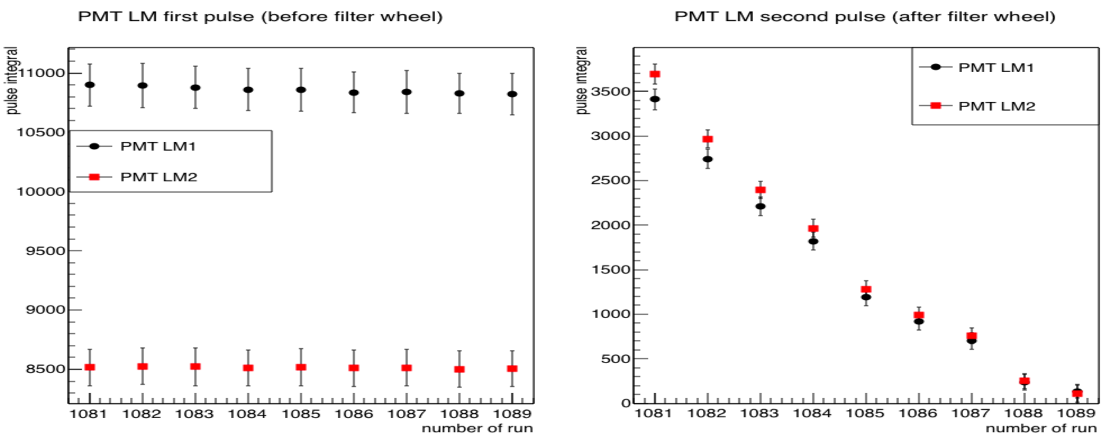

Figure 6.14: LM PMT response to laser light; on the left: first pulses, with mean integral constant with time; on the right: second pulses with mean integral varying with run conditions.

The stability of the system could be checked looking at first pulse integrals for both LM1 and LM2: as shown in the left plot of Figure 6.14, PMT responses didn't change over time (slopes from linear fits consistent with 0). However it is clear that PMT gains were really different as already observed.
Looking at the plot on the right side then, a difference between the two plots is evident: PMT integrals linearly decrease with different FW transmission factors, but integral values are almost superimposed. To better understand this (a priori) unexpected behavior, I plotted the ratios of the second over the first pulse integral vs. FW transmission factors. Since the ratio is not sensitive to PMT gain, I expected to see the same slope (of the fitting lines) for both PMTs. The fact that the slopes are different, including the uncertainties, could be index of a non-uniformity of the fibers which carried the light to the PMTs.

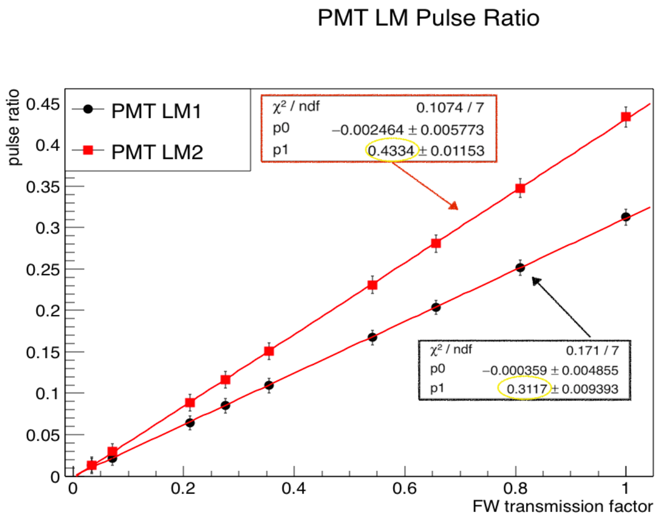

Figure 6.15: Ratios of the second over the first pulse integral for both LM1 and LM2.

PMT Calibration

Since the PMT response is linear, the PMT signal is expected to be proportional to the number of photoelectrons, $n_{p.e.}$:

$$(\mu - \beta) = k \langle n_{p.e.} \rangle$$

where μ is the mean of the PMT pulse integral distribution, after the baseline subtraction, β; the signal variance is the sum of a photoelectrons' statistics term, $\sigma^2_{p.e.}$, an electronic noise contribution, σ^2_e, and the intrinsic laser pulse fluctuations, $\sigma^2_L = (\alpha k 1(\mu - \beta))^2$, where α is the average relative laser intensity variation, which has been measured to be less than 1 %.

$$\sigma^2 = \sigma^2_{p.e.} + \sigma^2_e + \sigma^2_L$$

Since the p.e. component follows the Poisson statistics, assuming statistical independence of the three sources of fluctuations, the dependance of σ^2, as a function of the measured light intensity is given by:

$$\sigma^2 = k^2 \langle n_{p.e.} \rangle + \sigma^2_e + \sigma^2_L = k(\mu - \beta) + \sigma^2_e + \sigma^2_L$$

The proportional factor k can be obtained by fitting a parabola to σ^2 vs $(\mu - \beta)$, values obtained by calibration runs ($\sigma^2_{p.e.} \propto (\mu - \beta)$, $\sigma^2_L \propto (\mu - \beta)^2$).
Figure 6.16 shows an example of σ^2 vs $(\mu - \beta)$ plot for calibration runs.
The maximum number of photoelectrons, which is $\approx 3780 \pm 61$, calculated for the highest FW transmission factor (100 %) is consistent with values calculated from other calibration runs with a lower transmission factor. As an example, runs from 1010 to 1016 lead to: $n^{max}_{p.e.} \approx 2460$ (65,61 %) $\rightarrow 3750 \pm 61$ (100 %).

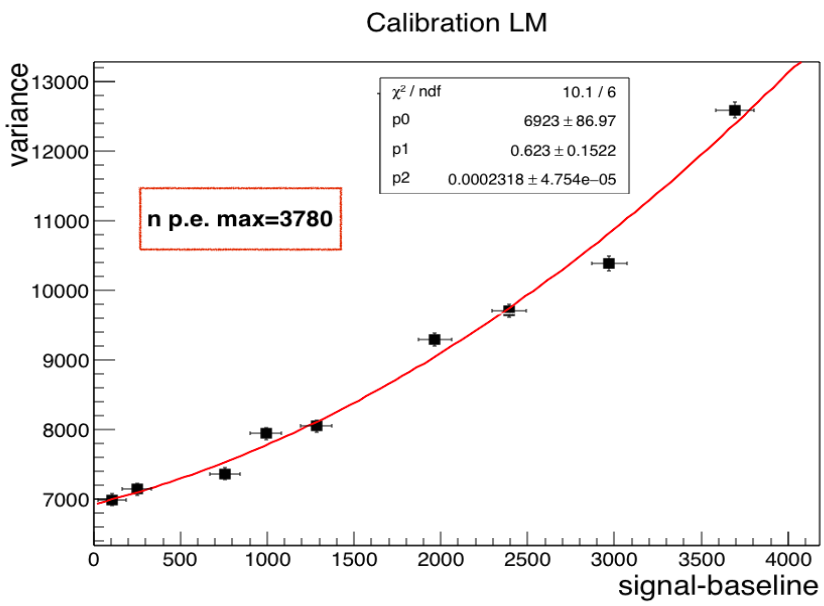

Figure 6.16: LM calibration curve.

Runs with beam

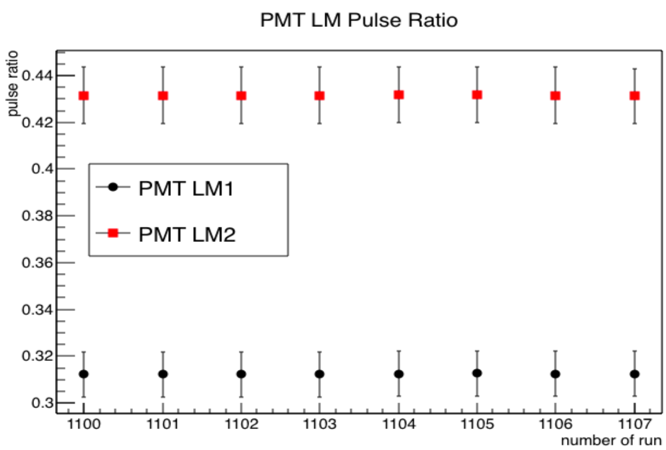

Figure 6.17: LM stability.

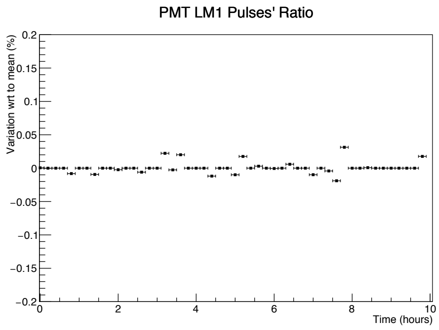

(a)

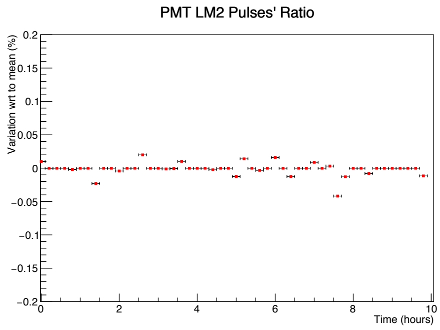

(b)

Figure 6.18: (a): LM1 pulses' ratio; (b): LM2 pulses' ratio.

I studied the LM stability in time ($\sim$ 4 hours) considering runs with beam, keeping the same FW setting, i.e. a 100 % light transmission factor. Looking at plots, which represent the ratios of the second over the first LM pulse, it is clear that ratios are constant; they are related to variations occurred through the distribution chain.
Within the uncertainties, they are consistent with the slopes of the fitting lines showed in Figure 6.15: these values can be used as correction factors.

Looking at the relative percentage variation, shown in Figure 6.18, that is (average of pulse integral-pulse integral)/(average of pulse integral), both LMs detected just a small fluctuation on the light distribution; the statistical resolution is 0.02 %.

6.5 Results

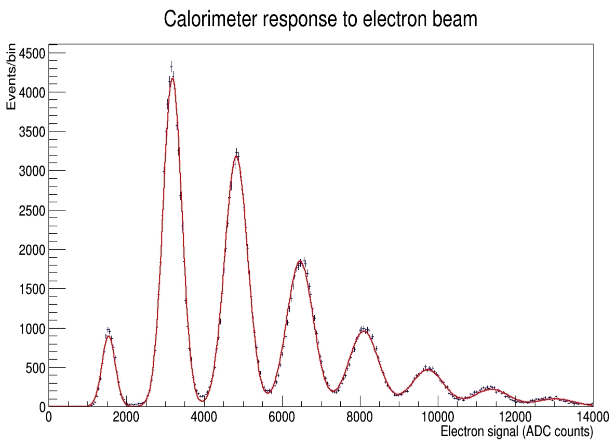

Figure 6.19: Calorimeter response to electron beam.

An example of the distribution of the calorimeter response to electrons is shown in Figure 6.19. The signal, L, observed by each SiPM in ADC counts is given by $L = k_2\nu$, where ν is the number of pixels fired[6]. This distribution was fitted with a sum of Gaussian distributions, where the means were assumed to be linearly related with the number of electrons simultaneously impinging in the calorimeter and their widths with their square root. The assumption on the widths was natural given the Poisson statistics of the number of fired pixels and assuming a contribution from the natural beam energy spread. The fit was typically well behaved ($\chi^2/ndf \approx 1$) and returned the mean value of the single electron peak in ADC counts. Taking the response to the laser with no Filter Wheel, dividing by the single electron mean and multiplying by the beam energy of 450 MeV, the response to the laser calibrated in equivalent energy was obtained. Typical values obtained in this test were around 800 MeV, which corresponded to a measured light power before the Filter Wheel of 11.2 ± 1.1 pJ. This value can be scaled to the laser power predicted in the final full calorimeter system, where 141 pJ are expected before the Filter Wheel instead of the 11.2 pJ measured here. The equivalent maximum energy seen by the calorimeter would then be 800 MeV$\times$ 141 pJ/11.2 pJ $\approx$ 10 GeV; 6 lasers will be sufficient to illuminate all 24 calorimeters with an equivalent energy of at least 10 GeV per laser pulse.

It was verified that the system presently is able to monitor and correct for laser intensity variations to 0.01 %. Variations in the distribution chain can be corrected by the LM at the same level on a longer timescale.

The energy of the electron incident on the calorimeter which is recorded by the SiPMs is expected to be affected by gain fluctuations connected primarily with temperature and bias voltage variations. By monitoring the response of the SiPMs to the laser pulses during data-taking it is possible to track and correct for these variations. The result of this correction process is illustrated in Figure 6.20 where the variations in the data taken during four hours of running, relative to the first data point, are shown before and after correction. Data points represent data averaged over 15 minutes of running. As shown in Figure 6.20, the data without any corrections exibits a positive drift of about 1.2 % over a four-hour run. After correcting for the laser calibration, the measured energy variations are made consistent with zero within the 0.3 % experimental error.

[6]See Section 4.2 (Photodetection Subsystem-SiPM) for details.

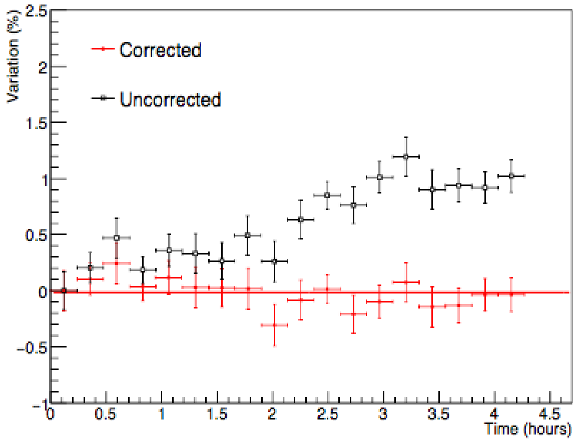

Figure 6.20: Variations in the measured energy of the electron beam during four hours of data acquisition. The black open circles show the long-term gain fluctuations in the raw data while the full-red circles are the same data after the laser-based calibration correction has been applied.

Comparing the 2 different SM configurations, no significative difference was observed but for a slightly smaller efficiency for the sphere solution.
Possible temperature-related fluctuations in the SM and LM photomultipliers were not relevant because only the ratios of simultaneous or nearly simultaneous signals from the same PMTs were necessary for the corrections as reported above.

Chapter 7

Laboratory tests

Due to the high level of accuracy required for the g-2 experiment, the response of every detector, including PMTs used for the LM, has to be precisely known; the distribution chain, including fibers and fiber connections, has to be fully tested in order to check its stability in time; the bias voltage, necessary to supply SiPMs, has to be constant over time, in order not to induce detector fluctuations.
In this chapter the tests I have performed to systematically assess the performance of the different parts of the system, are described.

7.1 Local Monitor PMT tests

7.1.1 Laser source: rate tests

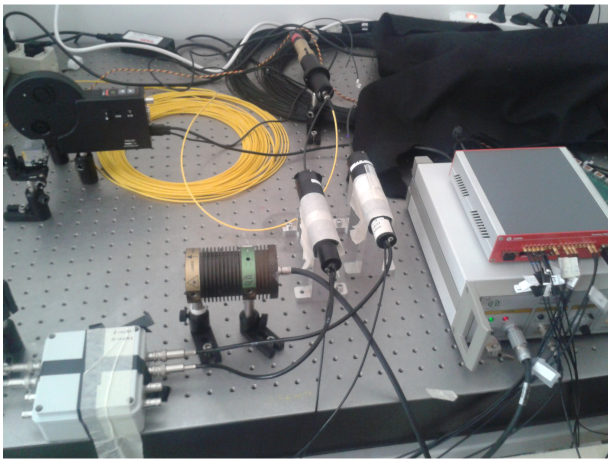

Figure 7.1: Setup of laser measurements

The first tests adopted the same configuration already seen in Frascati Test Beam, as shown in Figure 7.1, illuminating LM PMTs through fibers coming from an integrating sphere and from a fiber bundle. Laser light intensity was 750 pJ; FW transmission factor was 0.3 %, a factor chosen after proving that too much light made signals saturated; laser pulse repetition rate was changed in order to test the PMT response varying rates and

high voltages. Since laser pulse rate could be set just from 8 MHz to 500 kHz, an external trigger was requested; this kind of trigger was provided by a quad timer, which sent a NIM signal to the external trigger input of the laser driver with an adjustable frequency. The plots in Figure 7.2 present the results of measurements taken with three different frequencies, comparable with the ones expected for LM PMTs in the experiment:
f=1.4 kHz, f=5 kHz, f=14.8 kHz. High voltages were changed from 700 V to 1300 V.

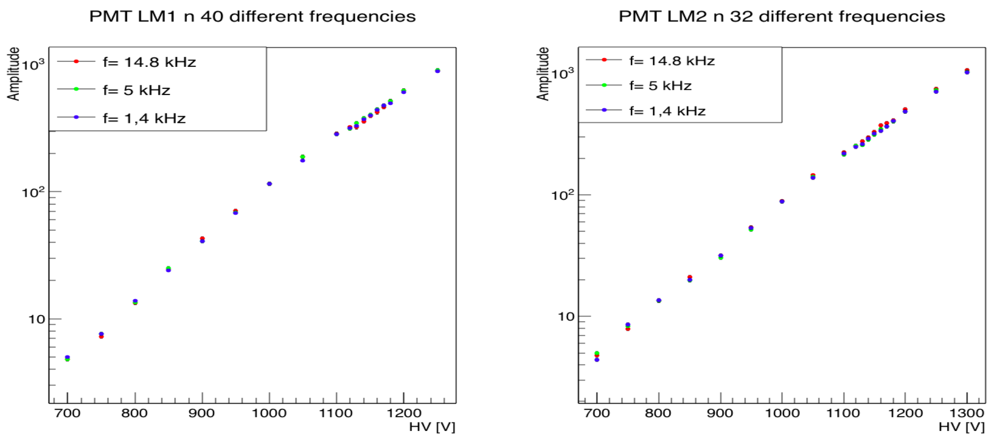

Figure 7.2: Amplitude vs High Voltage for different frequencies.

There is no evidence of a different PMT response varying frequencies; the output pulse height of a photomultiplier tube increases according to a power law with increasing supply voltages, even if the light level is kept constant, as it is expected.
A comparison between LM1 and LM2 response with a fixed frequency (14.4 kHz) decreasing the amount of laser light (half of the light), is shown in Figure 7.3. After testing more than 40 PMTs, I selected for this test two PMTs with similar gain (gain change of the photomultiplier tube directly affects the change of the output pulse height).

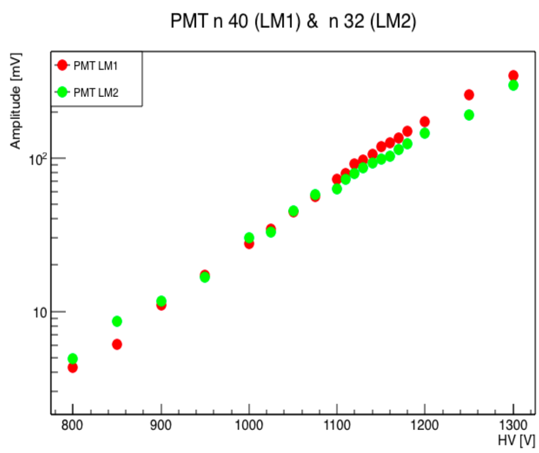

Figure 7.3: Amplitude vs High Voltage with a fixed frequency.

7.1.2 Cosmic rays: PMT plateau

To find the right PMT working point it was necessary to look for a "plateau" region in the Counting rates vs Voltage plane, a region in which small voltage supply oscillations would cause imperceptible efficiency variations; such a plateau is usually described in terms of its slope (in per cent change of count rate per volt) and its length in volts. Afterpulses, whose rate increases with the applied voltage, and dark noise, which is related to field emission, are important factors affecting the slope.
For this purpose, photon counting mode was chosen, since it ensures high stability even when the gain of the photomultiplier tube varies, as the gain is a function of the supply voltage [94]. These tests were realized using cosmic rays as light source and 2 NaI scintillators[1] coupled, through light guides, to the PMTs.
It didn't make sense to work with PMTs at the same voltage: in fact changing voltages at the same time would shift the "plateau" range. The value of the supplied voltage was kept fixed for one PMT at a time and varied for the other. It also had to be taken in account that PMTs should work over the "knee", which is the point where "plateau" begins and efficiency is not good enough, and that the voltage shouldn't be too high, not over 1300 V for these PMTs, in order not to stress detectors too much and avoid saturation.
The following electronics scheme was used in order to achieve the mentioned above goal.

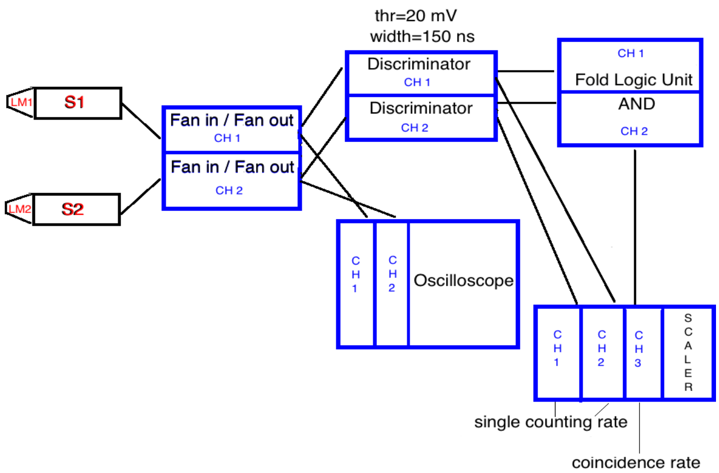

Figure 7.4: Electronics scheme.

The following procedure was followed:

- first step: find the plateau region fixing one PMT high voltage at a time; use fixed high voltages (1200 V, 1300 V, 1500 V) in order to better understand PMT response;
- second step: once the region has been found, fix PMT high voltage at the center of the region and look at the other PMT response in order to confirm the result.

[1]NaI stands for Sodium Iodide.

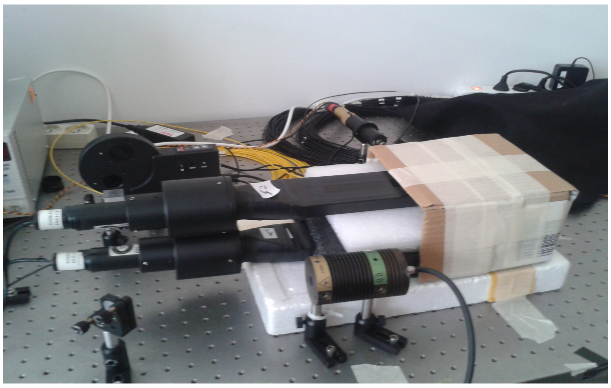

Figure 7.5: Setup of cosmic rays measurement.

Results obtained after the first step are shown in Figure 7.6: the plateau region amplitude is $\sim$ 50 V; regions with too high voltages (a threshold that was found working with the laser source) were not considered.

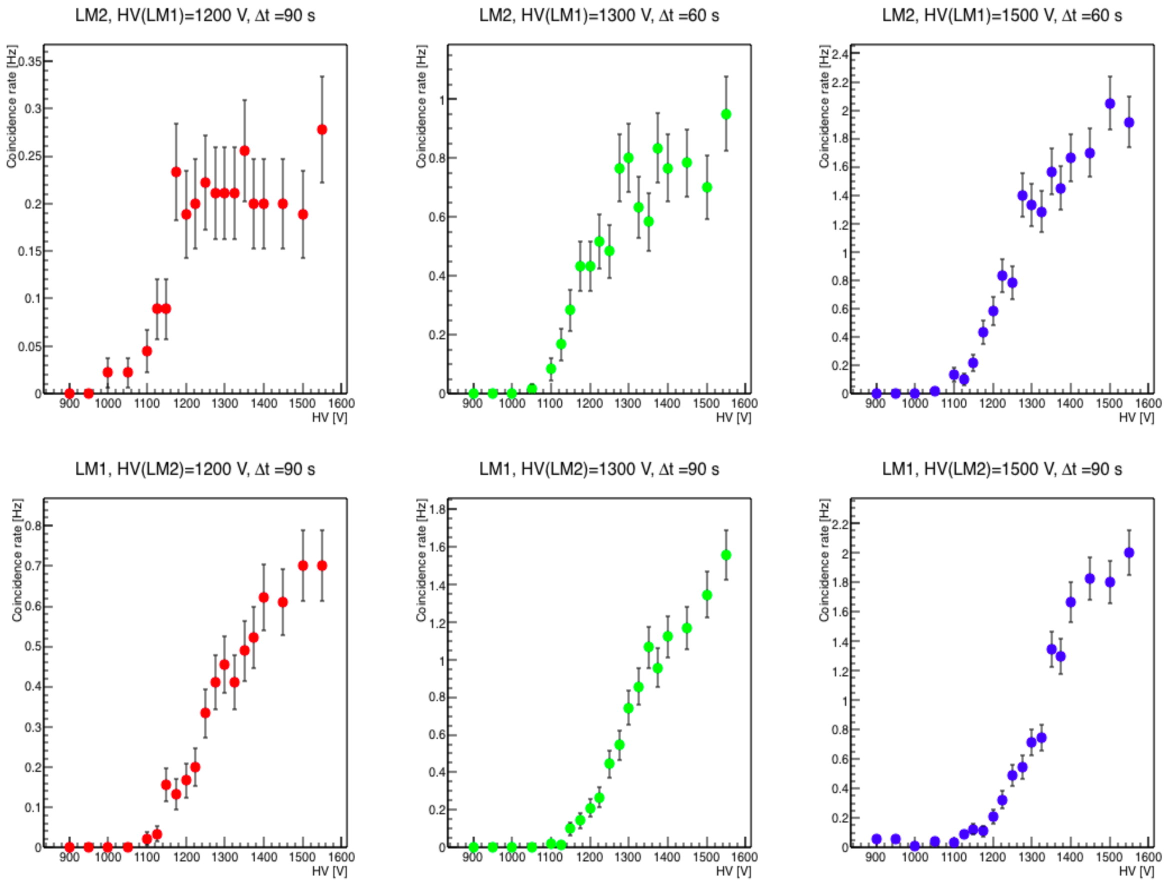

Figure 7.6: Plateau curves; Δt stands for the time span of the counting.

Results obtained after the second step are shown in Figure 7.7 and 7.8 for 4 different PMTs; it is clear that every PMT has its own plateau region, in fact in Figure 7.7 it seems to extend from 1150 to 1200 V, whereas in the left plot of Figure 7.8, it seems to extend from 1200 to 1250 V: this kind of tests should be performed over all PMTs to have right working points necessary for a stable PMT response.

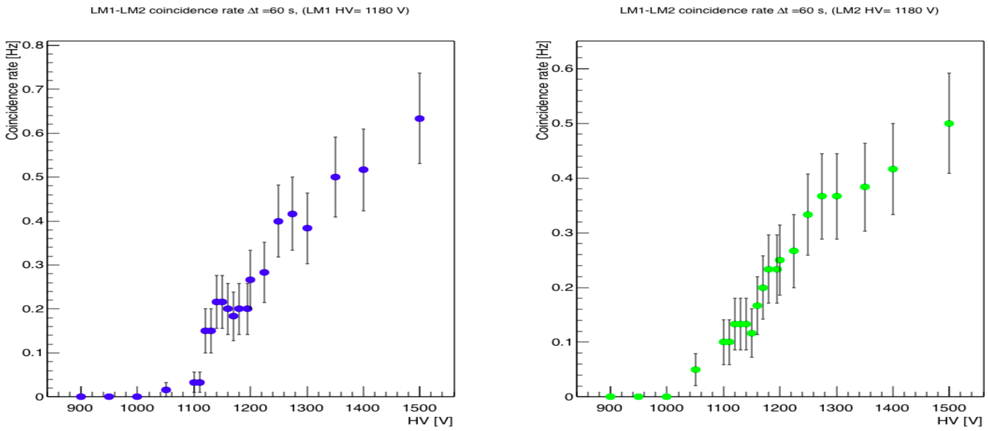

Figure 7.7: Plateau curves.

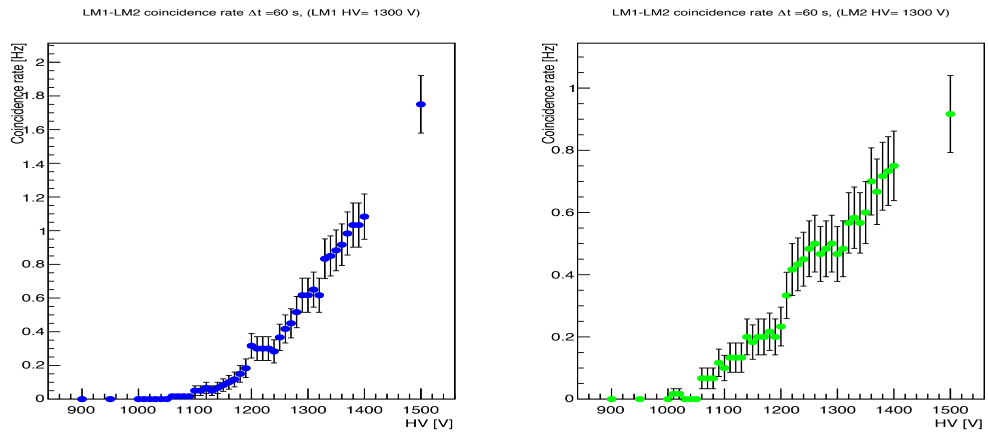

Figure 7.8: Plateau curves.

7.2 Splicing tests

To match the request of the experiment, the returning fibers to the LM must be disconnected from the distribution point whenever it's necessary. Two different possibilities were considered: cut and reconnect the fibers through a splicing, or using an optical connector. There are simple, but important differences between splicing and connecting. Connectors are used to couple two fibers together or to connect fibers to transmitters or receivers. They are also designed to be disconnected to allow patching to different locations and testing. Splices, however, are used to connect two fibers permanently. While they share some common requirements, like low loss, low back reflection and repeatability,

connectors have the additional requirements of durability under repeated matings.
Fusion splicing is the act of creating a continuous optical path for transmission of optical pulses from one fiber length to another (end-to-end) using heat. The goal is to fuse 2 fibers together in such a way that light passing through the fibers is not scattered or reflected back by the splice, and so that the splice and the region surrounding it are almost as strong as the virgin fiber itself. As a result, losses typically are in the range of 0.05 to 0.10 dB [95].
In order to join LM optical fibers, several tests, whose task is to compare light transmission factors and stability in time of connectors and spliced fibers, are being performed.
In this section preliminary tests concerning spliced fibers will be reported.

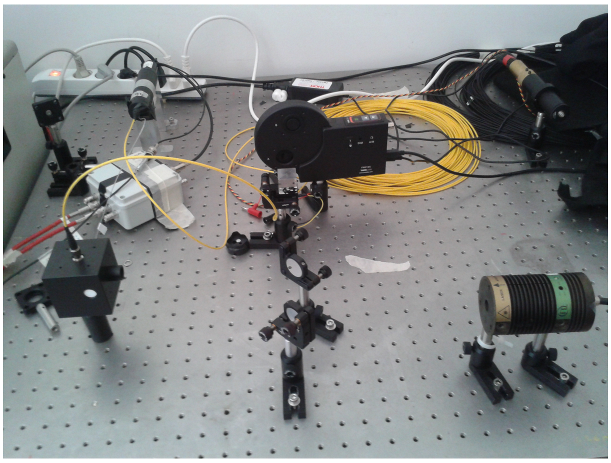

Figure 7.9: Setup of splicing tests.

The first goal of my tests was that of comparing light transmission between a nude and a spliced fiber; results are reported in the Table below.
Considering a laser signal of 2.57 mW, the mean ratio between a spliced fiber sample and a nude one indicated a light loss of $\sim 30\,\%$.
The main issue with spliced fibers was that the outcoming signal changed a lot ($\Delta \sim$ 200 nW), varying fibers; one possible explanation could be the use of different splicing fusion temperature for different fibers or some unexplained variations in the spliced fiber transmission factors resulting from this kind of technique.

	Fiber number	Offset (nW)	Signal (nW)	Light attenuation		Fiber number	Offset (nW)	Signal (nW)	Light attenuation
	1	36	1006	3,9E-04		9	33	287	1,1E-04
	2	36	995	3,9E-04		10	33	412	1,6E-04
	3	34	1025	4,0E-04		11	33	297	1,2E-04
FIBERS	4	35	1035	4,0E-04	FIBERS WITH SPLICING	12	34	272	1,1E-04
	5	35	1009	3,9E-04		13	34	299	1,2E-04
	6	35	1033	4,0E-04		14	35	320	1,2E-04
	7	35	1043	4,1E-04		15	33	397	1,5E-04
	8	36	1023	4,0E-04		16	34	481	1,9E-04

Figure 7.10: Splicing test results.

Although it would have been better to test identical fibers, which differed just for the splicing, in a further test mechanical restrictions of the experimental apparatus forced me to compare signal amplitudes coming from two fibers made of different materials, illuminated by the same laser source, as shown in Figure 7.11:

- a quartz, not spliced fiber (25 m long), which provided a signal amplitude of 128 mV;
- a spliced fiber which provided a signal amplitude of 154 mV and a signal larger than the quartz fiber one (enlargement due to the splicing).

Using a model which includes all fiber parameters, that are fiber diameter and fiber numerical aperture[2] (NA), the ratio between the two fibers, that theoretically should be 17.3, considering the real signal amplitudes is 1.2; this behavior should be investigated more carefully to be able to say that is caused by the splicing.

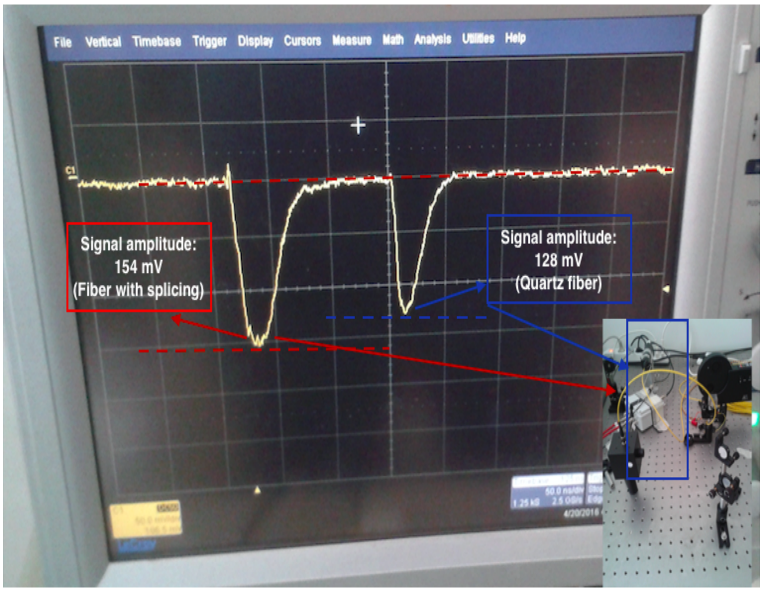

Figure 7.11: Signals from a quartz and a spliced fiber.

Since the light transmission factor obtained using connectors is $\sim 25\,\%$, in order to choose the best solution for the experiment, the key element would be the stability in time of the two options; tests concerning this issue are in progress.

7.3 Bias voltage tests

The response of a SiPM is quite sensitive to the bias voltage stability above Geiger-mode breakdown threshold. The SiPM Bias System must supply a bias voltage, V_{bias}, for each SiPM that is stabilized at the mV level, particularly over the critical $700\,\mu$s time window.
The SiPM pulse consists of two time components:

[2]Which is a dimensionless number characterizing the range of angles over which the system can accept or emit light.

- a fast rising edge caused by the Geiger discharge;
- a long falling edge due to the slow pixel recovery time τ_r which depends on the intrinsic properties of the SiPM and properties of the preamplifier: τ_r is defined by the value of the quenching resistor R_q, which quenches the avalanche and reduces the V_{bias} to V_{BD}, the breakdown voltage, or below, and the pixel capacitance C_{pix}, $\tau_r = R_q \cdot C_{pix}$.

After the recovery time τ_r, V_{bias} is restored and the pixel regained the charge due to the quenching resistor which terminates the avalanche formation to get the detector again sensitive to radiation.
In this process, however, a new avalanche called afterpulse, that affects the shape of the waveform on the decay time, may be triggered. The probability for afterpulses depends on the internal properties of the SiPM. Since afterpulses are delayed with respect to the original signal, their charge is only partially integrated over. This leads to photoelectron spectra with decreased resolution [96].

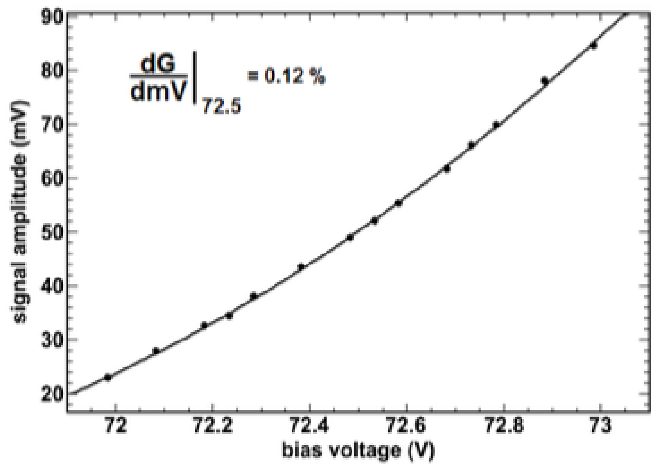

Figure 7.12: Gain vs. bias voltage. The measured change in gain is 0.12 % per mV [76].

Figure 7.12 shows the sensitivity of gain to bias voltage. At the projected operating voltage, the gain shift per millivolt is 0.12 %, which equates to a 50 ppb shift in ω_a if it were left uncorrected. The requirement to maintain mV stability or better is selected such that any necessary correction from bias voltage deviation is not large compared to the overall systematic error budget. Each SiPM has a preferred working point bias, so the system must allow each channel to be set to an individual bias voltage [76].

The whole experimental apparatus used for the Frascati Test Beam, except for the Local Monitor system, as shown in Figure 7.13, was used in order to test how the detector system reacts with a very high rate of laser pulses: the stability and recovery time of the bias voltage has been studied. In order to simulate beam fills, Figure 7.14, a waveform generator was used: it provided an exponential waveform used as a trigger, which simulated fills lasting 170 μs and spaced at intervals of 815 μs; the maximum rate was 1 MHz (the rate decreased with time).

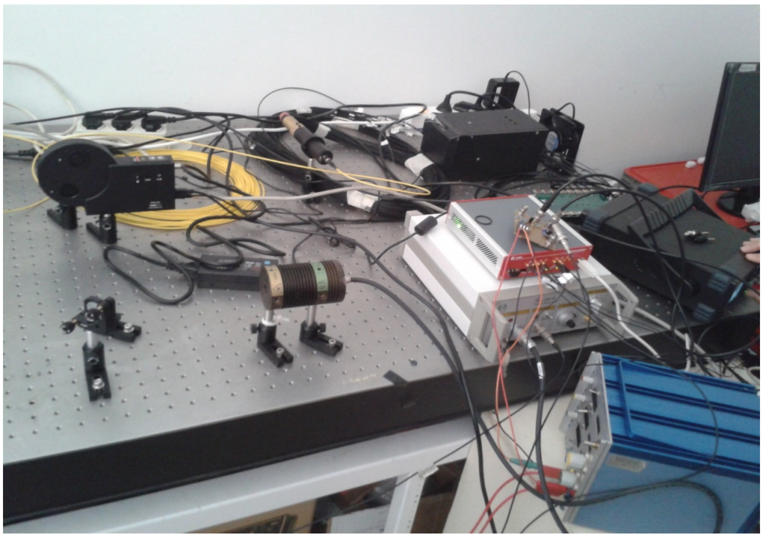

Figure 7.13: Setup of bias voltage tests.

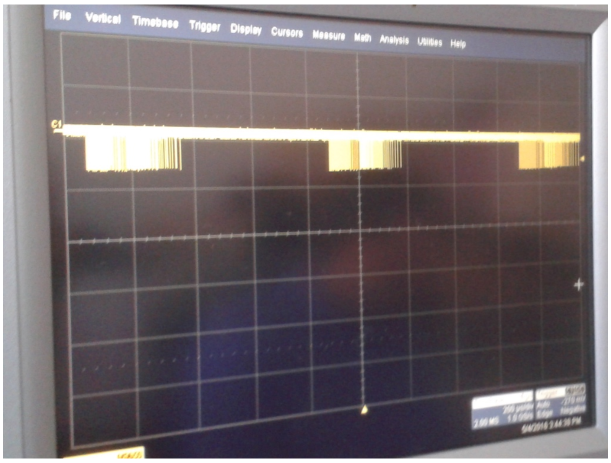

Figure 7.14: Example of a simulated fill.

A differential board, which made difference and amplification of the incoming signals, shown in Figure 7.15, was exploited in order to check bias voltage stability during the "fill". The incoming signals were:

- a reference stable signal of 67.8 V;
- the bias voltage that supplied SiPMs, see Figure 7.16, that was set at 67.8 V;

It is clear that a stable system should give a flat response in absence of voltage fluctuations. The signal coming from the differential board was obtained averaging 20 sweeps in order to smooth noise.

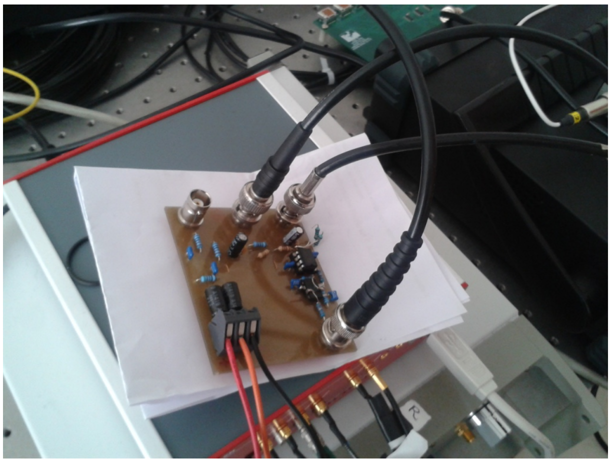

Figure 7.15: Differential board.

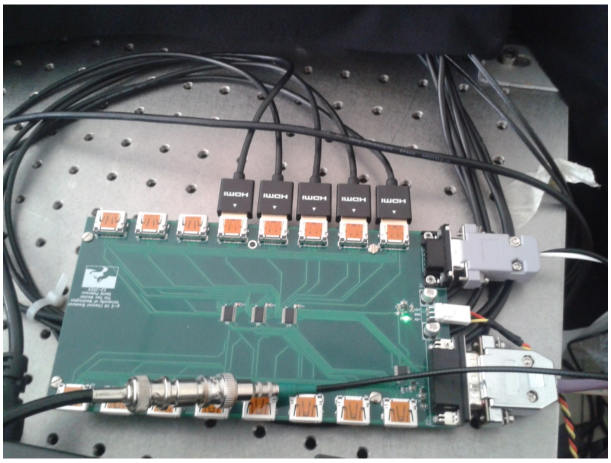

Figure 7.16: Breakout board which provided the bias voltage.

As well as shown in Figure 7.17 and 7.18, the difference is not equal to 0: it goes down when the fill arrives and it comes up when pulses start to thin out.
It also has to be noted that, with different configurations that are 1 supplied SiPM (Figure 7.17) and 2 supplied SiPMs (Figure 7.18), the bias voltage changes:

- first configuration: amplitude of the oscillation: 3.40 mV;
- second configuration: amplitude of the oscillation: 4.12 mV.

Other bias voltage supply systems are being tested in order to find a way to correct these fluctuations.

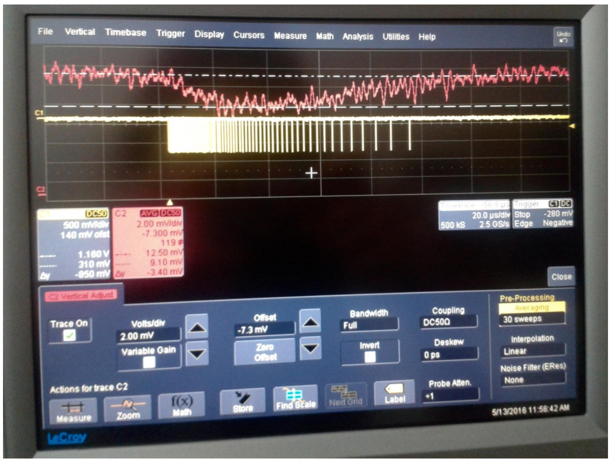

Figure 7.17: Fill and differential signal (1 SiPM).

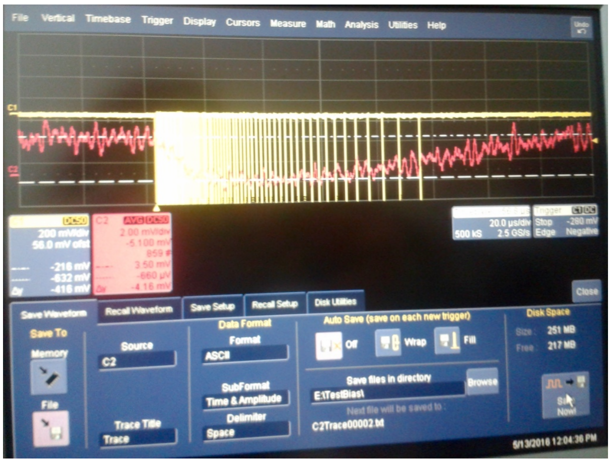

Figure 7.18: Fill and differential signal (2 SiPMs).

Conclusion

The calibration system of the muon g-2 experiment has been described in this thesis. During the Test Beam performed in Frascati, it was verified that the calibration system is presently able to monitor and correct for laser intensity variations to 0.01 %, and it has been proven that 6 lasers will be sufficient to illuminate all 24 calorimeters with an equivalent energy of at least 10 GeV per laser pulse.
Variations in the distribution chain can be corrected by the Local Monitor at the same level on a longer timescale: correction factors that could be applied during data analysis were obtained looking at Local Monitor signals.
Comparing two different Source Monitor configurations no significative difference was observed but for a slightly smaller efficiency for the sphere solution.
Possible temperature-related fluctuations in the Source Monitor and Local Monitor photomultipliers (PMT) were not relevant because only the ratios of simultaneous or nearly simultaneous signals from the same PMTs were necessary for the corrections.
Additional tests on the Local Monitor system proved that there is no evidence of a different PMT response varying the laser repetition rate; the output pulse height of a PMT increases according to a power law with increasing supply voltages, even if the light level is kept constant, as it is expected.
With regard to the right PMT working point, it is clear that every PMT has its own plateau region, which seems to extend for ~ 50 V, thus this kind of tests should be performed over all PMTs to have right working points necessary to a stable PMT response. However, plateau regions are surely not placed under 1100 V: since the operating supply voltages used for the Test Beam were $900 - 950$ V, chosen in order not to have too much light, the insertion of a light filter, which should be placed before the Local Monitor PMTs, is being planned; thus PMT features could be fully exploited.
The task of understanding how to disconnect two fibers without losing in intensity or stability led to tests concerning the connection of fibers. It was proven that both spliced fibers and connectors have high light losses, ~ 30 % of transmitted light for spliced fibers and ~ 25 % for connectors; in order to choose the best solution for the experiment, the key element would be the stability in time of the two options; tests concerning this issue are in progress.
Finally, the stability and recovery time of the bias voltage of the Silicon photomultipliers (SiPM) has been studied. The bias voltage oscillates at a few mV level; this oscillation increases considering a higher number of SiPMs; alternative supply voltage systems are being tested in order to minimize this kind of oscillation.

Bibliography

[1] Fred Gray: *A measurement of the anomalous magnetic moment of the positive muon with a precision of 0.7 parts per million*, *g*-2 Thesis, 2003;

[2] F. H. Combley: *g-2 factors for muon and electron and the consequences for QED*, 1979;

[3] B. Lee Roberts: *Precision Searches for Physics Beyond the Standard Model*, July 2009;

[4] I. Estermann, O. Simpson and O. Stern: *Phys. Rev. 52, 535*, 1937;

[5] Particle Data Group: *Phys. Rev. 38, 090001*, 2015;

[6] T. Kinoshita and W. B. Lindquist: *Phys. Rev. Lett. 47, 1573*, 1981;

[7] G. W. Bennett et al., Muon g-2 Collaboration: *Phys. Rev. Lett. 89*, 101804, 2002;

[8] M. Davier, S. Eidelman, A. Hocker and Z. Zhang: *hep-ph/0208177*;

[9] M. Acciarri et al., L3 Collaboration: *Phys. Lett. B434, 169*, 1998;

[10] M. A. Samuel, G.-W. Li and R. Mendel: *Phys. Rev. Lett. 67, 668*,1991;

[11] S. Gasiorowicz and J. L. Rosner: *Am. J. Phys. 49, 954*, 1981;

[12] W. E. Lamb and R.C. Retherford: *Fine Structure of the Hydrogen Atom. Part I, Phys. Rev. 79, 549*, 15 August 1950;

[13] F. Jegerlehner, A. Nyffeler: *The Muon g-2, Physics Reports Volume 477, Issues 1?3, Pages 1?110*, June 2009;

[14] J. Schwinger: *On Quantum-Electrodynamics and the Magnetic Moment of the Electron, Phys. Rev. 73, 416*, 15 February 1948;

[15] The NIST Reference on Constants, Units and Uncertainty, CODATA: *http://physics.nist.gov/cgi-bin/cuu/Valuegem*, 2016;

[16] Chris Polly: *A measurement of the anomalous magnetic moment of the negative muon to 0.7 ppm*,*g*-2 Thesis, 2005;

[17] M. Knecht: *The anomalous magnetic moment of the muon: a theoretical introduction, Lect.Notes Phys.629:37-84*, 2004;

[18] A. Czarnecki and William J. Marciano: *The Muon Anomalous Magnetic Moment: Standard Model Theory and Beyond, arXiv:hep-ph/0010194*, October 2000;

[19] M. Passera: *The Standard Model Prediction of the Muon Anomalous Magnetic Moment, J.Phys.G31:R75-R94*, February 2005;

[20] D. Chitwood: *A Measurement of the Mean Life of the Positive Muon to a Precision of* $11\,ppm$, 1999;

[21] L. Thomas: *Phil. Mag. 3, 1*, 1927;

[22] F. Farley and E. Picasso: *The muon g-2 experiments in Quantum Electrodynamics*, edited by T. Kinoshita, World Scientific, Singapore, 1990;

[23] J. Jackson: *Classical Electrodynamics*, 3rd ed. John Wiley and Sons, New York, 1999;

[24] V. Bargmann, L. Michel and V. Telegdi: *Phys. Rev. Lett. 2, 453*, 1959;

[25] M. Caffo, S. Turrini and E. Remiddi: *Phys. Rev. D 30 483*, 1984; E. Remiddi and S.P. Sorella: *Lett. Nuovo Cim. 44 231*, 1985; D.J. Broadhurst, A.L. Kataev and O.V. Tarasov: *Phys. Lett. B 298 445 [arXiv:hep-ph/9210255]*, 1993; S. Laporta: *Phys. Lett. B 312 495 [arXiv:hep-ph/9306324]*, 1993; P.A. Baikov and D.J. Broadhurst: *arXiv:hep-ph/9504398.*;

[26] T. Kinoshita, B. Nizic and Y. Okamoto: *Phys. Rev. Lett. 52*, 1984;

[27] T. Kinoshita: *Talk at Tau04, Nara, Japan*, September 2004;

[28] A. Hoecker (CERN), and W.J. Marciano (BNL): *The Muon Anomalous Magnetic Moment*, http://pdg.lbl.gov/2013/reviews/rpp2013-rev-g-2-muon-anom-mag-moment.pdf, August 2013;

[29] R. Jackiw, S. Weinberg: *Phys. Rev. D 5 2396*, 1972; I. Bars, M. Yoshimura: *Phys. Rev. D 6 374*, 1972; G. Altarelli, N. Cabibbo, L. Maiani: *Phys. Lett. B 40 415*, 1972; W. A. Bardeen, R. Gastmans, B. Lautrup: *Nucl. Phys. B 46 319*, 1972; K. Fujikawa, B. W. Lee, A. I. Sanda: *Phys. Rev. D 6 2923*, 1972;

[30] T.V. Kukhto, E.A. Kuraev, Z.K. Silagadze and A. Schiller: *Nucl. Phys. B 371*, 1992;

[31] C. Gnendiger, D. Stockinger, H. Stockinger-Kim: *The electroweak contributions to g-2 after the Higgs boson mass measurement*, arXiv:1306.5546v2, September 2013;

[32] C. Bouchiat and L. Michel: *J. Phys. Radium 22*, 1961;

[33] A. Vainshtein: *Hadronic effects in the muon anomalous magnetic moment*, William I. Fine Theoretical Physics Institute, School of Physics and Astronomy, University of Minnesota, March 2004;

[34] M. Davier and W. Marciano: *Annu. Rev. Nucl. Part. Sci. 54, 115*, 2004;

[35] T. Blum et al.: *The Muon g-2 Theory Value: Present and Future*, arXiv:1311.2198v1 [hep-ph], November 2013;

[36] M. Knecht, A. Nyffeler, M. Perrottet and E. de Rafael: *Phys. Rev. Lett.88*, 2002;

[37] K. Melnikov and A. Vainshtein: *Phys. Rev. D 70 113006*, 2004;

[38] J. Prades, E. de Rafael and A. Vainshtein: *Advanced Series on Directions in High Energy Physics - Vol. 20 Lepton Dipole Moments*, eds. B. L. Roberts and W. J. Marciano: *World Scientific, p. 303*; arXiv:0901.0306v1 [hep-ph], 2010;

[39] G. W. Bennett et al. [Muon g-2 Collaboration]: *Phys. Rev. D 73 072003*, 2006;

[40] H.N. Brown et al. [Muon (g-2) Collaboration]: *Phys. Rev. D 62 091101 [arXiv:hep-ex/0009029]*, 2000;

[41] H.N. Brown et al. [Muon (g-2) Collaboration]: *Phys. Rev. Lett. 86 2227 [arXiv:hep-ex/0102017]*, 2001;

[42] G.W. Bennett et al. [Muon (g-2) Collaboration]: *Phys. Rev. Lett. 89 101804 [Erratum-ibid. 89 (2002) 129903] [arXiv:hep-ex/0208001]*, 2002;

[43] J. Bailey et al. [CERN Muon Storage Ring Collaboration]: *Phys. Lett. B 67 225*, 1977; J. Bailey et al.: *Nucl. Phys. B 150*, 1979; F.J.M. Farley and E. Picasso: *Quantum Electrodynamics*, edited by T. Kinoshita (World Scientific, Singapore), pp. 479-559;

[44] For a review of tests of CPT invariance for muons, see V.W. Hughes: *J. Phys. G 29 181*, 2003;

[45] M. Davier, A. Hoecker, B. Malaescu and Z. Zhang: *Eur. Phys. J. C71 1515, 2011; Erratum-ibid. C72 1874*, 2012;

[46] K. Hagiwara, R. Liao, A. D. Martin, D. Nomura and T. Teubner: *J. Phys. G38 085003*, 2011;

[47] T. Aoyama, M. Hayakawa, T. Kinoshita and M. Nio: *Phys. Rev. Lett. 109 111808*, 2012;

[48] T. Blum: *Phys. Rev. Lett. 91 052001*, 2003; M. Gockeler et al. [QCDSF Collaboration]: *Nucl. Phys. B 688 135*, 2004; C. Aubin, T. Blum: *Phys. Rev. D 75 114502*, 2007;

[49] E. Eichten, K. D. Lane and M. E. Peskin: *Phys. Rev. Lett. 50, 811*, 1983;

[50] P. Mery, S. E. Moubarik, M. Perrottet and F. M. Renard: *Z. Phys. C46, 229*, 1990;

[51] J. Wess, B. Zumino: *Nucl. Phys. B 70 39*, 1974; R. Haag, J. T. Lopuszanski, M. Sohnius: *Nucl. Phys. B 88 257*, 1975;

[52] A. Czarnecki and W. J. Marciano: *Phys. Rev. D64, 013014, [hep-ph/0102122]*, 2001;

[53] B. Lee Roberts: *Experimental prospects for muon physics at a neutrino factory*, Plenary talk at NuFact08 (Valencia), 4 July 2008;

[54] C.J. Baker, et al.: *Phys. Rev. Lett. 97 131801*, 2006;

[55] B.C. Regan, et al.: *Phys. Rev. Lett. 88 071805-1*, 2002;

[56] G.W. Bennett et al.: *An Improved Limit on the Muon Electric Dipole Moment, arXiv:0811.1207v2 [hep-ex]*, July 2009

[57] M.V. Romalis, W.C. Griffith, J.P. Jacobs, and E.N. Fortson: *Phys. Rev. Lett. 86 2505*, 2001;

[58] V. Anastassopoulos et al.: *A Storage Ring Experiment to Detect a Proton Electric Dipole Moment* arXiv:1502.04317v1 [physics.acc-ph], February 2015;

[59] R. Garwin, L. Lederman and M. Weinrich: *Phys. Rev. 105, 1415*, 1957;

[60] J. Cassels et al.: *Proc. Phys. Soc. A70, 451*, 1957;

[61] S. Coffin et al.: *Phys. Rev. 109, 973*, 1958;

[62] R. Lundy et al.: *Phys. Rev. Let. 1, 38*, 1958;

[63] R. Garwin et al.: *Phys. Rev. 118, 271*, 1960;

[64] G. Bingham: *Nuovo Cimento 17, 1352*, 1962;

[65] D. Hutchinson et al.: *Phys. Rev. Lett. 131, 1351*, 1963;

[66] F. Combley, F. Farley and E. Picasso: *The CERN Muon (g-2) Experiments*, June 1980;

[67] G. Charpak et al.: *Phys. Rev. Lett. 6, 128*, 1961;

[68] H. Eland: *Phys. Lett. 21, 720*, 1966;

[69] D. Kawall: *Statistical and Systematic Errors in Fitting* ω_a*, Muon g-2 Internal Note No. 322*, 1998;

[70] J. Bailey et al.: *Nuovo Cimento Soc. Ital. Fis. A9, 369*, 1972;

[71] CERN Muon Storage Ring Collaboration, J. Bailey et al.: *Phys. Lett. B67, 225*, 1977;

[72] H. N. Brown and collaborators: *Revised rates for muon storage in the g-2 ring, Muon g-2 Internal Note No. 185*, 1994;

[73] G. Charpak et al.: *Nuovo Cimento Soc. Ital. Fis. 37, 1241*, 1965;

[74] R. M. Carey et al., *Phys. Rev. Lett. 82, 1632*, 1999;

[75] Muon g-2 collaboration: *Measurement of the Negative Muon Anomalous Magnetic Moment to 0.7 ppm*, arXiv:hep-ex/0401008 v3, February 2004;

[76] *Muon g-2 Technical Design Report*, June 2015;

[77] T. P. Gorringe, D. W. Hertzog: *Precision Muon Physics*, arXiv:1506.01465v1, June 2015;

[78] O. Rifki: *The muon anomalous magnetic moment: a probe for the Standard Model and beyond*, Report approved for the H.L.Dodge Department of Physics and Astronomy, 2014;

[79] M.E. Shenk: *A straw tube tracking detector for the new muon g-2 E989 experiment*, 2014;

[80] A. Anastasi et al: *The Calibration System of the new g-2 experiment at Fermilab, Nucl.Instrum.Meth. A824 716-717*, 2016;

[81] D. Hertzog: *Next Generation Muon g-2 Experiments, arXiv:1512.00928v1*, December 2015;

[82] R. Carey et al.: *FERMILAB-PROPOSAL-0989*, 2009;

[83] Wesley Gohn: *Data Acquisition for the New Muon g-2 Experiment at Fermilab, arXiv:1506.00608 [physics.ins-det]*, June 2015;

[84] Alonzi, L.P. et al.: *The calorimeter system of the new muon g-2 experiment at Fermilab*, Nucl.Instrum.Meth. A824 718-720, October 2015;

[85] A.T. Fienberg et al: *Studies of an array of PbF_2 Cherenkov crystals with large-area SiPM readout*, arXiv:1412.5525v2, February 2015;

[86] W.R. Leo: *Techniques for Nuclear and Particle Physics Experiment*, Springer-Verlag, March 1987;

[87] S. Braibant, G. Giacomelli, M. Spurio: *Particles and Fundamental Interactions*, Springer, 2012;

[88] Walter H. Toki: *Review of Straw Chambers, SLAC-PUB-5232*, March 1990;

[89] F. Sauli: *Principles of operation of Multiwire Proportional and Drift Chambers*, Lectures given in the Academic Training Programme of CERN, 1975-1976;

[90] A. Anastasi et al: *Test of candidate light distributors for the muon g-2 laser calibration system*, arXiv:1504.00132v1, April 2015;

[91] Labsphere: *Integrating Sphere Theory and Applications*;

[92] INFN-16-04/LNF: *Linear Accelerator Test Facility at LNF Conceptual Design Report*, March 2016;

[93] G. Mazzitelli, F. Sannibale, P. Valente, M. Vescovi Laboratori Nazionali di Frascati dell'INFN, Frascati, Italy P. Privitera, V. Verzi: *Beam Instrumentation for the Single Electron DAΦNE Beam Test Facility*, 2003;

[94] Hamamatsu: *Photon Counting using Photomultipliers tubes*, April 2001;

[95] Corning: *Single Fiber Fusion Splicing*, Application Note, June 2009;

[96] Gerald Eigen: *SiPM Gain Stabilization Studies for Adaptive Power Supply, arXiv:1603.00016 [physics.ins-det]*, March 2016.